January 2018

Surfactants, Thermal And Surface Energy Effects On Emulsions' Transport Properties: A Study Using Lattice Boltzmann Method

Wessam Falih Hasan
Wayne State University, engwfh@yahoo.com

SURFACTANTS, THERMAL AND SURFACE ENERGY EFFECTS ON EMULSIONS' TRANSPORT PROPERTIES: A STUDY USING LATTICE BOLTZMANN METHOD

by

WESSAM FALIH HASAN

DISSERTATION

Submitted to the Graduate School

of Wayne State University,

Detroit, Michigan

in partial fulfillment of the requirements

for the degree of

DOCTOR OF PHILOSOPHY

2018

MAJOR: MECHANICAL ENGINEERING

Approved By:

_____

Advisor Date

_____

Co-Advisor Date

_____

_____

_____

DEDICATION

I LIKE TO DEDICATE THIS WORK WITH LOVE AND AFFECTION TO MY PARENTS, WIFE, SIBLINGS AND CHILDREN FOR THEIR GREAT PATIENCE AND SUPPORT DURING MY STUDY.

AND I DEDICATE THIS WORK TO THE STRONGEST PERSON I KNOW: ME

ACKNOWLEDGMENTS

I would like to express my deep thanks and gratitude to **Dr. Hassan Farhat** for the important role he played during my Ph.D study. I deeply acknowledge him for his trust in me and for all the time he spent in guiding and teaching me. I would like to thank Dr. Naeim Henein, Dr. Trilochan Singh, Dr. Marcis Jansons, Dr. Leela Arava and Dr. Christopher Eamon for serving as my doctoral committee.

Finally, I like to thank the **Higher committee for Education Development in Iraq** and **North Oil Company** for their financial support.

TABLE OF CONTENTS

DEDICATION ii

ACKNOWLEDGMENTS iii

LIST OF TABLES x

LIST OF FIGURES xi

LIST OF NOMENCLATURES xv

CHAPTER 1 INTRODUCTION 1

1.1 Emulsions 1

1.2 Economic Effect 2

1.3 Numerical Methods for Colloidal Studies 4

CHAPTER 2 LITERATURE SURVEY 6

2.1 The lattice Boltzmann method 6

2.1.1 The single component LBM 6

2.1.The multi-component LBM 9

2.2Colloidal Studies 13

2.2.1 Surfactant Laden Droplets in Shear Flow 13

2.2.2 Surfactant Laden Droplets in Poiseuille Flow 21

2.3 Contact Angle Analysis: 26

2.3.1 Static Contact Angle Analysis:.....26

2.3.2 Smooth surface: 27

2.4 Enhanced Oil Recovery (EOR).....29

2.4.1 Thermal Recovery 31

2.4.2 Gas Injection 35

2.4.3 Chemicals Injection 35

2.5 Machining Tool Cooling 36

CHAPTER 3 OUTLINE OF THE PRESENT WORK 40

3.1 Research objectives 40

3.1.1 Code development 41

3.1.2 Validation.....41

3.1.3Application.....41

3.2 Dissertation organization 42

Chapter 4:.....42

Chapter 5:.....42

Chapter 6:.....43

Chapter 7:.....43

Chapter 8:.....44

CHAPTER 4 HYBRID QUASI-STEADY THERMAL LATTICE BOLTZMANN MODEL FOR STUDYING THE RHEOLOGY OF SURFACTANTS CONTAMINATED EMULSIONS 45

4.1 Numerical Method 45

4.1.1 LBM and the Gunstensen Model 45

4.1.2 The Surfactant Model 50

4.1.3 The Quasi-Steady Thermal Model 53

4.1.4 The Hybrid Thermal-Surfactants Model 58

4.2 Simulation and Discussion 59

4.3 Effects of the Shear Strain Rate on the O/W Emulsion Effective Viscosity at Different Temperatures 62

4.4 Shearing of O/W Emulsions with Induced Heat by Constant Temperature Walls 64

4.5 Surfactants Distribution and Droplet Morphology Dependence on the Fluid's Temperature 68

4.6 Cutting Tool Cooling Simulation 71

4.6.1 Transient Thermal Case Study 71

4.6.2 Surfactant Distribution for Transient Thermal Case Study 74

CHAPTER 5 INVESTIGATING THE EFFECTS OF THERMAL AND SURFACE ENERGY ON THE FLOW CHARACTERISTICS OF OIL IN WATER MIXTURE BETWEEN PARALLEL PLATES AND IN CONFINED FLOW 77

5.1 Numerical Method 77

5.1.1 The Surface Tension Temperature Depended Model 77

5.1.2 The Contact Angle Temperature Depended Model 78

5.2 Flow Between Two Parallel Plates Simulation and Discussion Without Surfactants 79

5.2.1 Validating the Temperature Dependent Static Contact Angle 81

5.2.2 Simulating the Behavior of One and Two Slugs in Parabolic Flow at Different Temperatures 82

5.2.3 Droplets Flow between Two Parallel Plates at Different Temperatures 86

5.2.4 Flow Power Number Ratio 88

5.3 Confined Flow Simulation and Discussion Without Surfactants 90

5.3.1 Simulation and Discussion 90

5.3.2 Validating Temperature Dependent Static Contact Angle 92

5.3.3 Simulating the Behavior of A slug in Parabolic Flow at Different Temperatures 93

5.3.4 Droplets in Flow in Parabolic Flow at Different Temperatures 96

5.3.5 Flow Power Number Ratio 98

CHAPTER 6 INVESTING THE EFFECTS OF THERMAL, SURFACTANTS AND SURFACE ENERGY ON THE FLOW CHARACTERISTICS OF OTL IN WATER MIXTURE BETWEEN TWO PARALLEL PLATES 102

6.1 Simulation and Discussion 102

6.2 Simulating the Behavior of Droplet Flow in Parabolic Flow with and Without Surfactants 103

6.3 Simulating the Behavior of Slug Flow in Parabolic Flow with and Without Surfactants 106

6.4 Surfactants Distribution for the Droplet and the Slug Flow 109

6.5 Flow Power Number Ratio 111

CHAPTER 7 HYBRID THERMAL LATTICE BOLTZMANN MODEL FOR ANALYZING THE TRANSPORTATION OF SURFACTANTS CONTAMINATED EMULSIONS IN PARABOLIC FLOWS 115

7.1 Simulation Results and Discussion 115

7.2 Effects of Temperature Changes on the Multiphase Flow Behavior 117

7.2.1 Flow Average Velocity 119

7.2.2 Surfactants distribution 121

7.2.3 Leading Droplet Deformation Index 124

7.2.4 Rheological Behavior of the Mixture 125

7.2.5 Flow Power Number 126

7.2.6 Notes on the Transient Flow Temperature Distribution 128

7.3 Effects of the Pressure Gradient on the Multiphase Parabolic Flow Behavior 129

7.4 Effects of the Volume Fraction on the Multiphase Parabolic Flow Behavior 132

7.5 Effects of Surfactants Concentration the Multiphase Parabolic Flow Behavior 135

CHAPTER 8 CONCLUSIONS AND RECOMMENDATIONS 139

8.1 Conclusion 139

8.1.1 Hybrid Quasi-Steady Thermal LBM with Surfactants 139

8.1.2 Hybrid Quasi-Steady Thermal LBM with Contact Angles 140

8.1.3 Hybrid Quasi-Steady Thermal LBM with Contact Angle and Surfactants 140

8.2 Recommendations for Future Work 140

REFERENCES 142

ABSTRACT 158

AUTOBIOGRAPHICAL STATEMENT 161

LIST OF TABLES

Table 4.1: Fluids physical and LBM properties……..……56

Table 5.1: Interfacial tensions at different temperatures……..…..……78

Table 5.2: Values of calculated, measured and relative errors for contact angle for validation-1…….……..….82

Table 5.3: Values of calculated, measured and relative errors for contact angle for validation-2…….……...……82

Table 5.4: Values of calculated, measured and relative errors for contact angle for validation-1…..……..…93

Table 5.5: Values of calculated, measured and relative errors for contact angle for validation-2……..……..……93

Table 7.1**:** Fluid properties of the mixture constituent fluid in both physical and lattice units…….……118

LIST OF FIGURES

Figure 1.1: World oil production by the source from 1990-2030……...……..3

Figure 1.2: Worldwide EOR Production Rates oil production rates……5

Figure 2.1: (A) Velocity vectors for the D2Q9 and (B) for the D3Q19 lattice Boltzmann method used in this study……...……..7

Figure 2.2: Two mechanisms for suppressing coalescence are presented here. (A) Surfactant concentration gradient. (B) Steric repulsion…….21

Figure 2.3: Surface forces acting on the three-phase contact line of a liquid droplet deposited on a substrate…….……..……..26

Figure 2.4: Liquid drop under zero-gravity……..…27

Figure 2.5: Liquid droplet in contact with a smooth surface……....28

Figure 2.6: Typical Steam Injection Process to Lower Oil Viscosity…….…..33

Figure 2.7: Steam Assisted Gravity Drainage (SAGD) Process……..34

Figure 2.8: Gas Injection Method…….……....35

Figure 2.9: Surfactant molecule and surfactant orientation in water…….…..36

Figure 4.1: Velocity vectors for the D3Q19 lattice Boltzmann method used in this model……..……..……..……46

Figure 4.2: Explanation of the imposed boundary conditions and the method used for calculating the effective viscosity of the mixture in a shear flow domain……...…..…….63

Figure 4.3: Comparison of the simulation results for the effective viscosity for four cases of surfactants covered droplets with different temperatures. The insets from top left to low right are density; phase filed, surfactants distribution and horizontal velocity contours as slices in the xz plane……..…65

Figure 4.4: Top: Effective viscosity dependence on changing fluid temperature. Bottom: Dimensionless temperature and relative viscosity dependence on dimensionless time. The insets are showing the

temperature contours slices for two different dimensionless time steps……..…67

Figure 4.5: Front and back contours for the surfactants distribution at T=25^{o}C ……..68

Figure 4.6: Front and back insets for the surfactants distribution at T=50^{o}C....70

Figure 4.7: Temperature profile as a function of dimensionless time as prescribed in the text and evaluation of the relative viscosities for all cases at the determined dimensionless time. The insets are for the temperature contours. A- for upper plate velocities=$\mp$0.142, B- for top plate velocities=$\mp$0.284……..73

Figure 4.8: Surfactant distribution at same dimensionless time $T_{ds} = 0.1408$ for the four different dimensionless velocities…….……...….75

Figure 5.1: Static contact angles at different temperatures for the first and the second validation cases and static contact angle vs. temperature ……...84

Figure 5.2: One slug displacement at different temperatures and same dimensionless time…….…….……85

Figure 5.3: Two slugs' displacement at different temperatures and same dimensionless time…….…….……86

Figure 5.4: Droplets displacement at two different temperatures and same times with negative source term. Insets are for the streamlines of the various cases……..……87

Figure 5.5: Slugs and droplets power number ratios at different temperature ……..89

Figure 5.6: Static contact angles at different temperatures for the first and the second validation cases and static contact angle vs. temperature …….…….94

Figure 5.7: Slugs displacement at different temperatures and same dimensionless time……..……..……..96

Figure 5.8: Droplets displacement at three different temperatures and same times with negative, positive term. Insets are for the x-velocity of the various cases…….....97

Figure 5.9: Slug and droplets power number ratio at using the average slug and droplets velocity at different……..……..…..98

Figure 6.1: Droplet displacement at different dimensionless time steps (A) With surfactants (B) without surfactants…….……..……..105

Figure 6.2: Dimensionless average flow velocity of the red dropletwith and without surfactants at different dimensionless time steps…..…....106

Figure 6.3: Slug displacement at different dimensionless timesteps(A) With surfactants (B) without surfactants…….……...……107

Figure 6.4: Dimensionless average flow velocity of slug with and without surfactants at different dimensionless time steps……...……108

Figure 6.5: Surfactants distribution and verical tangetial velocity at different times (A) surfactant distributionfor the droplet (B) surfactant distribution for theslug……..……..……111

Figure 6.6: Slug and droplet power number ratios at different dimensionless time……..…….....113

Figure 7.1: Dimensionless average velocity versus dimensionless time for the flow of three droplets simulated at different temperature conditions……..……120

Figure 7.2: Droplets shape and dimensionless surfactants concentration for leading droplet at different temperatures (X) represents the leading droplet major axis half-length and (Ro) is the initial droplet radius……..122

Figure 7.3: (A) Deformation index of the leading droplets (B) Relative viscosities as a function of dimensionless time with different thermal conditions, (C) Power number ratio as a function of dimensionless time at various temperatures…….……125

Figure 7.4: Average flow velocities at different pressure gradients as function of the dimensionless time……..……..……130

Figure 7.5: Droplets shape and dimensionless surfactants concentration for leading droplet at different pressure gradients. (X) represents the leading droplet major axis half-length and (Ro) is the initial droplet radius……..……...130

Figure 7.6: (A) Deformation index at different pressure gradients (B) Relative viscosity at various pressure gradients (C) Power number ratio at various pressure gradients……..……..…..…..…132

Figure 7.7: Average Velocity at Different Volume Fractions……..……..……133

Figure 7.8: Droplets shape and dimensionless surfactants concentration for the leading droplet at different volume fractions. (X) represents the leading droplet major axis half-length and (Ro) is the initial droplet radius……..……...134

Figure 7.9: (A) Droplets Deformation Index at Different Volume Fractions (B) Viscosity at different Volume Fractions (C) Power Number at different volume Fractions……..……..……..134

Figure 7.10: Droplets dimensionless surfactants concentration for the leading droplet with the original source term and different surfactants concentrations. (X) Represents the leading droplet major axis half-length and (Ro) is the initial droplet radius. In the low concentration simulation figure, the distribution is not obvious because of scaling……..……..…136

Figure 7.11: Average Velocity at Different Surfactant Concentrations……....136

Figure 7.12: Droplets dimensionless surfactants concentration for the leading droplets at the reduced source term and different surfactants concentrations. (X) represents the leading droplet major axis half-length and (Ro) is the initial droplet radius……..……..…..137

Figure 7.13: (A) Droplets Deformation Index at different surfactants concentrations (B) Viscosity at various surfactants concentrations (C) Power number at different surfactants concentration……..……...…138

LIST OF NOMENCLATURES

$f_i\ (x,t)$ .....Density distribution function

$f_i^{\,L}(\boldsymbol{x},t)$ .....Light fluid density distribution function

$f_i^{\,H}(\boldsymbol{x},t)$ .....Heavy fluid density distribution function

$f_i^{\,eq}(x,t)$ .....Equilibrium Density distribution function

$\boldsymbol{\xi}$ .....Macroscopic physical velocity

λ .....Physical relaxation time

e_i .....Lattice link

$\widehat{f}_i^{\,q}$ .....Post-collision equilibrium distribution function

ϕ_i .....Volume fraction

$\phi_i(x)$ .....Source term

τ .....Lattice relaxation time

c_i .....Lattice velocity in the ith direction

c_s .....Lattice speed of sound

δ_t .....Lattice time step

ρ .....Macroscopic density

ρ_d .....Droplet density

ω_i .....Weighing constant

ν .....Kinematic viscosity

ν_{eff} .....Effective kinematic viscosity

g .....Gravitational acceleration

p .....Macroscopic pressure

$\boldsymbol{u}$ .....Macroscopic velocity

α .....Interfacial tension

$\alpha_q^{(T)}$ .....Temperature dependent surface tension

K .....Interface curvature

ρ^N .....Phase field

$\boldsymbol{F}(\boldsymbol{x})$ .....Macroscopic force

R .....Density of suspended fluid

B .....Density of suspending fluid

$R_i(x,t)$ .....Post segregation red fluid distribution function

$B_i(x,t)$ ……..Post segregation blue fluid distribution function

Γ ……..Surfactant concentration

Γ_∞ ……..Saturation surfactant concentration

D_s ……Diffusion constant

D_{ifs} ……...Thermal diffusivity

DI ……..……Deformation index

Pe_s ……..Surface Péclet number

R_0 ……Undeformed droplet radius

h ……...Channel height

ℓ ……Channel length

σ_0 ……....Clean droplet surface tension

σ ……....Contaminated droplet surface tension

$\sigma(T_f)$ ……Temperature dependent surface tension

E_0 ……Surfactant Elasticity

$E_o^{(T)}$ ……Temperature dependent surfactant elasticity

Eo ……... Eötvös number

P_r ……..Prandtl number

T

……...Temperature

χ ……..... Dimensionless ratio of energies

Ca ……Capillary Number

B_o ……..…….Bond Number

Re ……..….Reynolds number

$\dot{\gamma}$ ……..…..Shear strain rate

Ω_i ……..….Inverse of relaxation time

Q …….…..Volume flow rate

$\dot{m}$ ……...Mass flow rate

Δp …….Pressure difference

$\boldsymbol{u}_s$ ……...…Tangential velocity

μ_{eff} ……...Effective viscosity

μ_{rel} .....Relative viscosity

μ_m .....Mean viscosity

W .....Width

W_e .....Weber number

$\bar{U}$ .....Average velocity

θ_d .....Temperature dependent contact angle

θ^{ref} .....Reference contact angle

P ..... Undisturbed flow power

P_d .....Droplet power

R_P .....Power ratio

$\forall_d$ .....Combined droplets volume

V_{dmc} .....Combined droplets mass center

CHAPTER 1 INTRODUCTION

1.1 Emulsions

Emulsions are a mixture of two immiscible liquids (typically oil and water).One of the liquids is dispersed in the other, and they are valuable in a broad scope of utilization. For example, emulsions are used in body washes, nourishment products, droplet-based microfluidic systems, medication, and in processes in the oil industry and concoction business (Shu, Eijkel, et al. 2007). The main two types of emulsions: oil-in-water (O/W) emulsions, in which oil droplets are dispersed in water; (2) water-in-oil (W/O) emulsions, in which water droplets are dispersed in oil (D.G. Dalgleish 2006).

Traditionally emulsions are formed by using mixing and agitation at high-speed where induced stress in the flow is utilized to break an immiscible mixture into small droplets. A capillary number which is the ratio of the viscous to interfacial surface tension forces controls the size of the drops produced (Molly.K Mulligan 2012).

Size of droplets is controlled by adding surface acting agents (surfactants), which adheres to the interface of the droplet and reduces interfacial tension. Furthermore, surfactants play an important role in suppressing the coalescence of the droplets and affect the rheology of the mixture (Vlahovska and Loewenberg, 2005). The focus of this work is on studying emulsions in the crude oil industry, mainly on breaking trapped crude oil slugs in the tiny channels inside the wellbore and transportation of the daughter droplets inside pipes. Most of the current world

crude oil production comes from mature fields. Increasing oil recovery from the aging resources is a major concern for oil companies and authorities. Also, the replacement rate of the produced reserves by newly discovered oil has been decaying in the last decades. Subsequently, the increase in the recovered oil will be critical from mature fields under primary and secondary production to meet the growing energy demand in the coming years (V. Alvarado and E. Manrique 2010)

Crude oil development and production in oil reservoirs include up to three different phases: primary, secondary, and tertiary (or enhanced) recovery. In the primary one, the natural pressure of the reservoir or gravity drives the oil to the wellbore, by using artificial lift techniques (such as pumps) which bring the oil to the surface (Morrow 1991). But only less than 20 % of the original oil in the reservoirs is produced during the primary recovery. In the secondary recovery, the productivity of the field is increased by injecting gas or water to unsettle oil and move it to the production wellbore. This gives a recovery of 20 to 40 percent of the original oil (Green and Willhite 1998).

1.2 Economic Effect

Most of the currently used world oil production is from mature fields. Increasing the recovered oil which comes from the aging resources is a major concern for oil companies and authorities. Besides, the rate of replacement of the produced reserves by discoveries has been declining steadily in the last decades. Thus, the increase in the recovery from old fields using primary and secondary techniques will be critical to meet the demand for energy in the coming years.

World oil production is expected to rise from 82.3 mb/d in 2007 to 103.8 mb/d in 2030 (increases by 26%). Declines in crude oil output at existing fields (those already in production in 2007) are more than compensated for by output from fields under or awaiting development and, mainly in the last decade of the Outlook period, fields that are yet to be found. As shown in Figure 1.1(World Oil Production Forecast (IEA)2008).

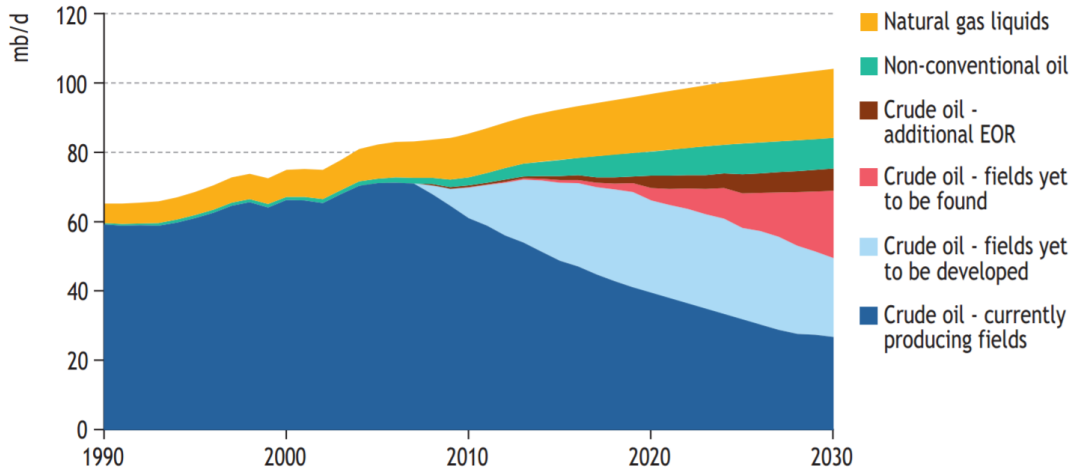

Figure 1.1 World oil production by the source from 1990-2030.

Worldwide, production of conventional crude oil alone increases only modestly, from 70.2 mb/d to 75.2 mb/d over the period. The share of natural gas liquids (NGLs) and enhanced oil recovery (EOR), predominately from the CO2 injection, in total oil production is expected to rise considerably, from 13% in 2007 to 25% in 2030. The contribution of non-conventional oil also is expected to increase substantially, from 2% in 2007 to 8.5% in 2030. Cumulative conventional oil production (crude and NGLs), which stood at 1.1 trillion barrels in 2007, is

projected to rise to over 1.8 trillion barrels by 2030. This will lead to a growth from slightly less than a third today to around one-half by 2030.

The global average recovery factor from oil reservoirs is about one-third. This recovery is considered small and leaves an enormous amount of oil underground. This motivates a global focus on increasing the number of the enhanced oil recovery projects. Since the straightforward and conventional light oil gets depleted, a move towards heavier hydrocarbon resources is demanded.

These resources include heavy and extra-heavy crudes, oil sands, bitumen and shale oil. Typically, the conventional oil recovery for these resources is generally low. An EOR method must be implemented in these reservoirs. Among few methods for EOR, thermal emerges as the more viable candidate especially in difficult resources worldwide. Figure 1.2 shows the number of projects used in EOR (Sunil and Al-Kaabi 2010).

1.3 Numerical Methods for Colloidal Studies

The fast and considerable development in computer technology in the last 20 years combined with an already matured branch of mathematics (Numerical Analysis Methods) are used efficiently as a tool for the studying of a wide range of problems in fluid dynamics.

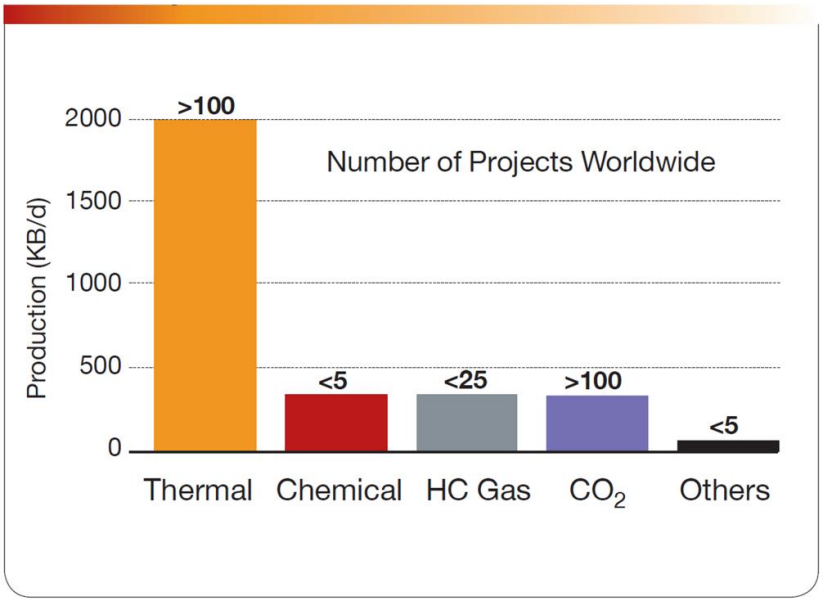

Figure 1.2 Worldwide EOR production rates oil production rates.

In this work, LBM based model, which couples the energy equation with the flow hydrodynamics and surfactants-interfacial physics is presented. This model is then used for studying the effects of temperature on the rheology of surfactants-contaminated emulsions in simple shear, through studying oil slug breakup and transportation in Couette flows and utilizing the developed model in simulating cutting tool cooling and lubrication. A quasi-steady thermal module characterized by updating the fluid transport properties as a function of the calculated fluid average temperature at each simulation time step is introduced. Speak more about your work. Please review my dissertation for this part.

CHAPTER 2 LITERATURE SURVEY

2.1 The lattice Boltzmann method

Computational fluid dynamics (CFD) constitute a powerful technique for investigating Complex multi-phase and multi-component flow problems. Droplet related studies such as the break-up, deformation, coalescence, and formation have attracted many researchers to get a better understanding of colloids and microfluidics applications. The Lattice Boltzmann method has been the point of interest of some researchers in the last 20 years due to its stability, parallelism and its simplicity.

2.1.1 The single component LBM

The Bhatnagar-Gross-Krook (BGK), lattice Boltzmann method, is an alternative computational technique used for solving a broad range of fluid problems. The isothermal, single-relaxation model is derived from the following Boltzmann kinetic equation (Yu et al. 2002):

$$\frac{df}{dt} + \boldsymbol{\xi} \cdot \nabla f = -\frac{1}{\lambda}(f - f^{eq}) \tag{2.1}$$

Where f is the density distribution function, $\boldsymbol{\xi}$ is the macroscopic velocity, f^{eq} is the equilibrium distribution function, and λ is the physical relaxation time.

Equation (2.1) is first discretized by using a set of velocities $\boldsymbol{\xi}_i$ confined to a finite number of directions, and this leads to the following equation:

$$\frac{df_i}{dt} + \boldsymbol{\xi}_i \cdot \nabla f_i = -\frac{1}{\lambda}(f_i - f_i^{eq}) \tag{2.2}$$

The LBM is based on a set of equivalent Cartesian velocities. The D2Q9 BGK described here has nine velocity direction vectors (lattice links) shown in Fig 2.1 (A) with the following endpoints coordinates:

$$
\begin{aligned}
&e_0(0,0,0); e_1(-1,-1,0); e_2(-1,0,-1); e_3(-1,0,0);\\
&e_4(-1,0,1); e_5(-1,1,0); e_6(0,-1,-1); e_7(0,-1,0);\\
&e_8(0,-1,1); e_9(0,0,-1); e_{10}(1,1,0); e_{11}(1,0,1);\\
&e_{12}(1,0,0); e_{13}(1,0,-1); e_{14}(1,-1,0); e_{15}(0,1,1);\\
&e_{16}(0,1,0); e_{17}(0,1,-1); e_{18}(0,0,1);
\end{aligned}
\tag{2.3}
$$

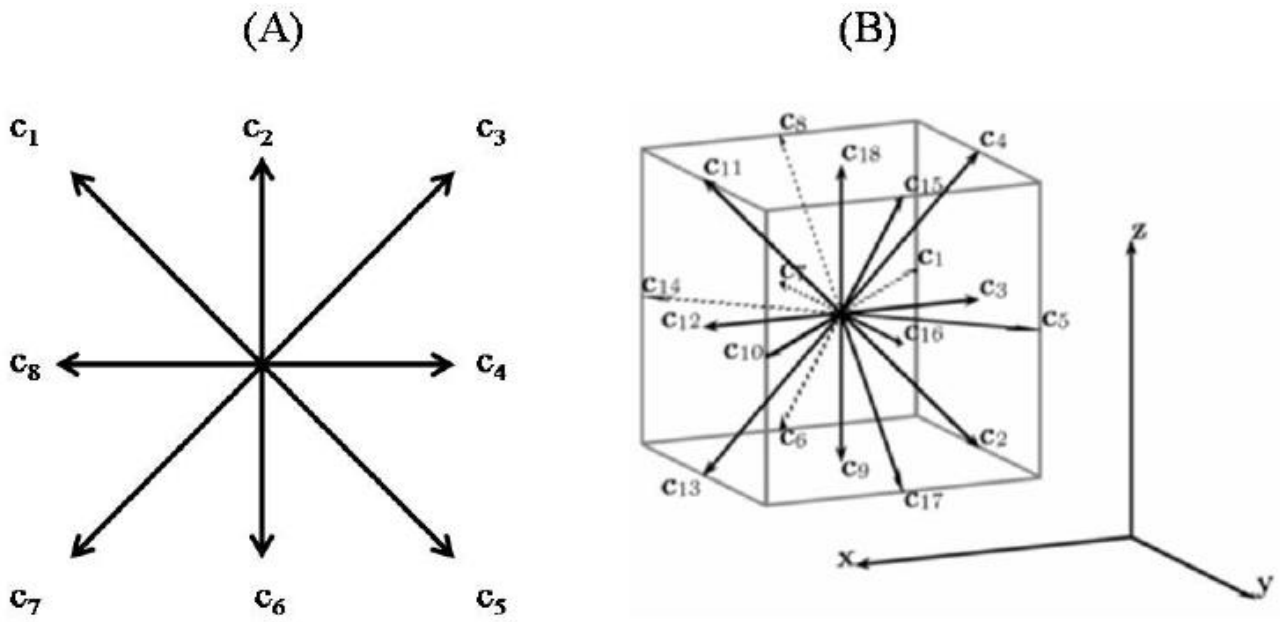

Figure 2.1 (A) Velocity vectors for the D2Q9 and (B) For the D3Q19 lattice Boltzmann method used in this study.

Figure 2.1 (B) show the lattice links for the D3Q19 model. Equation (2.2) is further discretized in the lattice space and time, and this leads to the following:

$$
f_i(x + c_i\delta_t, t + \delta_t) - f_i(x,t) = -\frac{1}{\tau}[f_i(x,t) - f_i^{eq}(x)] \tag{2.4}
$$

The lattice space δ_x and the lattice time step δ_t are taken as unity, and their ratio $c = \delta_x / \delta_t$ is the lattice velocity. The lattice speed of sound is used for determining the fluid pressure by $p = \rho c_s^2$, and the lattice relaxation time is $\tau = \lambda / \delta_t$. The kinematic viscosity is derived from the relaxation time by the following formula:

$$\nu = (\tau - 0.5) c_s^2 \delta_t \tag{2.5}$$

The equilibrium distribution function of Eq. (2.4) is calculated as follows:

$$f_i^{eq} = \rho \omega_i [1 + \frac{3}{c^2} c_i.u + \frac{9}{2c^4} (c_i.u)^2 - \frac{3}{2c^2} u.u] \tag{2.6}$$

Where $\tau = \lambda / \delta_t$ is the lattice velocity in the i^{th} direction, ω_i are the weighting constants for the various lattice links:

$$\omega_i = [4/9; 1/36; 1/9; 1/36; 1/9; 1/36; 1/9; 1/36; 1/9] \tag{2.7}$$

u and ρ are the macroscopic velocity and density, respectively. The macroscopic density and momentum are calculated from the distribution function as follows:

$$\rho = \sum_{i=0}^{Q-1} f_i = \sum_{i=0}^{Q-1} f_i^{eq} \tag{2.8}$$

$$\rho \boldsymbol{u} = \sum_{i=1}^{Q-1} \boldsymbol{c}_i f_i = \sum_{i=1}^{Q-1} \boldsymbol{c}_i f_i^{eq} \tag{2.9}$$

Where *Q* depends on the dimension and the type of the LBM model. Through a Chapman-Enskog expansion in the low frequency, long wavelength limits, and at low Mach number, the LBM can recover the Navier-Stokes equations to a second order accuracy if the right choice of the equilibrium distribution function is used

(Chen et al., 1992; Guo et al., 2000; Latt, 2007).

2.1.2 The multi-component LBM

The most famous multi-component LBM schemes is the Gunstensen model (Gunstensen et al., 1991) This scheme is used in this work.

The Gunstensen model identifies a red and a blue momentum distribution functions as $R_i(x,t)$ and $B_i(x,t)$ where x and t are the nodal position and time, respectively. The total momentum distribution function is the sum of the two functions (Gunstensen et al. 1991):

$$f_i(\boldsymbol{x},t) = R_i(\boldsymbol{x},t) + B_i(\boldsymbol{x},t) \tag{2.10}$$

The main difference between the two-component and the single component LBM is the modification of the collision rules to induce surface tension and segregate the two immiscible fluids. This is achieved by applying two-step collision rules (Gunstensen et al., 1991; Halliday et al., 2005; Halliday et al., 2006; Halliday et al., 2007, Hollis et al., 2007; Reis and Philip, 2007). The main streaming and collision function is expressed as follows:

$$f_i(x + c_i\delta_t, t + \delta_t) = f_i(x,t) - \frac{1}{\tau}\{f_i(x,t) - f_i^{eq}(\rho, \rho u)\} + \phi_i(x) \tag{2.11}$$

Where c_i is the lattice velocity vector in the i^{th} direction as shown in Fig. 2.1, τ is the lattice relaxation time, $\phi_i(x)$ is a source term used to induce an interfacial pressure step in the fluid mixture as per Lishchuk's interface method (Lishchuk et al., 2003; Lishchuk et al., 2008). The source term can also enclose a force in the

flow direction, which causes fluid movement. To define the interface between the two fluids, a phase field is described as follows (Halliday et al. 2007):

$$\rho^N(\boldsymbol{x},t) = \frac{R(\boldsymbol{x},t) - B(\boldsymbol{x},t)}{R(\boldsymbol{x},t) + B(\boldsymbol{x},t)} \tag{2.12}$$

Where *N* refers to the direction normal to the interface and the nodal red and blue densities are expressed by the following:

$$R(x,t) = \sum_{0}^{Q-1} R_i(x,t) \tag{2.13}$$

$$B(x,t) = \sum_{0}^{Q-1} B_i(x,t) \tag{2.14}$$

The two fluids can have different viscosities. This requires the use of various relaxation times in Eq. (2.5). The interface is made of a fluid mix; therefore, its viscosity is determined by the following equation (Dupin et al. 2003):

$$\nu_{eff} = (\tau_{eff} - 0.5)c_s^2\delta_t = \left(\frac{R}{R+B}\right)\nu_R + \left(\frac{B}{R+B}\right)\nu_B \tag{2.15}$$

Lishchuk's interface method is implemented to create a pressure step across the interface. The resulting surface tension force *F*(*x*) is used (Lishchuk et al. 2008):

$$F(x) = -\frac{1}{2}\alpha K \nabla \rho^N \tag{2.16}$$

Where $\nabla\rho^N = 0$ for a constant phase field. This means that this force is only applicable to the interface. α The surface tension parameter and k the curvature

of the interface. k Is obtained from the surface gradients by solving the following equation using the finite difference method (Lishchuk et al.,2003):

$$K = n_x n_y \left(\frac{\partial n_x}{\partial_y} + \frac{\partial n_y}{\partial_x} \right) - n_x^2 \frac{\partial n_y}{\partial y} - n_y^2 \frac{\partial n_x}{\partial x} \tag{2.17}$$

Where n_x, n_y are the x and y components of the interface normal vector $n \equiv -\nabla\rho^N / |\nabla\rho^N|$. $F(x)$ From Eq. (2.16) is used to correct the velocity by Guo's methodology (Guo et al., 2002; Dupin et al., 2003) as follows:

$$u^* = \frac{1}{\rho}\left[\sum_{i=1}^{Q-1} f_i c_i + \frac{1}{2} F(x) \right] \tag{2.18}$$

The relation between the macroscopic and a spatially varying lattice source term is by the following:

$$\phi_i = \omega_i \left(1 - \frac{1}{2\tau} \right) \left[3(c_i - u^*) + 9(c_i . u^*) c_i \right] . F(x) \tag{2.19}$$

Where u^* is the corrected velocity from Eq. (2.18). For constant body force this relationship is expressed by the following equation (Halliday et al. 2007):

$$\phi_i = \omega_i \frac{1}{k_2} F . c_i \tag{2.20}$$

Where $k_2 = 1/3$ and F is a constant macroscopic force such as a body force. The first collision is then applied using the corrected velocities in the calculation of equilibrium distribution function $f^{eq}(\rho, \rho u)$.The second step is the segregation of the two fluids which is achieved by imposing zero diffusivity of one color into the other (Gunstensen et al., 1991). A local color gradient is identified as follows:

$$G(x,t) = \sum_{ij} c_i \left(R_j(x + c_i, t) - B_j(x + c_i, t) \right) \tag{2.21}$$

The following formula calculates a local color flux:

$$J = \sum_{i} c_i \left(R_i(x,t) - B_i(x,t) \right) \tag{2.22}$$

The segregation step is achieved by forcing the local color flux to align with the direction of the local color gradient. Thus, the colored distribution functions at the interface are redistributed such that $J.G$ is maximized with the following constraints:

$$\begin{aligned} &\sum_{i} R_i(x,t) = R(x,t) \\ &B_i(x,t) = f_i(x,t) - R_i(x,t) \end{aligned} \tag{2.23}$$

Where B_i, f_i, R_i are the post-collision post-segregation blue, total, and red distribution functions respectively. The segregation can also be accomplished by a formulaic means as described in the model of Halliday et al. (2007) in accordance with the method of D'Ortona et al. (1995):

$$\begin{aligned} R_i(x, t + \delta_t) &= \frac{R}{R+B} f_i(x, t + \delta_t) + \beta \frac{RB}{R+B} \omega_i \cos(\theta_f - \theta_i) \mid c_i \mid \\ B_i(x, t + \delta_t) &= \frac{B}{R+B} f_i(x, t + \delta_t) - \beta \frac{RB}{R+B} \omega_i \cos(\theta_f - \theta_i) \mid c_i \mid \end{aligned} \tag{2.24}$$

Where θ_f and θ_i are the polar angle of the color field, and the angle of the velocity link respectively β is the segregation parameter. After the segregation process the two components propagate separately as follows:

$$R_i(x + c_i\delta_t, t + \delta_t) = R_i(x, t + \delta_t) \quad (2.25)$$

$$B_i(x + c_i\delta_t, t + \delta_t) = B_i(x, t + \delta_t) \quad (2.26)$$

2.2 Colloidal Studies

2.2.1 Surfactant Laden Droplets in Shear Flow

Experimental, analytical and numerical simulation studies were performed on Surfactant laden droplets in shear flow. Janssen et al. (1994) reported a phenomenological approach to link interfacial viscoelasticity to droplet breakup.

Partal et al. (1997) explored the influence of temperature and stabilizer concentration on emulsions' viscosity. The test emulsions were stabilized by a sucrose ester (SE) of high hydrophilic-lipophilic balance (HLB). Emulsions showed shear thinning at intermediate shear rates, metastable behavior at low shear rates and a limiting viscosity at high shear rates. As emulsion temperature increased, the emulsion viscosity decreased. On the other hand, phase separation and coalescence for high oil concentration took place at low temperature.

Gustavo et al. (1998) executed experiments on the flow characteristics of concentrated emulsions for Venezuelan bitumen in water with the presence of surfactants. These emulsions were studied between rotating cylinders, in a colloid mill, and in pipes. The authors examined the local inversion of an emulsion due to local increases in the bitumen fraction induced by flow. They also observed the conditions that lead to slip flow, in which the drag was reduced by the formation

lubricating layer of water at the wall. The results revealed the mechanisms that took place in the pumping and pipelining of oil-in-water emulsions.

Hu and Lips (2003) investigated the individual effects of the dilution, the tip stretching and the Marangoni stress on surfactant covered mother droplet by measuring the interfacial tension of the generated daughter droplets. Almatroushi and Borhan (2004) tested surfactant effects on the buoyancy of bubbles and viscous droplets in a confined region.

Kundu and Mishra (2013) investigated the removal of oil from oil-in-water emulsion using a packed bed of an ion-exchange resin, which was acting as a coalescing agent for the oil existing in the oil-in-water emulsion system. They evaluated the operating parameters through performing initial experimental studies to assess the operating parameters. These parameters were used for the determination of the oil removal efficiency. The effect of pH, oil concentration, bed height, and flow velocity on the removal efficiency of the resin bed was studied simultaneously. The results indicated that the responses were well predicted, and they were satisfactorily within the limits of the input parameters being used.

Kundu et al. (2015) studied the rheological behavior of oil-in-water emulsions with several oil concentrations (10– 80%), at different temperatures (25–50 ^{o}C) and with shear strain rates ranging from 1 to 100 s-1. Surfactants with varying concentration from 0.5 to 2 w/v % were used in this study. These emulsions exhibited a typical shear thinning behavior. The power law, as a relation between the shear stress and the shear strain rate, described well this rheological behavior.

The authors used several viscosity models, and the linear regression to curve fit the experimental rheological data. The experiment showed that by increasing the oil concentration, emulsions' viscosity and pseudoplasticity increased. Furthermore, emulsions' viscosity and pseudoplasticity decreased with the increase in temperature. The measurements of surface tension and droplet size distribution showed that they decrease with the increase in oil concentration.

Francesco (2002) used a perturbative approach to obtain an analytic solution for the shape of the droplet for the non-Newtonian fluids. The perturbation method is different from the classical approach which used for the Newtonian fluids, as it triggers use of rotational invariance to obtain from the beginning a full illustration of the velocity and pressure fields tensors.

Milliken et al. (1993) studied the effect of dilute, insoluble surfactants on the deformation and breakup of a viscous drop. The deformation and stretching of a drop were examined. The authors reported that the effects of surfactants were the most influential for small viscosity ratios, where Marangoni stresses substantially impeded the interfacial velocity and caused the drop to behave as more viscous. The authors reported that surfactants facilitated the formation of pointed ends during drop stretching, and this may expound the presence of tip streaming in experiments using viscoelastic droplets. Li and Pozridikis (1997) used a numerical approach similar to the previous one; they utilized viscosity ratio of unity with respect to the matrix with a linear surfactant equation of state to study the transient deformation of a spherical droplet. Eggleton et al. (2001) investigated tip streaming

and drop breakup in a linear extensional flow as a function of the initial surfactants coverage. They used boundary integral formulation for the Stokes equations, Runge-Kutta method for the interface time evolution and a finite difference for the mass balance equation.

Inamuro et al. (2003) used a lattice Boltzmann method (LBM) for multi-component immiscible fluids for different values of viscosity and capillary numbers under shear flow. In their simulations they used three different values for Reynolds number. The authors utilized the technique to study the deformation and break-up of a droplet in shear flows. The simulation results demonstrated that increasing the Reynolds number makes the deformation and break-up easier. Among other factors such as shear stress and surfactants, the temperature has the most influential role in the composition, rheological and transport characteristics of emulsions characterized by high viscosity ratio.

Drumright-Clarke (2002) and Drumright-Clarke and Renardy (2004) applied direct numerical simulations with a volume-of-fluid continuous surface stress algorithm to study the effects of insoluble surfactants at low concentration on a drop in strong shear. They used same viscosity and density for the droplet and the surrounding. The movement of the surfactants produces a Marangoni force which acts toward the drop center. For low inertia, viscous force opposes the Marangoni force. This force leads to that the stationary surfactants-covered droplet is more elongated than the one without surfactant. Breakup chances increase with the addition of surfactants at reduced critical capillary number. The produced daughter

droplets for this case are smaller compared to the case of uncontaminated droplets. Kruijt-Stegeman et al. (2004) used a finite element method to study the transient deformation of droplets in supercritical elongational flow and the breakup of elongated drops in quiescent medium with low surfactant coverage. They found that the droplet deformation increases with the increasing of surfactant coverage.

Dan and Jing (2006) developed a viscosity model for studying non-Newtonian emulsions. Empirical and theoretical relationships were proposed to describe the apparent viscosity versus water cut behavior of the water-in-crude oil emulsions. Their model was able to predict the relative viscosity of water-in-crude oil emulsions over the range of the maximum and minimum water cut.

Van der Graaf (2006) and van der Sman and van der Graaf (2006) used a free energy-based LBM to develop a diffuse model for studying the adsorption of surfactant onto flat and droplets interfaces. The model was tested in 2D linear shear and uniform flow fields to show its applicability when coupled to the hydrodynamics. The following studies (Lyu et al., 2002; Jeon and Makosco, 2003; Milliken et al., 1992; Hu and lips, 2003; Cheng et al., 2005; Sundaraj and Makosco, 1995; Kleshchsnok and Lang, 2007) provide a good understanding of the physical interaction and deformation of droplets during their formation and breakup.

Zhi and Jin (2007) presented a three-dimensional (3D) numerical study using a uniform staggered Cartesian grid. They explored the deformation and breakup of a droplet suspended in an immiscible viscous fluid under shear flow. They treated the surface tension as a modified stress. Their results were in good

agreement with the experimental measurements. Lai et al. (2008) developed an immersed boundary method for modeling fluid interfaces with insoluble surfactant in 2D geometries. Asymmetric discretization for the surfactant concentration was employed to ensure surfactant mass conservation numerically.

Farhat et al. (2011) proposed a hybrid model for the study of the droplet flow behavior in an immiscible medium with insoluble nonionic surfactants adhered to the O/W interface. The surfactants concentration distribution on the interface was modeled by using the time-dependent surfactant convection-diffusion equation. A finite difference scheme was employed in the solution. The fluid velocity field, the pressure, and the interface curvature were calculated by using the lattice Boltzmann method (LBM) for binary fluid mixtures. The coupling between the finite difference scheme and LBM was achieved through the LBM variables and the surfactants equation of state. The Gunstensen LBM was used in their study because it provided local and independent application of a special interfacial tension on the individual nodes of the droplet interface. The hybrid model was developed and successfully applied to droplet deformations under a variety of flow conditions.

Taghilou and Rahimian (2014) utilized a thermal lattice Boltzmann model to simulate the behavior of a droplet deposited on a solid surface. The simulation took into consideration the contact angle between gas, solid and liquid phases. For this thermal lattice Boltzmann simulation, Lee's model [29] was used to track the droplet interface. The Boussinesq approximation was implemented to couple

energy and momentum equations. Numerical results for the simulation boundary conditions of constant wall temperature and constant heat flux on the wall were in agreement with previous numerical results. The subject of the various studies stated in the review includes some selected facts which are relevant to this work:

- Surface tension decreases with the presence of the surfactant which leads to increase in droplets deformability through the increase in capillary number. The capillary number represents the ratio between the relative effect of viscous forces versus surface tension acting across an interface between a liquid and gas, or between two immiscible liquids. The capillary number is given by: $Ca = \frac{\mu R \dot{\gamma}}{\alpha}$, where μ is the viscosity of suspending fluid, R is the droplet radius, $\dot{\gamma}$ is the shear rate, and α is the surface tension.
- There are three mechanisms resulting from the existence of surfactant and these are namely: Tip stretching which is generated due to movement of the surfactant towards the tip of the droplet, Marangoni stresses which caused by the gradient in the surfactant concentration along the interface and surface dilution which is produced as a result of area increase of the droplet surface during deformation.
- Surfactants suppress coalescence, which leads to stable colloids. To explain suppressing the coalescence, there are two theories shown in Fig 2. 3; the first (Fig 2.3(A)) postulates that the Marangoni stresses increase on the opposing interfaces due to the squeeze of the matrix between the droplets. This leads to

a reduction in the local interface velocity, consequently, slows down the film drainage and then ban coalescence. The other one (Fig 2.3 (B)) supposes that the suppression of coalescence is due to steric repulsion force formed due to the surfactant layers' compression, which is attached to the surfaces of two approaching droplets, and that steric force is a surfactant molecular weight dependent force (Lyu et al.; 2002).

- Development of surfactant-covered droplet in Poiseuille flow is important for many industries. Numerical and experimental studies have been produced on the topic of surfactant-covered droplets. (Bentley and Leal 1986; Stone and Leal 1990; Janssen et al. 1994; Pawer and Stebe 1996; Eggleton and Stebe 1998; Eggleton et al. 2001; Greco 2002; Saiki et al. 2007; Janson and Anderson 2008; Ward et al. 2010; Kondaraju et al. 2012; Sourki et al. 2012) The final morphology of the system helps to determine the material, mechanical, chemical, thermal and sensory properties of the finished product (Bruijn 1998).

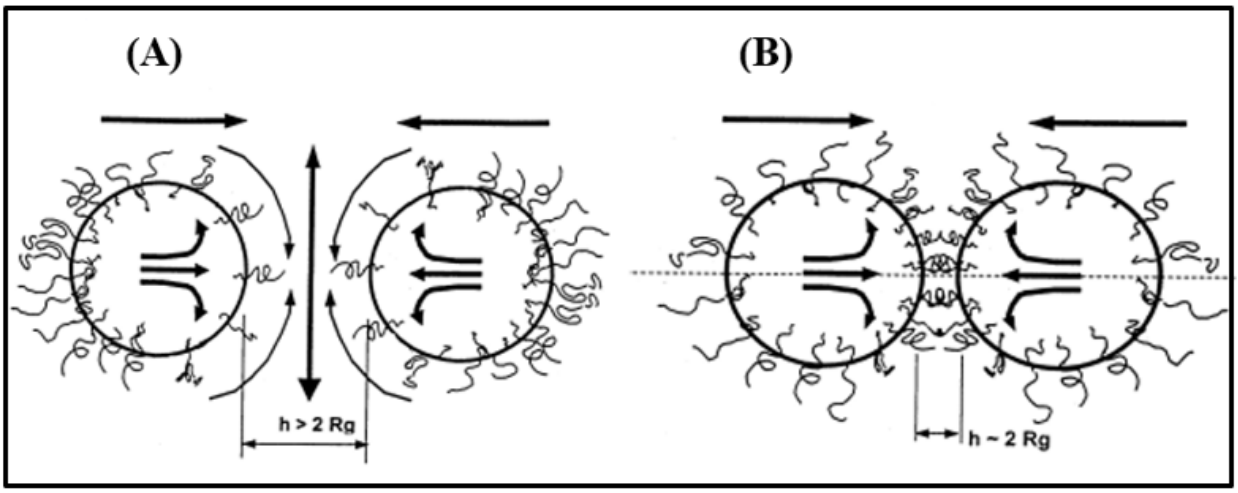

Figure 2.2 Two mechanisms for suppressing coalescence are presented here. (A)Surfactant concentration gradient. (B) Steric repulsion (Lyu et al., 2002).

2.2.2 Surfactant Laden Droplets in Poiseuille Flow

Baroud et al. (2010) studied microfluidic droplets merging, forming and transportation. They focused on the pressure fields associated with the presence of the interfacial tension. Furthermore, the authors studied the formation of drops, the nature of the dominant interactions in relation with the geometrical domain, the transport of drops and the fusion of two drops. They found that the interaction between capillary-viscous effects can be dominant in many cases and this interaction grows in unforeseen manner on the scale of the droplet or locally on the interface region. The flow rate versus pressure led to miscellaneous flow patterns and the presence of surfactants added further challenges through their effects on the flow-fields velocities.

Mulligan and Rothstein (2011) comprehensively studied wall confinement effects on droplet flow in a microchannel, and their findings showed that the degree of confinement was accountable for droplet tip streaming formation.

Baret (2012) discussed the importance of surfactants on droplets' flow in microfluidics. He reviewed interfacial rheology and emulsion properties of surfactants-laden droplets. Understanding the properties of emulsions, their interfaces is very important for the overall capabilities of microfluidics. This stems from the fact that microfluidic systems are very powerful tools for the study of surfactants dynamics at the time- and length-scale relevant to certain applications and they constitute a favorable tool for the study of the interfaces in complex systems.

Kowalewski (1984) performed experiments on the concentrated suspension of droplets, and they measured the velocity profiles and concentration of droplet suspensions flowing through a tube. Lovick and Angeli (2004) experimentally studied the vertical droplets distribution and size in dispersed liquid-liquid flow in a pipe. At different regions in the pipe they measured droplet velocities, and they saw that no significant droplet size changed when mixture velocity changed. Oshima et al. (2007) used confocal μPIV to study the flow field inside a moving droplet; after assessing the flow field at different planes, they were able to reshape the 3D flow topology to get a clear and high contrast images. The outcome of this study revealed the role of the flow around the droplet and the interface (liquid-liquid) on the flow topology. Then, they extended the research to

simultaneously describe the surrounding and internal flow by using multicolor illumination (Oshima et al. 2009).

Guido and Preziosi (2010) reviewed pressure driven droplet behavior flow in rectangular and circular cross-sectional channels; they discussed capillary number, droplet breakup and deformation, viscosity ratio for central oriented and central offset droplet. They also reviewed the role of surfactant on the droplets formation.

Jakiela et al. (2012) employed μPIV to report an interrupted transition in convective droplet velocity moving in a rectangular micron-sized channel with less than unity viscosity ratio. Their study showed changing in flow topology from a region characterized by two high recirculation, to another exhibiting four extra counter-rotating rolls at the caps.

Wu et al. (2015) Studied morphological developments droplets using a high-speed camera. The target of their study was to investigate the influences of both the dispersed droplet size and two-phase average flow velocity on the formation of tip stream at the rear part of the droplets. There exists a critical droplet (bubble) length depends on capillary number They found that the deformation of the droplet increased with the increase in Capillary number. They got a critical droplet length based on the Capillary number, beyond which the droplets start to breakup and produce small daughter droplets.

Many numerical studies performed on pressure-driven flow. Nott and Brady (1994) employed Stokesian Dynamics to simulate the pressure-driven flow of a

non-Brownian suspension at zero Reynolds number. They found that the particles gradually migrate toward the center of the channel, resulting in an inhomogeneous concentration profile, and a notching in the velocity profile.

Zhou and Pozrikidis (1994) adopted a boundary integral method to simulate the pressure-driven flow of a periodic suspension of droplets, and their findings showed that when the viscosity of the suspending fluid and droplets is the same, the droplets migrated toward the centerline of the channel. For the case of a single droplet, they used a viscosity ratio of 10, and they found that it migrates to an equilibrium position at about halfway between the wall and the centerline.

Loewenberg and Hinch (1996) simulated suspensions consisting of multi three-dimensional droplets in a linear shear flow. Their study revealed a shear thinning behavior for the suspension, and they found a slight increase in emulsion viscosity with volume fraction.

Mortazavi and Tryggvasson (2000) investigated the lateral migration of two-dimensional drops in a channel consisting of two parallel planes for limited Reynolds number. The full Navier–Stokes equations was solved using a second-order projection method, and a finite-difference/front-tracking approach to test the dynamic drop behavior.

Li and Pozrikidis (2000) performed a dynamic simulation on two-dimensional pressure driven flow between two parallel walls of a confined channel; they focused on the effects of viscosity ratio and the capillary number on the droplets distribution across the channel width and the effective suspension

viscosity. Staben et al. (2003) utilized a boundary-integral method to investigate the rotational and translational velocities of spherical and ellipsoidal particles, as functions of particle location and size in the channel.

Doddi and Bagchi (2009) executed three-dimensional simulations for the flow in a microchannel with a vast number of deformable cells by using the immersed boundary method. They investigate the three-dimensional velocity fluctuation and trajectories of each cell in the suspension. Bayareh and Mortazavi (2011) simulated the collision of two equal-size drops in an immiscible phase undergoing a shear flow. Mortazavi et al. (2011) studied the lateral migration of a droplet and reported that at a relatively high Reynolds number and small deformation, the droplet migrates to an equilibrium position, which is a little off the channel centerline. They witnessed a shear thinning behavior when simulated the suspension of 36 drops at finite Reynolds numbers.

Nourbakhsh et al. (2011) used a finite difference scheme to study the motion of three-dimensional deformable droplets in a Poiseuille flow at non-zero Reynolds numbers. They examined the effects of Reynolds Number, volume fraction and Capillary number on the flow. They found that the droplets tend to move towards the position at the middle between the centerline and the channel wall while exhibiting small deformation and proceeding like rigid particles. Highly deformable droplets appear to migrate to the channel centerline.

Opportunity

Introducing a LBM based model, which couples the energy equation with the flow hydrodynamics and surfactants-interfacial physics is for studying the effects of temperature on the rheology of surfactants-contaminated emulsions.

2.3 Contact Angle Analysis:

2.3.1 Static Contact Angle Analysis:

The contact angle is the angle which measures the ability of a liquid to spread when settled on a solid surface. The solid-air and liquid-air interfaces come together to form static contact angle (θ).

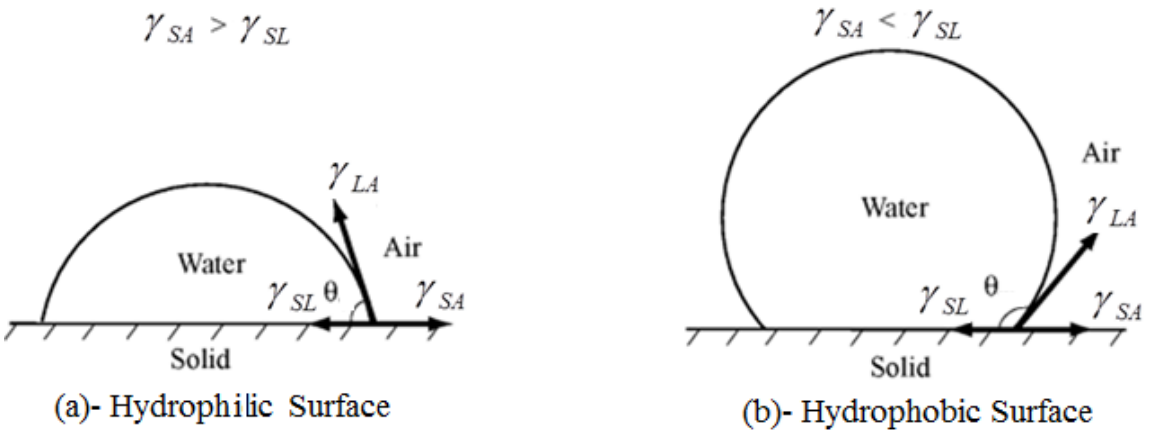

Figure 2.3 Surface forces acting on the three-phase contact line of a liquid droplet deposited on a substrate.

The contact angle is the angle at which the outline tangent of a liquid drop meets a solid surface. According to the value of the contact angle, surfaces are classified as hydrophilic with an angle ($\theta < 90^o$) or hydrophobic with an angle ($\theta > 90^o$). Superhydrophobic surfaces are surfaces with contact angles ($\theta > 150^o$) (De Gennes et al., 2004).

There are several models for interpreting interface force equilibrium; Laplace's theorem model is the most general one, which connects the relation between the pressure difference inside and outside of a spherical interface and the surface tension as follow: (Okiishi et al. 2006):

$$\Delta P = 2\gamma / R \tag{2.27}$$

where γ is a surface tension coefficient, R *is* the radius of the interface.

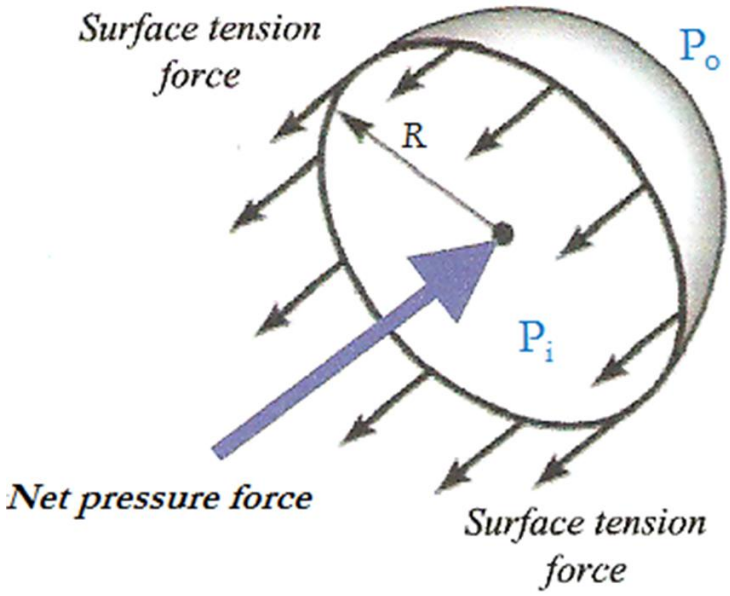

Figure 2.4 Liquid drop under zero-gravity (Michael Nosonovsky and Bhushan, 2005).

2.3.2 Smooth surface:

When a liquid contact a solid surface, the system energy of the two separated surfaces reduced by the molecular attraction. Adhesion force between the two surfaces per unit area is given by Dupré equation (Bisanda, 2000):

$$W_{SL} = \gamma_{SA} + \gamma_{LA} - \gamma_{SL} \tag{2.28}$$

Where γ_{LA} is the interfacial tension, γ_{SA} is the solid air surface tension and γ_{SL} is the solid-liquid surface tension. From the condition of minimizing the total energy E_{tot} of the system, the contact angle is determined. This is given by:

$$E_{tot} = \gamma_{LA}\left(A_{LA} + A_{SL}\right) - W_{SL}.dA_{SL} \tag{2.29}$$

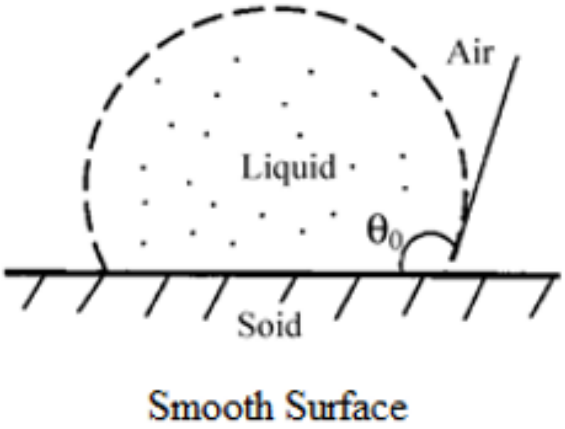

Figure 2.5 Liquid droplet in contact with a smooth surface (Michael Nosonovsky and Bhushan, 2007).

By assuming that the droplet is small, so the gravitational potential energy can be neglected. At the equilibrium $dE_{tot} = 0$:

$$\theta = \gamma_{LA}(dA_{LA} + dA_{SL}) - W_{SL}.dA_{SL} \tag{2.17}$$

For a constant volume droplet, and employing geometrical considerations:

$$\frac{dA_{LA}}{dA_{SL}} = \cos\theta_o \tag{2.18}$$

This leads to Young's equation for contact angle on a flat surface (Michael Nosonovsky and Bhushan, 2007):

$$\cos\theta_o = \frac{\gamma_{SA} - \gamma_{SL}}{\gamma_{LA}} \quad (2.19)$$

Young's formula represents a simplified formula of the real situation, and it is only valid for smooth, homogeneous surfaces.

Opportunity

Presenting a thermal lattice Boltzmann model which is coupled with a temperature dependent interfacial tension and contact angle modules to study the combined multi-physics effects on oil/water system.

2.4 Enhanced Oil Recovery (EOR)

Most of the current production of the world oil comes from mature fields. Increasing oil recovery from the aging resources is a major concern for oil companies and authorities. Besides, the rate of replacement of the produced reserves by discoveries has been declining steadily in the last decades. (Lake LW 1989; Bedrikovetsky 1993). Crude oil development and production can include up to three distinct phases: primary, secondary, and tertiary (or enhanced EOR) recovery.

Enhanced oil recovery (EOR) is a very challenging area for different scientific disciplines. Limited number of patents were filed about this topic in the last ten years (which are less than 25), which reflects the difficulty related to the research in this field (Wever et al. 2011). EOR is a technique, which includes utilizing additives to the crude oil to control the following (Sandersen 2012):

- Wettability

- Fluid properties
- Interfacial tensions
- Getting the required pressure gradients to overcome retaining forces
- Handle the remaining oil in a controlled way towards the production well.

During primary recovery, the natural pressure of the reservoir or gravity drives oil to the production wellbore with the aid of lifting pumps which push the oil to the surface. During primary recovery, only about 10 percent of a reservoir's original oil in place is typically produced.

Secondary recovery techniques extend the field's productivity by injecting gas or water to drive oil to the production wellbore, which increases the oil recovery by 20 to 40 percent of the original crude oil in place.

However, oil producers in the United States oil fields, have used tertiary, or enhanced oil recovery (EOR) techniques, which lead to potential 30 to 60 percent or more increase in the productivity of the oil reservoir (Alvarado and Manrique 2010). In addition, the easily extracted oil by primary recovery is continuously decreasing, while the remaining oil in the reservoir stays unharvested; thus, employing the enhanced oil recovery is crucial to maintaining a continuous oil supply. Secondly, sustainable energy resources are still in their infant step and have not yet proved to be able to meet the global energy demand (Wever et al. 2011).

According to Thomas (2008), about 7.0×10^{12} barrels of oil will stay in the crude oilfields after using the traditional methods of extracting crude oil. Water

soluble polymers have been used successfully in Chinese oilfields (Han et al. 1999; Li et al. 2008), the water-soluble polymers were used to improve the rheological properties of the liquid (Lake LW 1989).

Based on the viscoelastic specifications of the used polymers, a mathematical model was utilized to explore the effects of the polymer injecting mechanism in the EOR (Wang et al. 2001; Yin et al. 2003; Zhang and Yue 2008). Surfactants are added by injection to the liquid into the crude oil reservoir. The injection actually controls the properties of the oil and move the trapped crude oil by reducing the interfacial tension between the injected liquid and the crude oil (Sandersen 2012).

An important factor for the success of such recovery is the surfactant stability at the reservoir. Surfactants are sensitive to high temperature and high salinity; subsequently, surfactants which can resist these conditions should be used (Green and Willhite 1998).

Three broad categories of EOR have been found to be commercially successful to varying degrees: a- Thermal recovery, b- Gas injection and c- Chemicals injection (Alvarado and Manrique 2010). Below is a brief explanation for each kind:

2.4.1 Thermal Recovery

Steam injection, steam flooding, and Steam-Assisted Gravity Drainage (SAGD) have been used widely to recover heavy and extra-heavy oil production in sandstone reservoirs during last decades.

All the above methods involve the introduction of heat to lower the viscosity of the heavy oil and enhance its ability to flow through the reservoir.

Thermal enhanced oil recovery projects have been mostly used in Canada, the United States and Former Soviet Union (Hann et al. 1969; Ernandez 2009). Steam injection began approximately 50 years ago. Steam Assisted Gravity Drainage (SAGD) represents another important and current EOR thermal method to increase the amount of produced crude oil from oil sands. Due to SAGD applicability in reservoirs with high vertical permeability, this EOR process has received attention in countries with heavy and extra-heavy oil resources, such as Canada and Venezuela, both owning vast oil sands resources (Manrique et al. 2007). The role of temperature on the mechanism of capillary imbibition was investigated by (Babadagli 1995). A 3D capillary imbibition tests at a temperature range of 20-90 ^{o}C. Different types and a wide range of oil-water interfacial tension and viscosity ratios were used.

The author reported a reduction in interfacial tension and viscosity as temperature increased and a significant alteration in the rate of capillary imbibition. (Tang and Kovscek 2004) employed X-ray in computed-tomography (CT) scanner to study the heavy oil recovery from outcrop diatomite and field core. They experimented isothermal flows ranging between 20-180 ^{o}C.

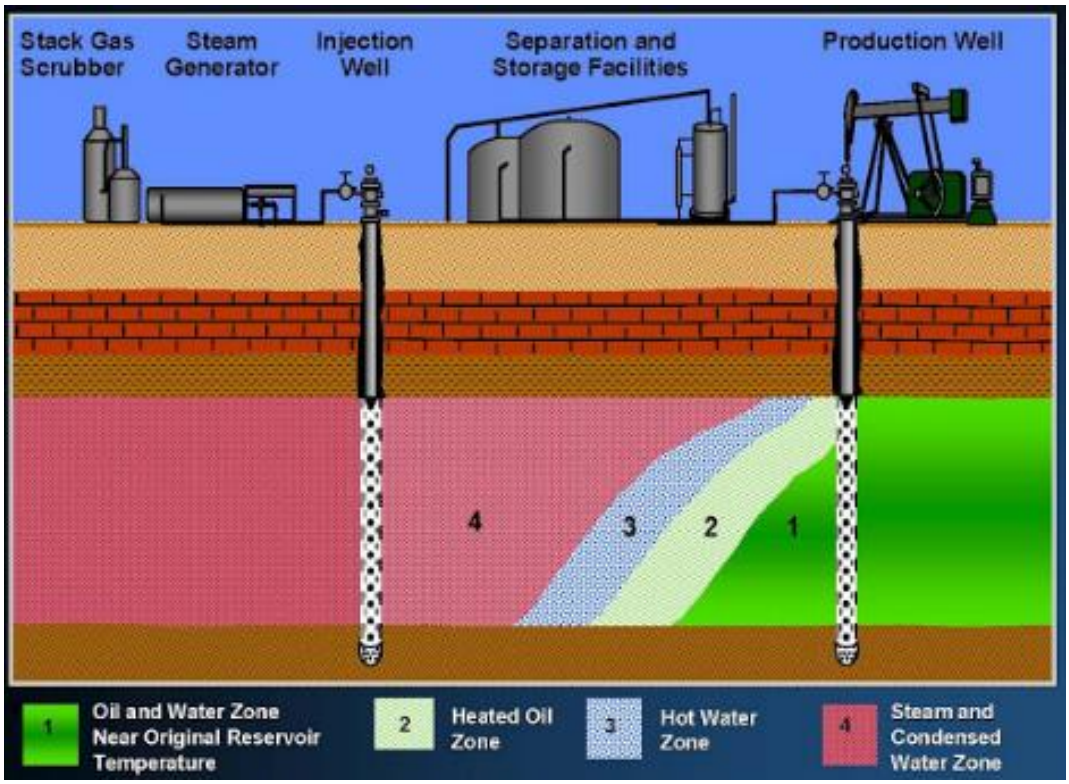

Figure 2.6 Typical steam injection process to lower oil viscosity.

They found that increasing temperature supported oil recovery due to the reduction in viscosity and altered wettability toward water wetness. A series of works targeting chalk-water-crude oil interactions were executed.

The researchers showed that in the oil- water-rock system, that the increase in temperature was playing an important role in improving the water wetness of oil-wet chalk. which resulted in the increase in oil recovery with a considerable reduction in interfacial tension and contact angle (Hamouda et al. 2004, Hamouda et al. 2008, Gomari et al. 2006, Karoussi et al. 2007, Karoussi et al. 2008).

A practical study performed on crude oil recovery from chalk rocks revealed that a reduction in oil recovery was associated with the temperature exceeding 80

^{o}C. This is due to the oil- water-rock system leaning toward oil wet instead of water wet (Hamouda and Karoussi 2008). The effect of transition temperature (explain more) on chalky limestone rock was investigated. The study showed wettability alternation toward water wet explain more (Al-Hadhrami and Blunt 2001). The role of temperature on the wettability alteration in oil-wet fractured carbonate reservoirs was investigated. By using hot-water injection or steam flooding, the temperature increases the wettability changes from oil-wet to water-wet (Al-Hadhrami and Blunt 2000).

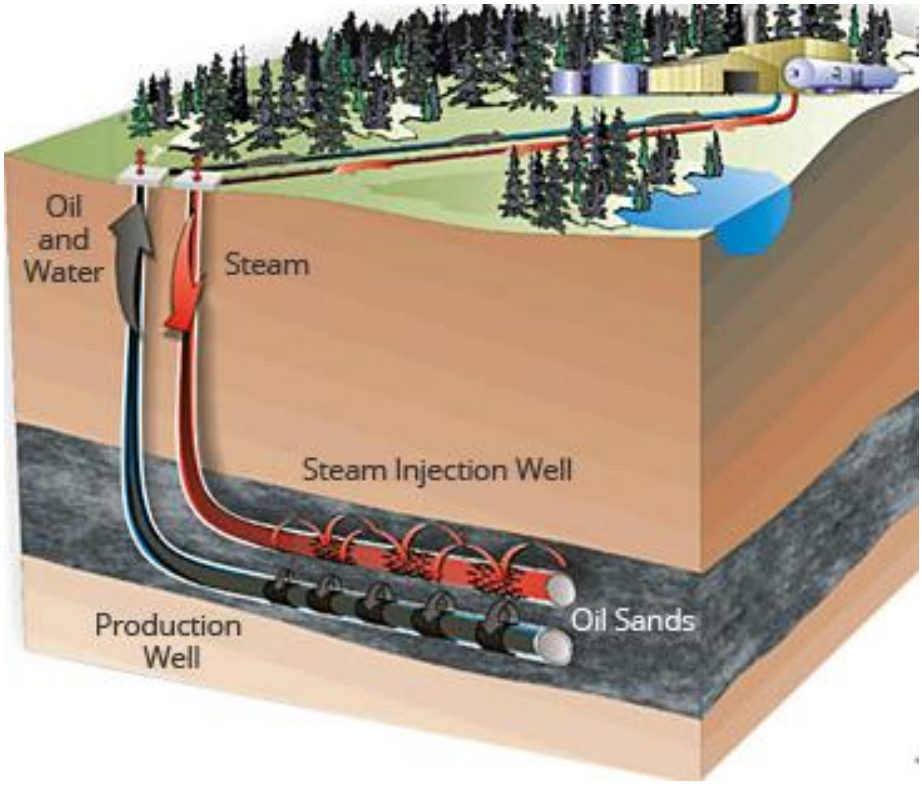

Figure 2.7 Steam assisted gravity drainage (SAGD) process.

2.4.2 Gas Injection

Which uses different types of gases such as nitrogen, natural gas, or carbon dioxide (CO_2) that increase the pressure in the reservoir to push additional oil to the wellbore, or by using other kinds of gases that dissolve in the oil to lower its viscosity and improves its flow rate. EOR gas flooding version considered the most widely used recovery methods of light, condensate and volatile oil reservoirs (Moritis 2008).

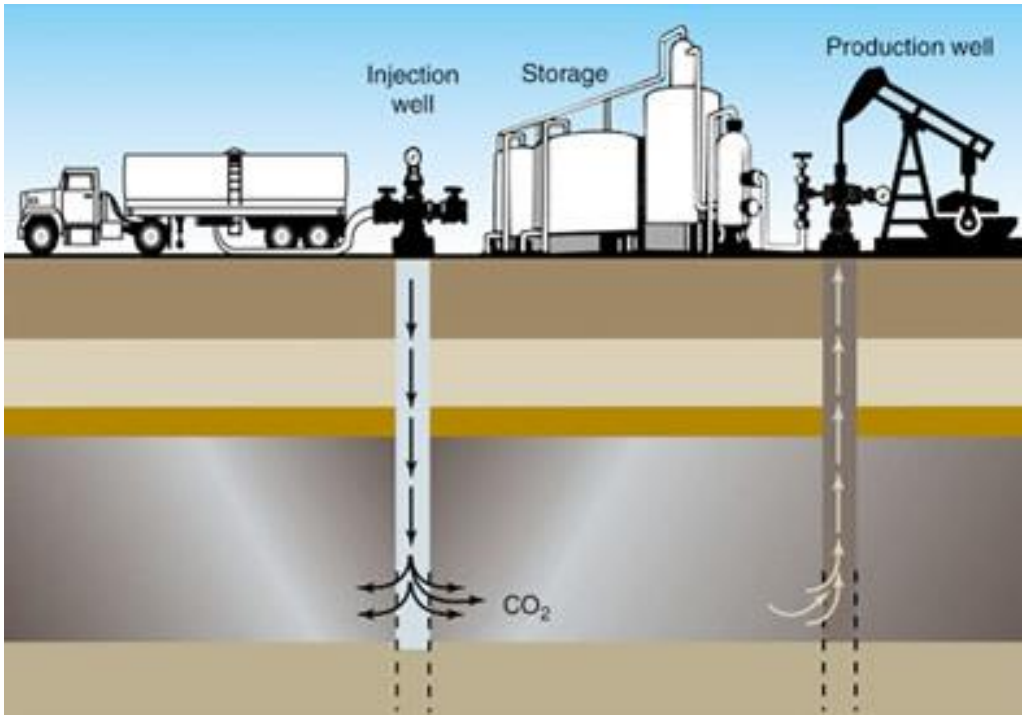

Figure 2.8 Gas injection method.

2.4.3 Chemicals Injection

Chemicals injection involves the use of long-chained molecules called polymers to increase the effectiveness of water floods, or the use surfactants to help lower the surface tension that often prevents oil droplets from moving through

a reservoir. When using surfactant flooding, the injected chemicals contain surface active agents, (surfactants), which are polymeric molecules used to lower the interfacial tension between the liquid surfactant solution and the residual oil. The most common type of surfactants used in this process contain a hydrophobic tail and a hydrophilic head (Sandersen 2012).

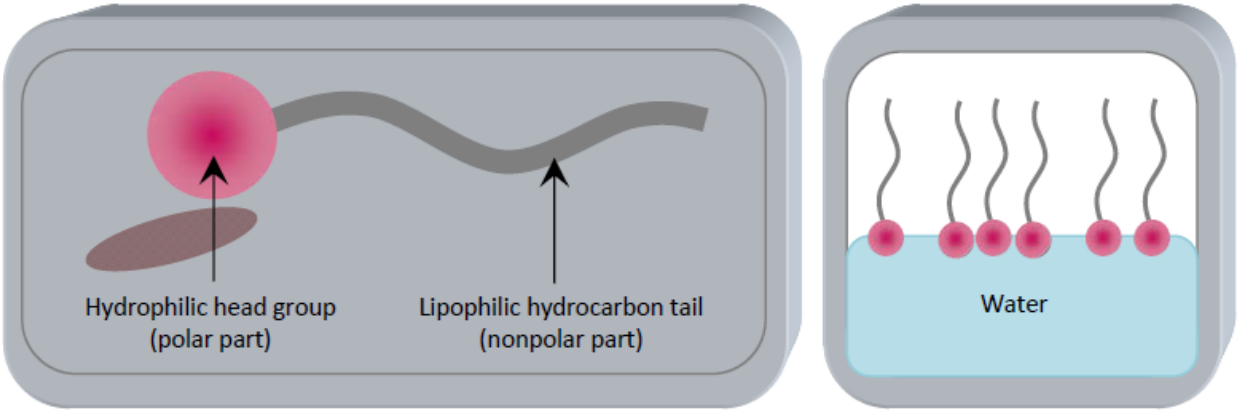

Figure 2.9 Surfactant molecule and surfactant orientation in water (Green and Willhite, 1998).

Opportunity

A special LBM model, which couples the effects of hydrodynamics, interfacial physics, surfactants effects and temperature is used for the investigation of the flow behavior of O/W emulsions with the goal of delineating the best practices for transporting these emulsions in circular ducts.

2.5 Machining Tool Cooling

Reducing the friction between the cutting tool edge and the workpiece and controlling the temperature and corrosion are the main functions of cutting fluid. As temperature increases to high levels, tool wear increases which has adverse

effects on tool life and machining accuracy (V.Dessoly et al. 2004). About 15–25% of production total cost is spent for coolant (Jem et al. 2002)

A cooling method was investigated, which uses liquid nitrogen in the process of material removal. The study focused on the liquid nitrogen effects on the cutting tool and workpiece material properties. The authors concluded that using liquid nitrogen cooling is one of the most favorable methods for material cutting operations because it can improve tools' life and surface finish by reducing tools' wear resulting from a proper control of the machining temperature (Yakup and Nalbant 2008).

An overview is proposed for studying of significant advances in techniques used to minimize the number of lubricants such as compressed air cooling, solid coolants-lubricants, cryogenic cooling, and high-pressure coolant. These techniques lead to increasing productivity, reducing friction, and heat generation (Sharma et al. 2009). Use of heat pipe during machining was proposed, and the effects of different heat pipe parameters such as length, diameter degree of vacuum, and material of heat pipe were studied. The researchers assumed that the cutting tool is subjected to static heating in the cutting zone, which justifies the practicality of using this cooling method in turning operations (Haq and Tamizharasan 2006).

Taguchi's Design of Experiments was used for optimizing the heat pipe parameters, and a confirmation test was conducted by using the fabricated heat pipe with the best values of parameters. The results of the study showed a

reduction by about 5% in temperature. This leads to an improved cutting tool life, surface finish, and minimization of wear. Finite element analysis results also predicted a reduction in temperature in the cutting zone and the heat transfer to the tool is effectively removed when a heat pipes are used (Haq and Tamizharasan 2006).

(Carlsaw and Jaeger 1959) presented an analytical model, which extends Jaeger's model (Jaeger 1942), The authors approximated the solution by a moving-band heat source for the chip and a stationary rectangular heat source for the tool for metal cutting. Appropriate boundary conditions and a non-uniform heat distribution along the tool were assumed. The calculated temperature showed an increase in temperature distribution on the two sides of the tool and the chip interface.

(Komanduri and Hou 2001) presented a model, which assumed a temperature rise distribution in metal cutting due shear plane heat source in the primary shear zone and a frictional heat source at the tool-chip interface. The model was used for two cases of metal cutting. The analytical results were found to be in good agreement with the experimental results, thus validating the model.

Opportunity

A different approach is suggested for studying tools' cooling. This approach focuses on attempting to understand the physics of the multiphase coolant, i.e. its transport properties relation with the flow conditions imposed during the cooling process to improve the process. Complex multiphase thermal-

surfactants LBM, which couples the energy equation with hydrodynamics and interface physics, is used in the simulation of the cooling of cutting tool using O/W emulsions.

CHAPTER 3 OUTLINE OF THE PRESENT WORK

3.1 Research objectives

This work aims to provide an efficient Gunstensen LBM based CFD model, capable of solving complex problems related to droplets behavior in shear and parabolic flows. This will be achieved through the following:

A model has been introduced to study enhanced oil recovery technique by an improved Lattice Boltzmann model, which includes thermal, contact angle and surfactant effects for breaking up trapped crude oil slugs and for capturing the underlying physics of transporting emulsions in confined three-dimensional ducts. The proposed model was used for enhancing the understanding of surfactants, thermal and contact angle effects on emulsions rheology and the pumping cost of transporting emulsions in miniature channels such as those encountered in the oil extraction fields. The model provides a tool for solving engineering problems at an extremely low cost compared to experimentation cost.

The model also used to investigate the oil in water (O/W) emulsions which are utilized extensively for cooling and lubricating cutting tools during parts machining. A robust Lattice Boltzmann (LBM) thermal-surfactants model, which provides a useful platform for exploring complex emulsions' characteristics under a variety of flow conditions, is used here for the study of the fluid behavior during conventional tools cooling. The transient thermal capabilities of the model are employed for simulating the effects of the flow conditions of O/W emulsions on the cooling of cutting tools.

3.1.1 Code development

• Build multi-component Gunstensen LBM model to couple the effects of five branches of physics which are:

- Hydrodynamics
- Physics of Interface
- Energy
- Surfactants
- Surface Energy and Contact Angle

3.1.2 Validation

The developed code should be tested and validated through comparison with other numerical, analytical and experimental results.

3.1.3Application

• Use the presented model in calculating and optimizing the energy required for the flow of single and multi-droplets in a confined flow.

• Use the presented model as a numerical platform for optimizing the use of thermal and surfactants effects in the oil industry and advancing the understanding of thermal emulsions.

• Use the presented model to study and optimize the cooling of the cutting tool.

3.2 Dissertation organization

Chapter 4:

A 3D LBM based model, which couples the energy equation with the flow hydrodynamics and surfactants-interfacial physics is presented and used for studying the effects of temperature on the rheology of surfactants-contaminated emulsions in simple shear and Couette flows. A quasi-steady thermal module characterized by updating the fluid transport properties as a function of the calculated fluid average temperature at each simulation time step is introduced.

The calculated average temperature is furthermore used for updating the surfactants elasticity and eventually correcting the emulsion's interfacial tension. The model is capable of reproducing the rheological behavior of emulsions from several experimental cases with the effects of temperature and surfactants. A transient thermal problem is also presented for exploring the potential of using the model in realistic engineering problems, thus providing a robust numerical model for simulating complex flow phenomena. The three-way coupling of hydrodynamics, surfactants and thermal energy is evaluated by showing its effects on the flow behavior of surfactants laden droplet under Couette flow conditions.

Chapter 5:

In this section, 2D and 3D thermal lattice Boltzmann models are coupled with a temperature dependent interfacial tension and contact angle modules to study the combined multi-physics effects on oil/water system. The thermal-capillary effects have a direct impact on the transport properties of crude oil. The

model static contact angles on two channels with different surface energies and at various temperatures were validated by comparison with the results of the mathematical model. The model was also used to simulate the dynamic behavior of oil/water system flowing between two parallel plates. Oil slugs and droplets attached to the upper and lower walls were investigated for improving the understanding of the underlying physics of the secondary and tertiary extraction process of trapped crude oil in wells. The model was then extended to simulate 3D oil/water slug system, and the same previous validation procedures were adopted. Effects of temperature and contact angle on the flow of slug and droplets inside confined channel were studded to assess the required power to push them inside the channel.

Chapter 6:

The 2D model which was proposed in chapter 5 was amended further to include surfactants dependent contact angle. The model was used to study the combined effects of temperature, surfactants and contact angle on the movement of slugs and droplets of oil in water (O/W) system flowing between two parallel plates. It was also shown that adding surfactants at the elevated temperature the power to transport the mixture diminished remarkably.

Chapter 7:

The 3D LBM based model, which presented in chapter 4 is used for studying the effects of temperature on the rheology of surfactants-contaminated emulsions in Poiseuille flow. The model used to examine the effects of changing the

temperature on emulsion rheology, average flow velocity, surfactant distribution, leading droplet deformation index and the transient temperature effects.

Furthermore, the effects of changing emulsion volume fractions, source term and surfactant concentration on the are studied. Finally, the power number was calculated to get an indication of the pumping efficiency in different situations.

Chapter 8:

Presents a summary of the research findings and suggests some future recommendations.

CHAPTER 4 HYBRID QUASI-STEADY THERMAL LATTICE BOLTZMANN MODEL FOR STUDYING THE RHEOLOGY OF SURFACTANTS CONTAMINATED EMULSIONS

Thermal conditions determine the outcome of the physical and transport properties of emulsions during their various processing phases. A better understanding of the intricate relationship between thermal, surfactants and hydrodynamics can help in the optimization of these processes during the production of emulsions. To investigate the outcome of coupling thermal, surfactants and hydrodynamics on emulsions behavior, a robust quasi-steady thermal-surfactants numerical scheme is presented and used here. To validate the model, the rheological behavior of oil-in-water system was investigated. The numerical results matched well the experimental results of the similar oil-in-water system under steady-state thermal conditions. Furthermore, it is shown that the proposed numerical model can handle cases with transient thermal conditions while maintaining good accuracy.

4.1 Numerical Method

4.1.1 LBM and the Gunstensen Model

The Bhatnagar-Gross- Krook (BGK) lattice Boltzmann (LBM), single-relaxation model used in this work, is derived from the Boltzmann kinetic equation:

$$\frac{df}{dt} + \xi \cdot \nabla f = -\frac{1}{\lambda}(f - f^{eq}) \tag{4.1}$$

Where f is the density distribution function, ξ is the macroscopic velocity, f^{eq} is the equilibrium distribution function, and λ is the physical relaxation time. Equation

(4.1) is first discretized by using a set of velocities $\{\xi_i\}$ confined to a finite number of directions, and this leads to the following equation:

$$\frac{df_i}{dt} + \boldsymbol{\xi}_i \cdot \nabla f_i = -\frac{1}{\lambda}(f_i - f_i^{eq}) \tag{4.2}$$

The equivalent velocity vectors (lattice links) for the D3Q19 BGK used here are shown in Fig 4.1 These links have the following endpoints coordinates:

$$\begin{aligned}
&e_0(0,0,0); e_1(-1,-1,0); e_2(-1,0,-1); e_3(-1,0,0);\\
&e_4(-1,0,1); e_5(-1,1,0); e_6(0,-1,-1); e_7(0,-1,0);\\
&e_8(0,-1,1); e_9(0,0,-1); e_{10}(1,1,0); e_{11}(1,0,1);\\
&e_{12}(1,0,0); e_{13}(1,0,-1); e_{14}(1,-1,0); e_{15}(0,1,1);\\
&e_{16}(0,1,0); e_{17}(0,1,-1); e_{18}(0,0,1);
\end{aligned} \tag{4.3}$$

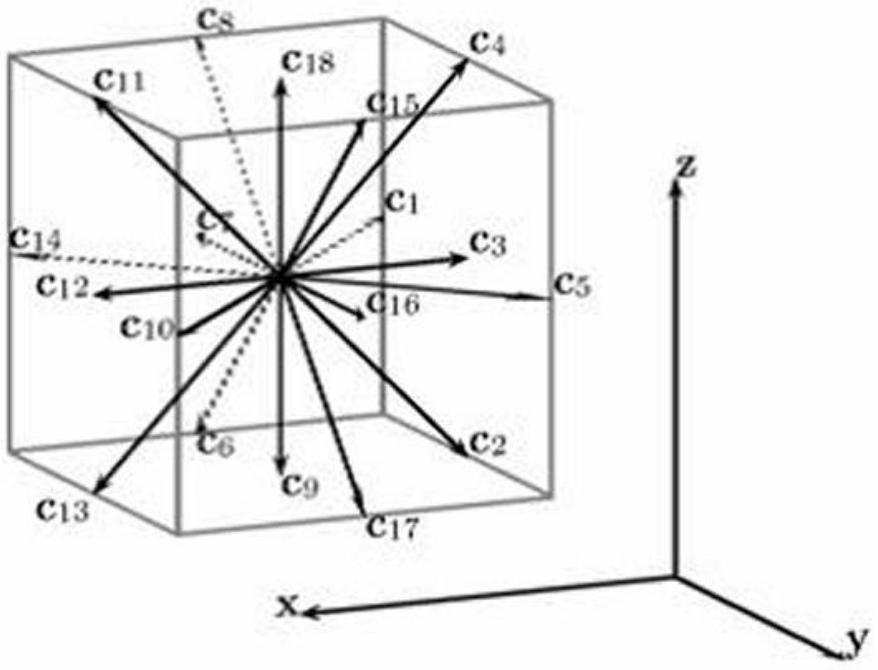

Figure 4.1 Velocity vectors for the D3Q19 lattice Boltzmann method used in this model.

In the multi-component LBM Eq. (4.2) is further discretized in the lattice space and time and this leads to the following:

$$\hat{f}_i^q(x,t+\delta_t) = f_i^q(x,t) - \frac{1}{\tau^q}[f_i^q(x,t) - f_i^{q,eq}(\rho,\rho u)] + \phi_i(x) \tag{4.4}$$

The lattice space δ_x and the lattice time step δ_t are taken as unity and their ratio $c = \delta_x / \delta_t = 1$, while q refers to the light and heavy fluids. The lattice speed of sound $c_s = c/\sqrt{3}$ is used for determining the fluid pressure by $p = \rho c_s^2$, and the lattice relaxation time is $\tau = \lambda / \delta_t$. The kinematic viscosity is derived from the relaxation time by the following formula:

$$\nu = (\tau - 0.5) c_s^2 \delta_t \tag{4.5}$$

The Gunstensen multi-component model uses a color-blind total density distribution function given by:

$$f_i(\boldsymbol{x},t) = f_i^L(\boldsymbol{x},t) + f_i^H(\boldsymbol{x},t) \tag{4.6}$$

Where $f_i^L(\boldsymbol{x},t)$ and $f_i^H(\boldsymbol{x},t)$ are the light and the heavy fluid density distribution functions respectively. For tracking the liquid interface, a phase field is given by the following relation:

$$\begin{aligned} \rho^N(\boldsymbol{x},t) &= \frac{\rho^L(\boldsymbol{x},t) - \rho^H(\boldsymbol{x},t)}{\rho^L(\boldsymbol{x},t) + \rho^H(\boldsymbol{x},t)} \\ \rho^L(\boldsymbol{x},t) &= \sum_0^{Q-1} f_i^L(\boldsymbol{x},t); \rho^H(\boldsymbol{x},t) = \sum_0^{Q-1} f_i^H(\boldsymbol{x},t) \end{aligned} \tag{4.7}$$

where Q depends on the dimension and the type of the model, ρ^L is the density of the lighter fluid, ρ^H is the density of the heavier fluid.

To tolerate a density ratio up to 20 between the constituent fluids, the collision rule is modified from the original Gunstensen model. The various fluids are collided separately using the following equilibrium distribution functions in Eq.(4.4):

$$f_i^{L,eq} = \rho^L \omega_i [1 + \frac{3}{c^2} c_i.u + \frac{9}{2c^4}(c_i.u)^2 - \frac{3}{2c^2} u.u]$$
$$f_i^{H,eq} = \rho^H \omega_i [r_i + \frac{3}{c^2} c_i.u + \frac{9}{2c^4}(c_i.u)^2 - \frac{3}{2c^2} u.u] \quad (4.8)$$

Where $r_i = \begin{Bmatrix} 3-2\zeta, \rightarrow i = 0 \\ \zeta, \rightarrow i \neq 0 \end{Bmatrix}$, $\zeta = \frac{\rho^L}{\rho^H} = \frac{(c_s^H)^2}{(c_s^L)^2}$ is the density ratio and $c_i = e_i / \delta_t$ is the lattice velocity in the i^{th} direction, ω_i are the weighting constants for the various lattice links:

$$\omega_i = [1/3; 1/36; 1/36; 1/18; 1/36; 1/36; 1/36; 1/18; 1/36; 1/18; 1/36; 1/36; 1/18; 1/36; 1/36; 1/36; 1/18; 1/36; 1/18] \quad (4.9)$$

u and ρ are the macroscopic velocity and density, respectively.

The surface tension is created by the method of Lishchuk et al., which imposes a normal force at the interface as follows:

$$F(x) = -\frac{1}{2} \alpha K \nabla \rho^N \quad (4.10)$$

Where α is the interfacial tension parameter, K is the interface curvature and ρ^N is the phase field.

The effects of thermal and surfactants leading to anisotropic interfacial tension, necessitate the use of spatially varying lattice source term $\phi_i(x)$. The

interfacial tension is imposed by correcting the macroscopic velocity $\boldsymbol{u}$ prior to the collision step and applying the source term $\phi_i(\boldsymbol{x})$ after collision, for perturbing the interface prior to the segregation step. The method is due to Guo et al. where the corrected velocity and the source term are given by:

$$\boldsymbol{u} = \frac{1}{\rho}\left[\sum_{i=1}^{8} f_i \boldsymbol{c}_i + \frac{1}{2}\boldsymbol{F}(\boldsymbol{x})\right]$$
$$\phi_i(\boldsymbol{x}) = k_2\omega_i\left(1-\frac{1}{2\tau}\right)\left[\frac{\boldsymbol{c}_i-\boldsymbol{u}}{c_s^2}+\frac{(\boldsymbol{c}_i\cdot\boldsymbol{u})\boldsymbol{c}_i}{c_s^4}\right]\cdot\boldsymbol{F}(\boldsymbol{x}) \tag{4.11}$$

where $k_2\delta_{\alpha\beta\gamma} = \sum_i \omega_i e_{i\alpha}e_{i\beta}e_{i\gamma}$. This produces a more accurate interfacial tension, which equals to the appropriate value of the interfacial tension α.

After the collision, the color-blind density distribution function is invoked as follows:

$$\hat{f}_i(\boldsymbol{x},t) = \hat{f}_i^{L}(\boldsymbol{x},t) + \hat{f}_i^{H}(\boldsymbol{x},t) \tag{4.12}$$

$\hat{f}_i^{q}$ refers to post-collision distribution functions.

The segregation of the fluids happens after the collision step. D'Ortona et al., implemented a formulaic approach for the segregation of the mixture after the collision as follows:

$$\hat{\bar{f}}_i^{L}(\boldsymbol{x},t+\delta_t) = \frac{\rho^L}{\left(\rho^L+\rho^H\right)^2}\hat{f}_i(\boldsymbol{x},t+\delta_t) + \beta\frac{\rho^L\rho^H}{\left(\rho^L+\rho^H\right)^2}\omega_i\cos(\theta_f-\theta_i)\,|\boldsymbol{c}_i|$$
$$\hat{\bar{f}}_i^{H}(\boldsymbol{x},t+\delta_t) = \hat{f}_i(\boldsymbol{x},t+\delta_t) - \hat{\bar{f}}_i^{L}(\boldsymbol{x},t+\delta_t) \tag{4.13}$$

where θ_f and θ_i are the polar angle of the color field, and the angle of the velocity link respectively, β is the segregation parameter. $\hat{\hat{f}}_i^L$ and $\hat{\hat{f}}_i^H$ are the post-collision post-segregation distribution functions of the light and heavy fluids, respectively.

The two fluids can have different viscosities. This requires the use of various relaxation times in Eq. (4.5). The interface is made of a fluid mixture; therefore, its viscosity is determined by:

$$\nu_{eff} = (\tau_{eff} - 0.5)c_s^2\delta_t = \left(\frac{R}{R+B}\right)\nu_R + \left(\frac{B}{R+B}\right)\nu_B \tag{4.14}$$

The streaming step follows the segregation of the fluids by the following formulae:

$$\begin{aligned} f_i^L(\boldsymbol{x} + \boldsymbol{c}_i\delta_t, t+\delta_t) &= \hat{\hat{f}}_i^L(\boldsymbol{x}, t+\delta_t) \\ f_i^H(\boldsymbol{x} + \boldsymbol{c}_i\delta_t, t+\delta_t) &= \hat{\hat{f}}_i^H(\boldsymbol{x}, t+\delta_t) \end{aligned} \tag{4.15}$$

The macroscopic density and momentum are obtained from the distribution function as follows:

$$\rho = \sum_{i=0}^{Q-1} f_i = \sum_{i=0}^{Q-1} f_i^{eq} \tag{4.16}$$

$$\rho\boldsymbol{u} = \sum_{i=1}^{Q-1} \boldsymbol{c}_i f_i = \sum_{i=1}^{Q-1} \boldsymbol{c}_i f_i^{eq} \tag{4.17}$$

4.1.2 The Surfactant Model

The general time-dependent surfactant convection-diffusion equation is given by:

$$\partial_t \Gamma + \nabla_s \cdot \left(\boldsymbol{u}_s \Gamma \right) + K \Gamma u_n = D_s \nabla_s^2 \Gamma \tag{4.18}$$

Where $\partial_t \Gamma$ accounts for the temporal change in the interface surfactant concentration, $\nabla_s \cdot \left(\boldsymbol{u}_s \Gamma \right)$ is the convection term, $k \Gamma u_n$ is to describe the effects of change in the interface morphology on the surfactant concentration distribution and $D_s \nabla_s^2 \Gamma$ is the diffusion term.

The combination of all the terms of Eq. (4.18) through some mathematical steps, leads to the following simplified equation:

$$\begin{aligned} &\partial_t \Gamma + C_1 \partial_x \Gamma + C_2 \partial_y \Gamma + C_3 \partial_z \Gamma + C_4 \Gamma + C_5 \partial_{xx}^2 \Gamma + C_6 \partial_{yy}^2 \Gamma + C_7 \partial_{zz}^2 \Gamma \\ &+ C_8 \partial_{xy}^2 \Gamma + C_9 \partial_{xz}^2 \Gamma + C_{10} \partial_{yz}^2 \Gamma = 0 \end{aligned} \tag{4.19}$$

where the coefficients C_j are expressed as follows:

$$\begin{aligned} &C_1 = u_{sx}; C_2 = u_{sy}; C_3 = u_{sz} \\ &C_4 = \left(n_y^2 + n_z^2 \right) \partial_x u_{sx} + \left(n_x^2 + n_z^2 \right) \partial_y u_{sy} + \left(n_x^2 + n_y^2 \right) \partial_z u_{sz} \\ &- n_x n_y \left(\partial_y u_{sx} + \partial_x u_{sy} \right) - n_x n_z \left(\partial_z u_{sx} + \partial_x u_{sz} \right) \\ &- n_y n_z \left(\partial_z u_{sy} + \partial_y u_{sz} \right) + \left(K u_x n_x + K u_y n_y + K u_z n_z \right) \\ &C_5 = (n_x{}^2 - 1) D_s; C_6 = (n_y{}^2 - 1) D_s; C_7 = (n_z{}^2 - 1) D_s \\ &C_8 = 2 n_x n_y D_s; C_9 = 2 n_x n_z D_s; C_{10} = 2 n_y n_z D_s \end{aligned} \tag{4.20}$$

D_s Is the surface diffusion constant which can be determined in lattice units $\left[lu^2 ts^{-1} \right]$ from the following relationship: $Pe_s = \dot{\gamma} R_0^2 / D_s$. Pe_s is the surface Péclet number, $\dot{\gamma}$ is the shear strain rate and R_0 is the droplet radius. n_x, n_y, n_z Are the

components of the normal to the interface, K is the interface curvature and u_{sx}, u_{sy}, u_{sz} are the components of the tangential velocity of the interface.

The surfactant concentration effect on the interfacial tension of the droplet can be imposed by the non-linear Langmuir surfactant equation of state:

$$\sigma = \sigma_0 + RT\Gamma_\infty \ln\left(1 - \frac{\Gamma}{\Gamma_\infty}\right) \tag{4.21}$$

Where R is the universal gas constant and T is the temperature in Kelvin. The equation can be rewritten for convenience as follows:

$$\sigma = \sigma_0 \left[1 + E_0 \ln\left(1 - \Gamma^*\right)\right] \tag{4.22}$$

where σ_0 is the surface tension of a clean droplet, E_0 the surfactant elasticity given by: $E_0 = \frac{\Gamma_\infty RT}{\sigma_0} < 1$ (4.23)

The following ratio calculates the dimensionless surfactant concentration:

$$\Gamma^* = \frac{\Gamma}{\Gamma_\infty} \tag{4.24}$$

where Γ_∞ is the saturation surfactant concentration which can be derived from Eq. (4.23) in lattice units as $\Gamma_\infty = \frac{E_0\sigma_0}{RT}\left[lmol/lu^2\right]$ and the product $RT = 1/3$ is used for the isothermal thermal LBM, which is reasonably applicable to the proposed quasi-steady thermal model since the temperature does not change within a one-time step.

4.1.3 The Quasi-Steady Thermal Model

Assuming small variations in the thermal fluid properties and no phase change due to temperature rise or fall, the following energy equation is used for the calculation of the flow temperature profile:

$$\partial_t T + \nabla \cdot (\boldsymbol{u} T) = D_{ifs} \nabla^2 T + \varphi \tag{4.25}$$

In Eq. (4.25) $\partial_t T$ Accounts for the fluid temperature change in time $\nabla \cdot (\boldsymbol{u} T)$ is the convection term and $D_{ifs} \nabla^2 T$ is the diffusion term, φ accounts for the flow viscous dissipation. The governing equation can be writing after some mathematical manipulation as follows:

$$\partial_t T + D_1 \partial_x T + D_2 \partial_y T + D_3 \partial_z T + D_4 T + D_5 \partial^2_{xx} T + D_6 \partial^2_{yy} T + D_7 \partial^2_{zz} T + D_8 = 0$$

where,

$$D_1 = u_x; D_2 = u_y; D_3 = u_z; D_4 = \partial_x u_x + \partial_y u_y + \partial_z u_z; D_5 = D_6 = D_7 = -D_{ifs}$$

$$D_8 = -\frac{\mu}{\rho c_p}\left[\begin{array}{l} 2(\partial_x u_x)^2 + 2(\partial_y u_y)^2 + 2(\partial_z u_z)^2 + (\partial_x u_y + \partial_y u_x)^2 + (\partial_y u_z + \partial_z u_y)^2 \\ + (\partial_z u_x + \partial_x u_z)^2 - \frac{2}{3}(\partial_x u_x + \partial_y u_y + \partial_z u_z)^2 \end{array}\right] \tag{4.26}$$

D_{ifs} is the thermal diffusivity, u_x u_y , u_z are the fluid velocity components and μ is the dynamic viscosity.

The conversion of the physical units into lattice Boltzmann units, requires identifying the properties of the specific fluids used for the simulation. The next step is to convert through a multiplier the kinematic viscosities at different

temperatures into lattice viscosities ν_q, which values are selected such that the relaxation time of the suspending liquid for oil in water emulsions is always slightly greater than 0.5 i.e. $\tau = \nu_q / c_s^2 \delta_t + 0.5 > 0.5$, while maintaining the same physical viscosity ratio. For example, for SAE 50 oil in water the kinematic viscosity multiplier is chosen as 31,715.81, which leads to water lattice kinematic viscosity $\nu_{lat-w@50C} = 0.0171$ and a relaxation time $\tau = 0.551$. While the oil lattice kinematic viscosity $\nu_{lat-o@50C} = 4.08$ and the ratio $\nu_{lat-o@50C} / \nu_{lat-w@50C} = 238.59$, which is the same as the physical ratio of SAE50 to water.

Values of physical conductivity k and temperature T are used without modification. The final step is to find the right multipliers for the specific heat c_p and density ρ in order to get the appropriate thermal diffusivity by $D_{ifs} = k / (\rho c_p)$ which yields the correct physical Prandtl number $P_r = \nu / D_{ifs}$. For example, the density multiplier for SAE50 in water is set to 0.002317 and the multiplier for specific heat is 0.013608. This leads to lattice thermal diffusivity of water $D_{ifs-w-lat@50C} = 5.08 \times 10^{-3}$ and the lattice Prandtl number $P_r = 0.0171 \times 10^3 / 5.08$, which matches the physical Prandtl number. Table-1 presents the values of water and SAE-50 motor oil used in the subsequent simulations.

LBM properties such as kinematic viscosity, specific heat and thermal diffusivity are curve fitted as functions of temperature. The curve fitting equations are, eventually used in the code for modifying the fluids properties at the beginning

of each time step during the simulation. This is done by evaluating these properties with respect to a calculated average temperature of the fluid domain at the respective time step. The one-third Simpson double integral is used for the calculation of the average temperature by the following:

$$T_{av} = \frac{1}{X}\sum_{X}\left(\frac{1}{A_{yz}}\iint_{A_{yz}} T dydz\right) \tag{4.27}$$

where X is the number of nodes in the horizontal direction and A_{yz} is the area of the domain in the yz directions.

The presented approach for varying the fluid properties due to thermal effects assumes that these properties are invariant within the same time step. This allows the use of the Boussinesq approximation to track the effects of changes in density due to the change in temperature. The Boussinesq approximation is implemented in the proposed LBM as a constant source term by the following equation:

$$\phi_i = \omega_i \frac{1}{k_2} F \cdot \boldsymbol{c}_i;\ F = \rho\left[1-\psi\left(\Delta T\right)\right]g \tag{4.28}$$

where ρ is the local density, ψ is the average thermal expansion coefficient, ΔT is the temperature difference between the initial condition and g is gravity.

Table 4.1: Fluids physical and LBM properties.

SAE-50 Oil and Water Physical and Lattice Properties								
	Temperature C°	**Density Kg/m³**	**Dynamic Viscosity Kg/m.s**	**Kinematic Viscosity m²/s**	**Specific Heat J/kg.k°**	**Conductivity W/m.k°**	**Prandtl Number**	**Thermal Diffusivity m²/s**
Water	10	999.570	1.266E-03	1.267E-06	4089.70	0.588	8.803	1.439E-07
	20	997.780	9.772E-04	9.794E-07	4076.40	0.605	6.587	1.487E-07
	30	995.180	7.773E-04	7.811E-07	4070.20	0.619	5.108	1.529E-07
	40	991.800	6.354E-04	6.407E-07	4067.30	0.632	4.086	1.568E-07
	50	987.680	5.319E-04	5.385E-07	4066.00	0.644	3.358	1.604E-07
LBM								
	10	2.316	9.307E-02	4.018E-02	55.65	0.588	8.803	4.565E-03
	20	2.312	7.181E-02	3.106E-02	55.47	0.605	6.587	4.716E-03
	30	2.306	5.712E-02	2.477E-02	55.39	0.619	5.108	4.850E-03
	40	2.298	4.670E-02	2.032E-02	55.35	0.632	4.086	4.973E-03
	50	2.288	3.908E-02	1.708E-02	55.33	0.644	3.358	5.086E-03
	Temperature C°	**Density Kg/m³**	**Dynamic Viscosity Kg/m.s**	**Kinematic Viscosity m²/s**	**Specific Heat J/kg.k°**	**Conductivity W/m.k°**	**Prandtl Number**	**Thermal Diffusivity m²/s**
SAE-50 Oil	26.67	875.249	4.589E-01	5.243E-04	1800.32	0.131	6.324	8.289E-05
	37.78	868.041	2.191E-01	2.524E-04	1989.99	0.130	3.358	7.516E-05
	48.89	860.992	1.178E-01	1.368E-04	2041.90	0.129	1.864	7.339E-05
	60	854.425	6.903E-02	8.080E-05	2093.40	0.128	1.127	7.172E-05
LBM								
	26.67	2.028	33.719	16.627	24.50	0.131	6.324	2.629E-03
	37.78	2.011	16.100	8.005	27.08	0.130	3.358	2.384E-03
	48.89	1.995	8.658	4.340	27.79	0.129	1.864	2.328E-03
	60	1.980	5.073	2.563	28.49	0.128	1.127	2.275E-03

The temperature effect on the initial surface tension of the mixture constituent fluid q can be calculated by the following empirical equation (Katayama and Tokohu 1916, Guggenheim and Chem 1945):

$$\sigma_q^{(T)} = \sigma_q^* \left(1 - \frac{T}{T_{c,q}}\right)^n \tag{4.29}$$

Considering a value $n \approx 1.0$ for the empirical factor, it is reasonable to assume a linear surface tension-temperature relationship and σ_q^* is calculated using the following equation:

$$\sigma_q^* = \sigma_{q,0}\left(1+\frac{T_0}{T_{c,q}-T_0}\right) \tag{4.30}$$

where $T_{c,q}$ is the critical temperature at which the surface tension vanishes, $\sigma_{q,0}$ is the initial surface tension of each fluid and T_0 is the initial mixture temperature the following equation calculates the interfacial tension:

$$\sigma_0^{(T)} = \sigma_a^{(T)} + \sigma_b^{(T)} - 2\chi\sqrt{\sigma_a^{(T)}\sigma_b^{(T)}} \tag{4.31}$$

Where χ is a dimensionless ratio of energies of adhesion and cohesion of the two phases, $\sigma_a^{(T)}$ and $\sigma_b^{(T)}$ are then calculated from Eq. (4.29) Temperature dependent surface tensions for the suspending and suspended fluids, respectively. The values for the initial surface tensions σ_q are selected in such a way, that the resultant interfacial tension σ_0 leads to the correct physical capillary number of the flow:

$$Ca = \frac{R_0\mu_m\dot{\gamma}}{\sigma_0} \tag{4.32}$$

The initial surface tension σ_0 is used in the calculation of the correct flow's Eötvös number:

$$Eo = \frac{\Delta\rho g\ell^2}{\sigma_0} \tag{4.33}$$

Where ℓ is the characteristic length and g is acceleration due to the gravity of the matrix and $\Delta\rho$ is the density difference. The Eötvös number is used for finding the correct value for the model acceleration g .

The effect of the thermal changes in the surfactants concentration is imposed through modifying the surfactants elasticity from Eq. 4.23 by:

$$\frac{E_0}{E_o^{(T)}} = \frac{T_0}{T} \tag{4.34}$$

Where T is the local varying temperature, $E_o^{(T)}$ is the temperature dependent surfactant elasticity.

4.1.4 The Hybrid Thermal-Surfactants Model

The proposed Gunstensen LBM is used for determining the hydrodynamic characteristics of the mixture and for tracking the fluid-fluid interface. During initialization of the LBM, the initial surfactant concentration Γ_i is imposed on the interface with a controllable thickness. The thermal boundary condition is also applied during this step.

After determining the LBM velocity components $\left(u_x, u_y, u_z\right)$, the droplet curvature and the interface normal components $\left(k, n_x, n_y, n_z\right)$, the tangential components $\left(u_{sx}, u_{sy}, u_{sz}\right)$ of the interface velocity are calculated. These variables are after that, used for the derivation of the surfactants-diffusion Eq. (4.19), and the governing energy equation Eq. (4.25). Both equations are solved by a finite difference scheme resolved on the same spatial lattice grid.

The coupling back of the thermal and surfactant effects on the fluid LBM is executed in the following order:

The temperature dependent surface tensions of both fluids are updated by:

$$\alpha_q^{(T)} = \alpha_{q,0}\left(1+\frac{T_0}{T_{c,q}-T_0}\right)\left(1-\frac{T}{T_{c,q}}\right)^n \tag{4.35}$$

The temperature dependent interfacial tension is then calculated by:

$$\alpha_0^{(T)} = \alpha_a^{(T)} + \alpha_b^{(T)} - 2\chi\sqrt{\alpha_a^{(T)}\alpha_b^{(T)}} \tag{4.36}$$

The temperature dependent surfactants elasticity is determined by:

$$E_o^{(T)} = \frac{E_0 T}{T_0} \tag{4.37}$$

The final update of the interfacial tension is given by:

$$\alpha = \alpha_0^{(T)}\left[1+E_0^{(T)}\ln\left(1-\Gamma^*\right)\right] \tag{4.38}$$

The local surface tension parameter in the proposed model is thus non-isotropic, and it changes based on the outcome of Eq. (4.35 - 4.38).

4.2 Simulation and Discussion

A domain consisting of $145\times65\times125\left[lu^3\right]$ was used in the two subsequent simulations. The geometrical similitude of 125 lattice units for 2.5 × 10^{-4} meters was utilized to mimic the average gap between the cone and plate rheometer from the experimental work of (Kundu *et al*. 2015). For kinematic viscosity multiplier of 31,715.8, the ratio of lattice's shear strain rate to physical shear strain rate was calculated as follows:

$$\frac{\dot{\gamma}_{phys}}{\dot{\gamma}_{lat}} = \frac{h_{lat}^2 \upsilon_{phys}}{h_{phys}^2 \upsilon_{lat}} = 7,882,505 \tag{4.39}$$

The surfactant covered droplets initial radii were set to $R_0 = 15\left[lu\right]$. Shear strain rate with a range $1.27\times10^{-7} \le \dot{\gamma} \le 1.27\times10^{-5}\left[ts^{-1}\right]$ was imposed by moving the top wall at different velocities with respect to the stationary bottom wall in the direction shown in Fig 4.1 the following equation can describe the velocity:

$$\boldsymbol{u}^{\infty}\left(\boldsymbol{x}\right) = \begin{pmatrix} 0 & 0 & -\dot{\gamma} \\ 0 & 0 & 0 \\ 0 & 0 & 0 \end{pmatrix} \cdot \boldsymbol{x} \tag{4.40}$$

The periodic boundary condition was used in all other directions. The inverse of the relaxation times $\Omega_i = 1/\tau_i$ for the suspended (oil) droplets and their ambient (water) fluid from Eq. 4.5, were calculated by using the values for the temperature dependent kinematic viscosities for oil and water by the following curve fits, respectively:

$$\Omega_O = 1/\left\{\left[123.5\times\exp\left(-0.08984\times \mathrm{T_F}\right) + \ 11.83\times\exp\left(-0.02956\times \mathrm{T_F}\right)\right]\times\ 3.0 + 0.5\right\}$$
$$\Omega_W = 1/\left\{\left[0.03265\times\exp\left(-0.04379\times \mathrm{T_F}\right) + 0.02087\times\exp\left(-0.008796\ \times \mathrm{T_F}\right)\right]\times\ 3.0 + 0.5\right\}$$

(4.41)

This leads to an average oil to water kinematic viscosity ratio $\lambda = 314.7$ for temperature range $25c^o \le T \le 60c^o$. The average density ratio between the two fluids is $\zeta = 0.873$ for the same temperature range.

Under simple shear flow, the following formula was used for calculating the effective viscosity of o/w emulsions:

$$\frac{Q}{W}=\frac{Uh}{2}+\frac{h^3}{12\mu_{eff}}\frac{\Delta p}{\ell}$$
$$\mu_{eff}=\frac{h^3}{6}\frac{W}{\left(2Q-UhW\right)}\frac{\Delta p}{\ell} \quad (4.42)$$

where, μ_{eff} is the effective dynamic viscosity, U is the linear velocity of the top wall, h is the height of the domain, W is the domain width, and Q is the volumetric flow rate. The pressure difference $\Delta p=\bar{p}_{x_2}-\bar{p}_{x_1}$ is the difference between the averaged pressure values over two surface areas, which entrapped the suspended fluid. The distance between the two selected surface areas for measuring the pressure difference due to the restriction of the suspending flow by the suspended phase is $\ell=x_2-x_1$. The selection of the surface areas was motivated by the desire of avoiding the effects of the periodic boundary conditions on the pressure measurements.

The volumetric flow rate was calculated by using the averaged horizontal velocity over the whole domain. The recorded effective viscosity was taken after stabilization of the flow conditions as shown in (Fig 4.2B). It is worth noting that non-Newtonian fluids such as emulsions subjected to simple shear flow without imposed pressure gradient behave similarly as those of Newtonian fluids placed under Coquette flow conditions with backflow producing pressure gradient as presented in Fig 4.2A In Couette flow the ratio $P=-\frac{h^2}{2\mu U}\frac{\partial p}{\partial x}$ influences the dimensionless velocity distribution. The average calculated ratio in the shear flow simulations was $P\approx -0.46$.

The lattice surface tensions for the two fluids were set such that a mixture interfacial tension of $\sigma_0 = 1.03\times10^{-3}\ \left[lf \times lu^{-1}\right]$ was derived from Eq. (4.31). This led to Eötvös number $Eo = 2.3\times10^{-3}$ for average temperature $T_{av} = 40c^o$, which matched the physical Eötvös number of the o/w emulsion from the experimentation.

Acceleration due to gravity used in the Eötvös formula is $g = 5.46\times10^{-9}\ \left[lu\times ts^{-2}\right]$, and the average thermal expansion coefficient $\beta = 2.6\times10^{-4}\ lt^{-1}$ was imposed in the Boussinesq assumption for a mixture volume fraction $\phi_{o/w} \approx 10\%$. The initial surfactant elasticity was determined as $E_0 = \Gamma_0 RT/\sigma_0 = 0.5$, in which Γ_0 is the initial surfactants' concentration. The non-linear Langmuir equation of state was used in the simulations with $\Gamma^* = \Gamma/\Gamma_0 = 2.5$. The diffusion constant was set to $D_s = 3.9\times10^{-3}\left[lu^2 ts^{-1}\right]$, for a range of capillary numbers $0.00309 \le Ca \le 0.309$.

4.3 Effects of the Shear Strain Rate on the O/W Emulsion Effective Viscosity at Different Temperatures

Validation of the proposed model was executed by comparing the simulation results with the experimental work of (Kundu *et al*. 2015). The experimental research group presented their rheological measurements for several sets of O/W emulsions at different temperatures, volume fractions, and shear strain rates.

The simulations domain contained nine droplets resulting in a volume fraction $\phi_{o/w} \approx 10\%$ similar to emulsion set one from the referenced work.

Four different static temperatures were used 25°C, 30 °C, 40 °C and 50 °C as these were the conditions of the experimental work. The simulation results are presented in Fig 4.3 in conjunction with the results, which were extracted from the experimental measurements (with permission of Kundu et al.).

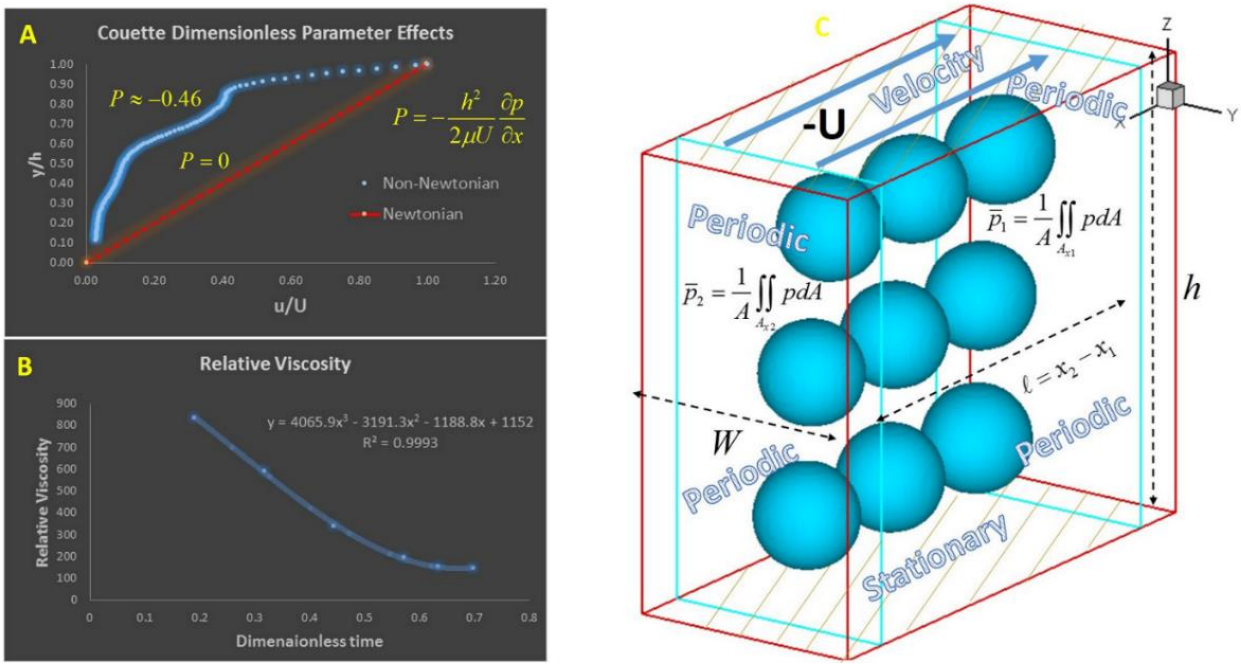

Figure 4.2 Explanation of the imposed boundary conditions and the method used for calculating the effective viscosity of the mixture in a shear flow domain.

The simulations stopped at shear strain rate $\dot{\gamma} = 10\left[s^{-1}\right]$ since the integrity of the simulations outcome would have been compromised for any lower values due to some inherent spurious effects generated by the method used for imposing the surface tension in the base Gunstensen LBM model.

The simulation results show a reasonable agreement with the experimental outcomes. The slight discrepancies may have been due to the difference in the physical properties of the light petroleum oil used in the experimental work and SAE-50 oil employed in the simulation. SAE-50 oil was used here since the properties of such oil is easier to find in the literature, and it has close dynamic viscosity to that of the light petroleum oil.

It is evident from both the experimental and the simulation results that O/W emulsions exhibit shear thinning behavior. The power law was used to describe this rheological behavior. Dividing the effective viscosity by the viscosity of the suspending fluid at the respective temperature leads to the relative viscosity. The power law for the described oil rheological behavior is given by:

$$\mu_{rel} = \frac{\mu_{eff}}{\mu_m} \propto \dot{\gamma}^{(n-1)} \tag{4.43}$$

where the coefficient *n* was calculated from the various simulated cases as $0.466 \leq n \leq 0.517$.

4.4 Shearing of O/W Emulsions with Induced Heat by Constant Temperature Walls

The effective viscosity results from the work of (Kundu et al. 2015) for volume fraction $\phi_{o/w} \approx 10\%$, shear strain $\dot{\gamma} \approx 10\ s^{-1}$ and $\dot{\gamma} \approx 25\ s^{-1}$, were rearranged in plots representing the effective viscosity as a function of temperature.

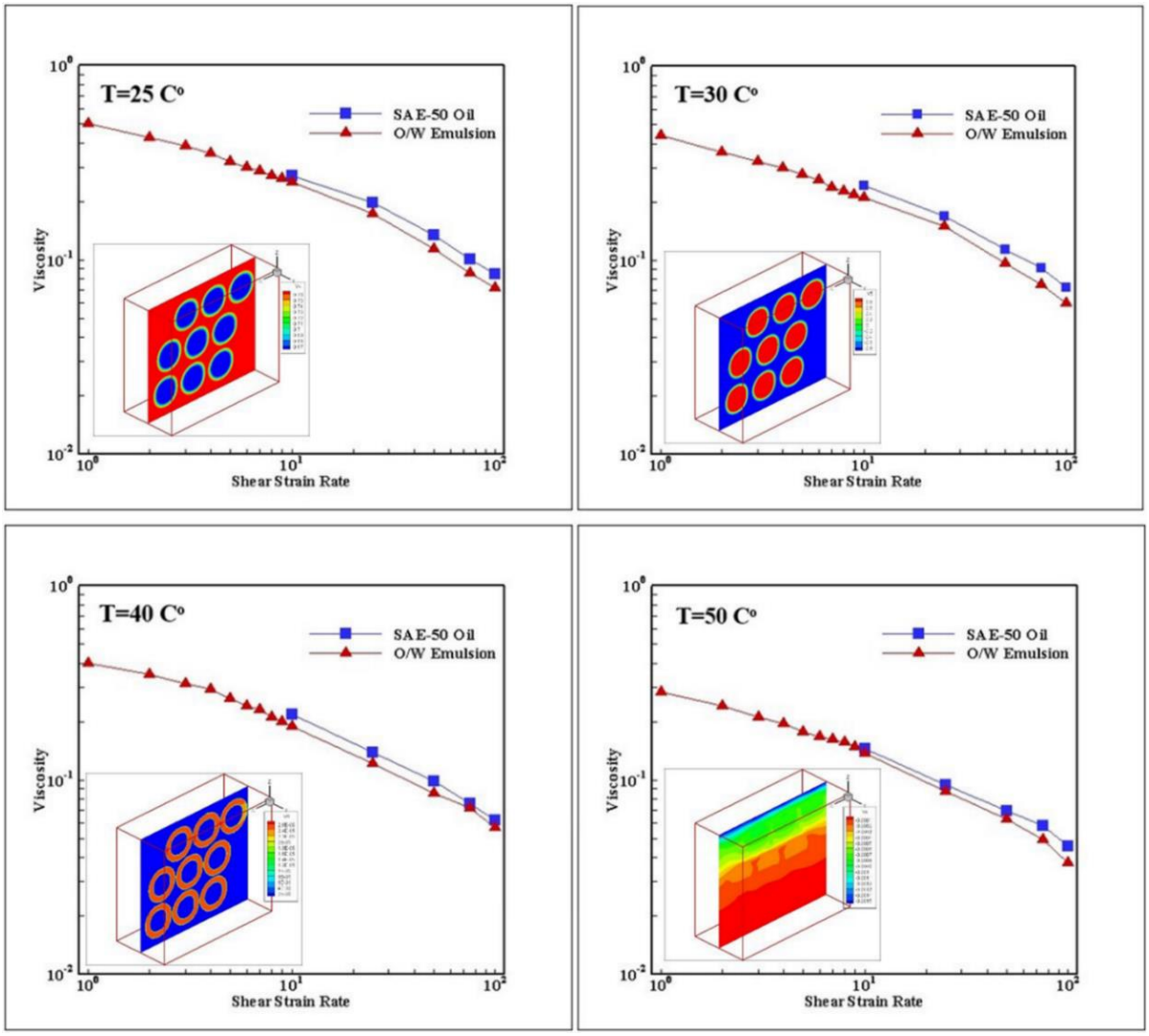

Figure 4.3 Comparison of the simulation results for the effective viscosity for four cases of surfactants covered droplets with different temperatures. The insets from top left to low right are density; phase filed, surfactants distribution and horizontal velocity contours as slices in the xz plane.

The objective here was to test the transient capabilities of our model. The simulation domain described in the previous section was used with walls set to a constant temperature $T_{wall} \approx 80^{o}C$ and the initial fluid temperature to $T_{init} \approx 20^{o}C$. The temperature difference between the wall and the fluid led to mixture's warm

up in time. The values of the effective viscosity were measured from the simulations at the desired temperatures for comparison with the rearranged experimental data and the previous simulation results. The results from the simulations were superimposed on the experimental graphs for both shearing strain rates, respectively. The results presented in the upper section of Fig 4.4, show good agreement with the experimental work.

The relative temperature and relative viscosity with respect to dimensionless time of the O/W emulsions are shown in the bottom section of Fig 4.4. The dimensionless time was calculated as $t_{\dim} = \dot{\gamma}_{lat} \times t_{lat}$, where $\dot{\gamma}_{lat}$ is the lattice shear strain rate and t_{lat} is the lattice time step. The relative temperature was calculated as the ratio of the measured temperature from the simulations to the initial mixture temperature $T_{\dim} = T / T_{init}$. The relative viscosity was calculated as the measured effective viscosity normalized by the initial matrix viscosity $\mu_{rel} = \mu / \mu_w$.

The bottom section of Fig 4.4 shows that as the temperature propagates from the wall into the mixture, the average dimensionless temperature increases, and the relative viscosity decreases. The viscosities were curve fitted with respect to time as per the following two-dimensional first-order polynomials:

$$\begin{aligned} \mu_{rel} &= 282.1 - 802.4 \times t_{\dim} + 18.16 \times T_{\dim} \\ \mu_{rel} &= 330.3 - 6.452 \times t_{\dim} - 109.1 \times T_{\dim} \end{aligned} \tag{4.44}$$

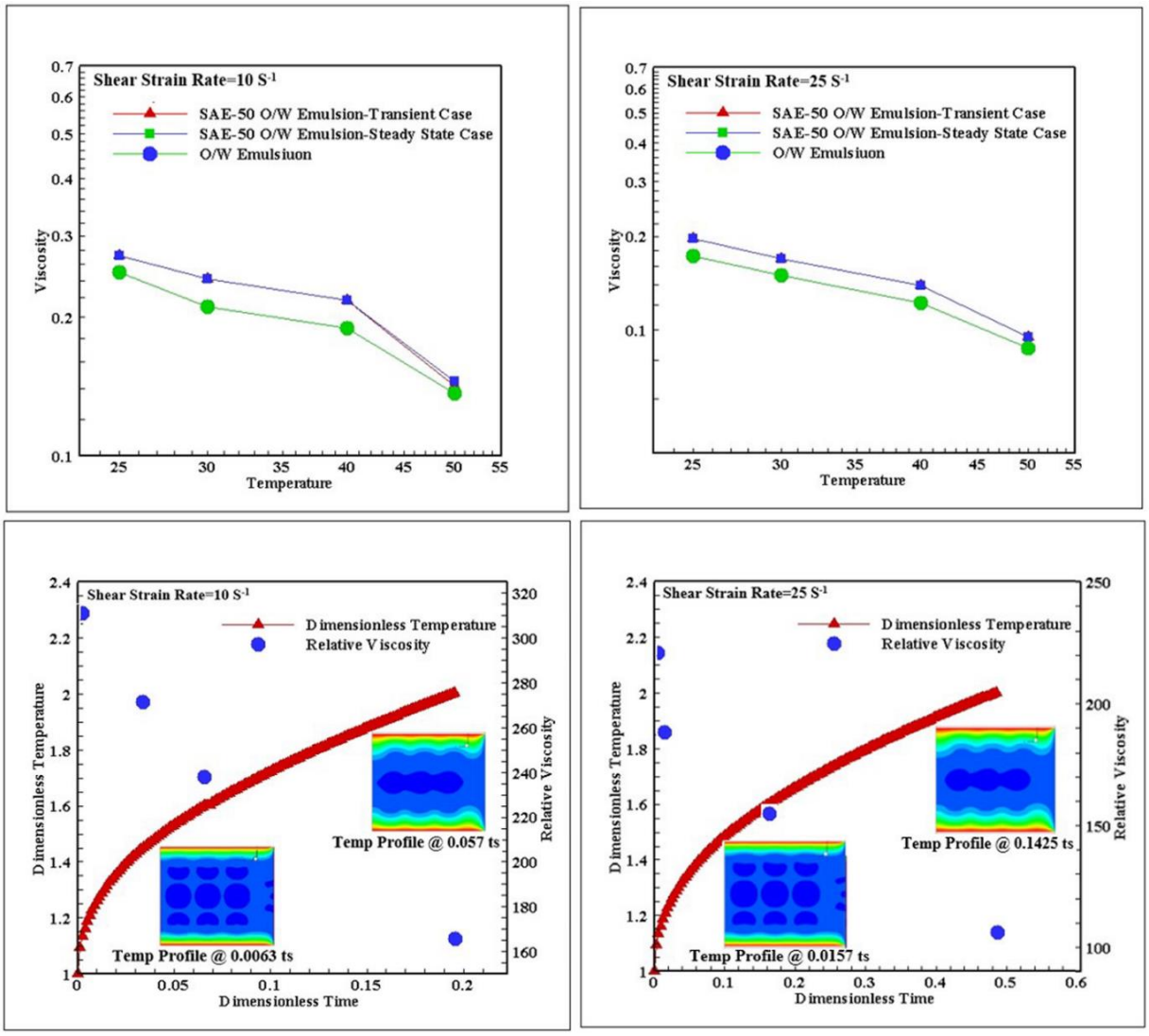

Figure 4.4 Top: Effective viscosity dependence on changing fluid temperature. Bottom: Dimensionless temperature and relative viscosity dependence on dimensionless time. The insets are showing the temperature contours slices for two different dimensionless time steps.

4.5 Surfactants Distribution and Droplet Morphology Dependence on the Fluid's Temperature

In this section, the surfactants distribution for two temperatures T=25ºC and T=50ºC used in the validation of the model are examined with a shear strain rate $\dot{\gamma} = 100\left[s^{-1}\right]$. A quick observation of the surfactants distribution in both simulations shows that the effects of the interface change in the surfactants governing equation Eq. (18) is negligible because of the high viscosity ratio of the O/W emulsions.

As shown in Fig 4.5. For temperature T=25ºC, the surfactants distribution is unique to each of the droplets in the domain.

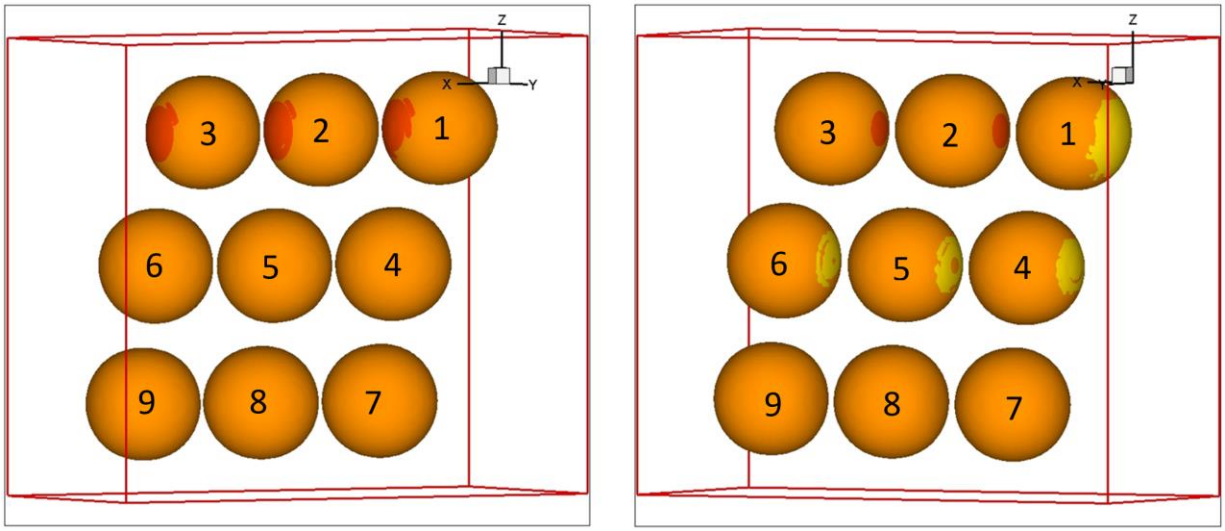

Figure 4.5 Front and back contours for the surfactants distribution at T=25ºC.

At lower matrix temperature, the upper row of droplets is moved at relatively higher velocity due to its proximity to the driving wall and due to the matrix higher viscosity. The leading droplets designated by 1, exhibits surfactants depletion from its frontal zone, and accumulation at its back.

This is due to the difference between the leading average droplet velocity (moving as one body) and the surrounding matrix average velocity affected by the shear flow gradient. The second and third droplets in the top row, exhibit rather different behavior, where an accumulation at the frontal and rear zones is observed. These droplets are moving in the wake of the leading droplet, and their top surfaces are subjected to a higher matrix velocity, than their own velocities, which leads to an accumulation at their frontal section. The velocity difference is reversed at the lower surfaces of the first-row droplets, which justifies the surfactants accumulation at the rear of the droplets.

All droplets in the second row are experiencing depletion in their surfactants concentration at their frontal zones and almost even distribution in all other zones.

The middle row droplets motion is due to the viscous shearing caused by the movement of the top droplets' row, which is more influential than the effects of the shear flow velocity gradient. This difference in velocity justifies the surfactants distribution of the second-row droplets. The droplets of the third row are not affected by the flow since they are closer to the stationary wall.

The surfactants distribution at T= 50^{o}C is much less aggressive. This is because the matrix viscosity at T= 50^{o}C is about 4.62 times less than the viscosity at T= 25^{o}C. Depletion of the frontal zone of the leading drop in the first row is evident due to the velocity differential; however, there is no frontal accumulation on the second and third droplets of the first row as a consequence of the matrix

lower viscosity. The droplets of the first raw accumulate surfactants at their rear zones due to the low velocity of the matrix flow below them.

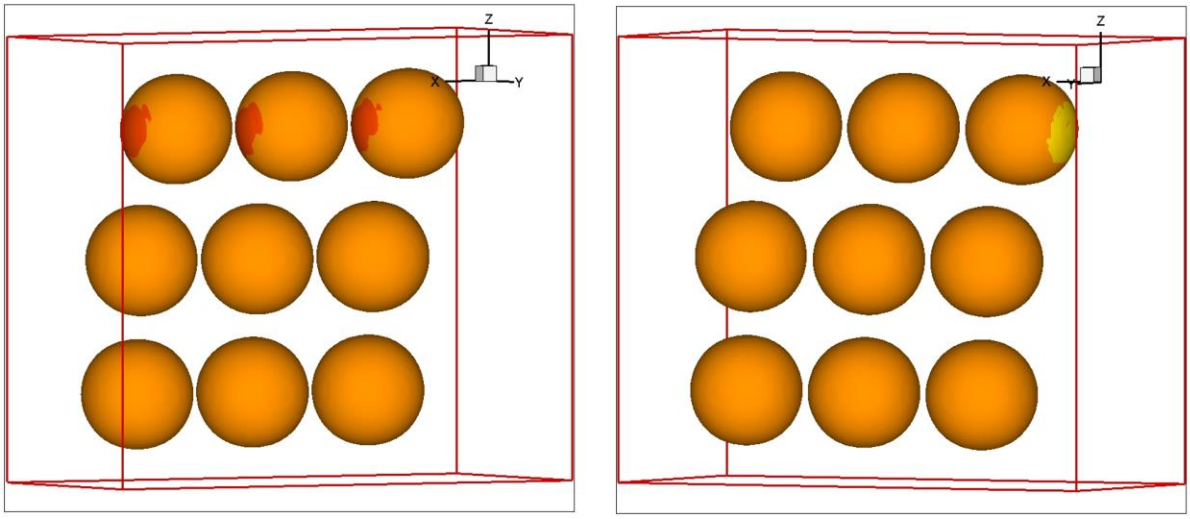

Figure 4.6 Front and back insets for the surfactants distribution at T=50^{o}C.

Under the simulation conditions, it is clear that the thermal effects overshadow the surfactants effect on the rheology of the O/W emulsion. This is evident from the fact that although the droplets in the lower temperature simulation move faster than those of, the higher temperature simulation, this does not lead to a greater thinning of the emulsion as it was shown in Fig. 3. On the other hand in high viscosity ratio O/W, surfactants are not effective in helping to deform the suspended phase nor to force it to tilt and align with the matrix flow direction for favorable rheological effects.

4.6 Cutting Tool Cooling Simulation

4.6.1 Transient Thermal Case Study

Oil in water emulsions is used extensively during parts machining for simultaneous cooling and lubrication of the parts and the cutting tools. In this simulation, a mixture with volume fraction $\phi_{o/w} \approx 10\%$ is used for simulating the conditions of cooling and lubrication during machining. Simple shear flow with pressure gradient (Couette flow) can be observed in a simple hypothetical case of linear milling of a piece of metal, where cooling is generously provided both externally and internally between the cutting tool and the part to avoid extreme temperatures of the cutting tool and to prevent coolant phase change. Couette flow can simulate this simple case.

This simulation is to investigate the effects of the driving flow pressure gradients and flow direction with respect to the cutting tool direction of movement, on the resulting coolant outlet temperature and its relative viscosity. In case of an undisturbed flow between two parallel plates the pressure gradient per unit length leads to the following average velocity:

$$V_{av} = \frac{h^2 \Delta p}{3W \mu \ell} \tag{4.45}$$

The viscosity used in Eq. (4.5) Is that of the suspending fluid at an initial liquid, an average temperature of 25 ^{o}C resulting and wall temperature of 80 ^{o}C. This equation helps to calculate an average reference velocity for comparison with the velocity of the top wall for dimensionless analysis of the posed problem. The

resulting dimensionless velocity is given by $U_{ds} = V_{av}/U$, which indicates the ratio of the undisturbed velocity between two parallel plates and the velocity of the top wall in a simple shear flow.

Two values for pressure drop per unit length are used with the top plate moving in opposite directions, which leads to the following four conditions characterized by $U_{ds} = \pm 0.142$ and $U_{ds} = \pm 0.284$. The dimensionless time is calculated by multiplying the lattice time step with the shear strain rate due to the top plate movement as $T_{ds} = T_{lat}\dot{\gamma}$

From Fig 4.7 it is clear that reversing the top plate direction has a little effect on the temperature outcome; however, and in both pressure gradient cases the relative viscosity is substantially higher when the pressure has driven flow is counteracting the effect of the top plate movement (counter flow). A careful observation of Eq. (4.37) used in the calculation of the effective viscosity is helpful in explaining this rheological behavior.

In the case of counter flow condition, the volumetric flow rate is much smaller than that of the opposite condition. Since the effective viscosity is inversely proportional to the volumetric flow rate, it is expected that the viscosity will increase upon a decrease in flow rate. It is important to state that under counter flow condition the pressure drop is higher than that of the parallel flow. This should contribute to an increase in the effective viscosity since it is directly proportional to the pressure

drop; however, the magnitude of the pressure drop increase is not comparable to that of the flow rate decrease.

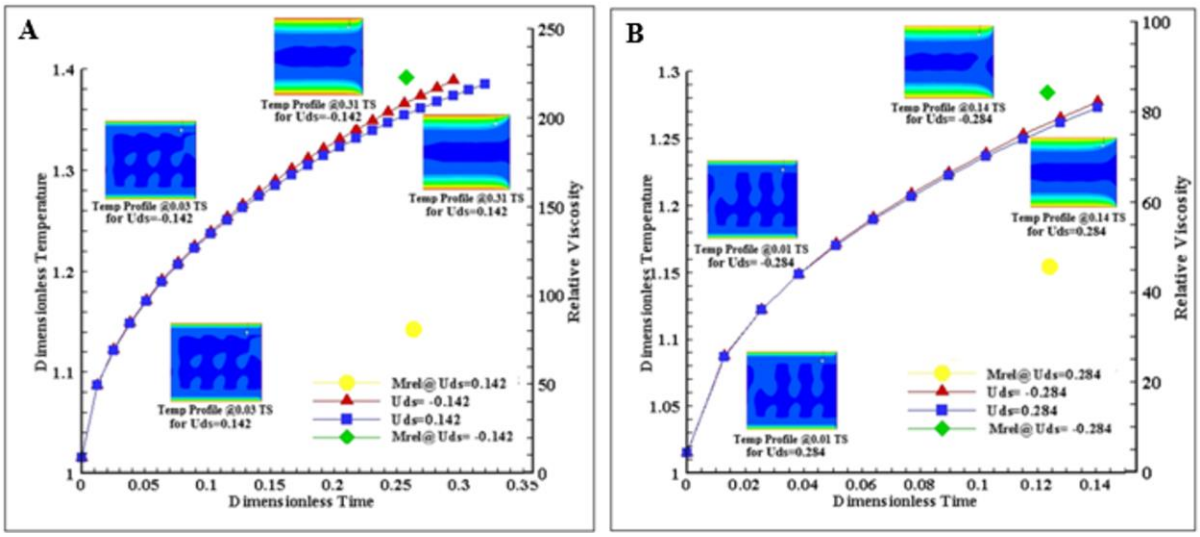

Figure 4.7 Temperature profile as a function of dimensionless time as prescribed in the text and evaluation of the relative viscosities for all cases at the determined dimensionless time. The insets are for the temperature contours. A- for upper plate velocities=∓0.142, B- for top plate velocities=∓0.284.

Comparing the temperature profiles and relative viscosities in Fig 4.6 leads to the conclusion that the outlet temperatures for the higher dimensionless velocity U_{ds} cases is slightly lower and that has to do with the emulsion smaller residence time inside the channel. The relative viscosity is greater for lower dimensionless U_{ds} cases due to lower volumetric flow rate.

The following equation can assess the heat rejection in all cases:

$$\dot{Q} = \rho Q c_p \Delta T \tag{4.46}$$

The results from the simulations show that it is practical to use counter flow configuration to ensure better lubricity during machining. It is also beneficiary to

increase the flow rate since the heat rejection ratio for the two counter flow cases is calculated at dimensionless $T_{ds} = 0.1408$ as follows:

$$R_{\dot{Q}} = \frac{\dot{Q}_{U_{ds}=-0.284}}{\dot{Q}_{U_{ds}=-0.142}} = 3.07 \tag{4.47}$$

4.6.2 Surfactant Distribution for Transient Thermal Case Study

It is shown from Fig 4.8, that the distribution of surfactant on the droplets in the simulation domain is mainly affected by the presence of the moving and the stationary walls. The following observations can be reported:

a- The upper surfaces of the top three droplets are subjected to higher shear flow with negative top wall velocity. This is evident from the diminishing surfactants concentration at the top surface. The effect is less influential with the top plate moving in the positive direction. In the case of higher flow driving pressure gradient, the reduction of surfactant concentration starts affecting the rear surface due to the fact that the droplets tend to resist the movement in the direction of the top plate.

b- The bottom surfaces of the bottom three droplets are mainly affected by the pressure gradient induced flow, and they are indifferent to the top wall motion and its direction. The surfactants concentration distribution is almost identical in all cases. The last bottom droplets show concentration decrease at the rear surface, which is due to the flow expanding towards the periodic boundary.

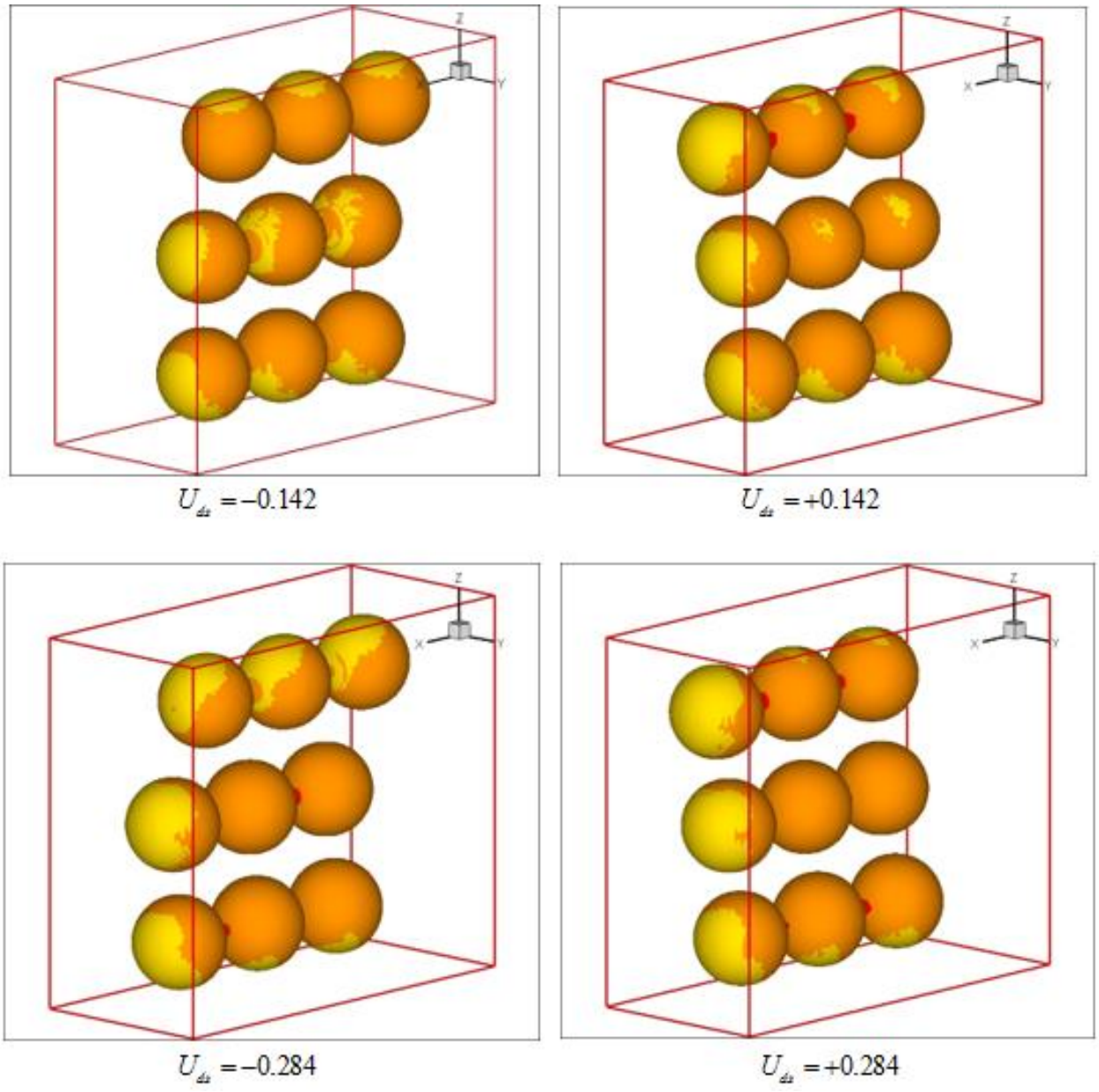

Figure 4.8 Surfactant distribution at same dimensionless time $T_{ds} = 0.1408$ for the four different dimensionless velocities.

c- The two central frontal droplets at low-pressure gradient driven flow to show some surfactant concentration reduction at the rear and top side surfaces

depending on the movement direction of the top plate. This is an indication of the influence of the top wall movement on the surfactants distribution. This is not observed with the higher-pressure gradient because, in the case of negative top wall velocity, the pressure induced pressure neutralizes the effects of the top wall. In the case of positive top wall velocity, the absence of walls does not allow a change in the surfactants concentration. The rear central droplets show a consistent decrease in surfactants concentration due to the pressure induced flow expansion at the periodic boundary.

CHAPTER 5 INVESTIGATING THE EFFECTS OF THERMAL AND SURFACE ENERGY ON THE FLOW CHARACTERISTICS OF OIL IN WATER MIXTURE BETWEEN PARALLEL PLATES AND IN CONFINED FLOW

A hybrid quasi-steady thermal lattice Boltzmann model with a temperature dependent contact angle is presented here. The model was used to study the combined effects of temperature, and contact angle on the movement of slugs and droplets of oil in water (O/W) system flowing between two parallel plates and in 3D confined flow. The model static contact angle due to the deposition of the O/W droplet on a flat surface with simulated hydrophilic characteristic at different fluid temperatures, matched very well the proposed theoretical calculation.

Furthermore, the model was used to simulate the dynamic behavior of droplets and slugs deposited on the domain's upper and lower surfaces, while subjected to parabolic flow conditions. The model accurately simulated the contact angle hysteresis for the dynamic droplets cases. It was also shown that at elevated temperatures the required power to transport the mixture diminished remarkably. The aim is to improve our understanding of the underlying physics associated with the secondary and tertiary extraction process of trapped crude oil in wells by injecting hot water.

5.1 Numerical Method

5.1.1 The Surface Tension Temperature Depended Model

The temperature dependent surface tension used here was presented in the work of Ganesan et al.

$$\sigma(T_f) = \sigma_{ref} - C_1(T_f - T_{ref}) \tag{5.1}$$

The value for C_1 was calculated by using physical data for oil in water system shown in Table 5.1.

Table 5.1: Interfacial tensions at different temperatures

Temperature (°C)	Interfacial Tension (N/m)
0	0.0271
10	0.0253
20	0.0235
30	0.0217
40	0.0199
50	0.0181
60	0.0163
70	0.0145
80	0.0127

The kinematic viscosity is given by:

$$\nu = (\tau - 0.5)c_s^2\delta_t \tag{5.2}$$

To use Eq. (5.2) for the simulation, the lattice initial surface tension σ_0 was selected such that the lattice Eötvös number matched the physical number given by:

$$Eo = \frac{\Delta\rho g \ell^2}{\sigma_0} \tag{5.3}$$

Where ℓ is the characteristic length and g is acceleration due to the gravity of the matrix and $\Delta\rho$ is the density difference.

5.1.2 The Contact Angle Temperature Depended Model

Venkatesan et al. derived the following theoretical temperature dependent contact angle equation:

$$\theta_d\left(T_F\right)=\cos^{-1}\left(\frac{\cos\theta^{ref}}{1-\frac{C_1}{\sigma_{ref}}\left(T_F-1\right)}\right) \tag{5.4}$$

where θ_d is the temperature dependent dynamic contact angle, θ^{ref} is the equilibrium contact angle at the reference temperature and σ_{ref} is the interfacial tension at the reference temperature.

The contact angle in the Gunstensen LBM can be achieved by assigning a phase field value for the wall. The calculated angles from Eq. (5.4). For several reference temperatures and contact surfaces, were used for determining the appropriate phase field values for the targeted contact angles. These values were curve fitted using second order, and exponential polynomial formulas and the fitted curves equation was eventually utilized in the code for simulating a variety of cases.

5.2 Flow Between Two Parallel Plates Simulation and Discussion Without Surfactants

A two-dimensional (2D) domain representing a flow between two plates was used in the subsequent simulations. Three configurations were executed in the following simulations.

The first consisted of $71\times31\left[lu^2\right]$ domain and a central droplet radius $R=8\left[lu\right]$ m deposited on the lower surface. The objective was to investigate the

conformance of the temperature dependent static contact angle to the theoretical calculation results.

The second configuration was consisted of $140 \times 20\left[lu^2 \right]$ to simulate the flow of one and two oil slugs attached to the top and bottom surfaces at different static temperatures.

The last configuration consisted of $311 \times 49\left[lu^2 \right]$ and droplet radius $R = 15\left[lu \right]$, and it was used to simulate the movement of four droplets placed on the upper and lower surfaces with three different static temperatures. The second configuration flow was subjected to a source term $\phi_i(x) = \frac{\Delta p}{\ell} = 0.000002$ and the third configuration to a source $\phi_i(x) = \frac{\Delta p}{\ell} = 0.000001$. This was to induce constant pressure gradient, which when associated with a second-order bounce back on the top and bottom surfaces resulted in a parabolic flow profile. Periodic boundary condition was imposed on the inlet and outlet boundaries.

Dimensionless variables were used in the analysis of the simulation results with reference time calculated as follows: $\dot{\gamma}_{1/4(h)} \times t$ where $\dot{\gamma}$ is the shear strain rate calculated at $\frac{h}{4}$ and h is the channel height and *t* is the time step. The height of the channel was used as the reference distance, and the central velocity of the undisturbed parabolic flow was used as the reference velocity, which is calculated by $u_{\max} = \frac{h^2}{2\mu} \times \frac{\Delta p}{\ell}$. The calculated physical Eötvös number calculated at $T_{av} = 40c^o$ is

equal to 1.475×10^{-4}. Gravitational acceleration $g = 5.46\times10^{-9}\left[lu\times ts^{-2}\right]$ and mixture interfacial tension $\sigma_0 = 0.01028\left[lf\times lu^{-1}\right]$ were used to ensure Eötvös number similarity.

5.2.1 Validating the Temperature Dependent Static Contact Angle

The first 2D configuration subjected without any source term was used to check the values of the dependency of the contact angles on the domains temperature. The first case was done by assuming a reference contact angle of $\theta = 66.7^o$ at $T = 20^oC$. Several temperatures were assumed, and the corresponding values of the static contact angles were measured directly from the simulations. The model was set to give the required theoretical contact angle calculated by Eq. (5.4) through changing the value of phase field assigned to the wall nodes by Eq. (4.7) which mentioned in the previous chapter.

The measurement results were then compared with the data from the mathematical calculations. Furthermore, the second set of simulations was done by assuming a reference contact angle of $\theta = 45^o$ at $T = 20^0C$ and the same procedure was adopted to check the model robustness.

A trend of diminishing static contact angle is associated with the increase in temperature of the fluid for both reference angles. The results for $\theta = 66.7^o$ and $\theta = 45^o$ were fitted and the following regression formulae were found to describe their behavior:

$$\theta = -0.1052Exp(0.06148T) + 68.1Exp(-0.002053T)$$

$$\theta = -0.01325T^2 + 0.2065T + 45.84$$

Tables 5.2 and 5.3 show the values of the calculated and the measured contact angles for both validation cases.The static contact angle dependency on temperature results are presented in Fig 5.1 The contact angles directly measured from the simulations match very well the calculated angles for the range of temperatures and the two-different reference static contact angles.

Table 5.2: Values of calculated, measured and relative errors for contact angle for validation-1

Temperature(ºC)	Calculated Contact Angle	Measured Contact Angle	Relative Error (%)
20	66.7	65	2.54
40	62.2	61.5	1.12
60	55.3	56	1.26
80	43.1	43.4	0.69

Table 5.3 Values of calculated, measured and relative errors for contact angle for validation-2

Temperature(ºC)	Calculated Contact Angle	Measured Contact Angle	Relative Error (%)
20	45	44.7	0.70
30	40	40	0.11
40	33.4	33	1.21
50	23.4	23	1.67

5.2.2 Simulating the Behavior of One and Two Slugs in Parabolic Flow at Different Temperatures

The domain consisting of $140 \times 20 \left[lu^2 \right]$ was used in this simulation with attached one and two slugs to the top and bottom walls. Three different temperatures were used in the presented simulations. As shown in Fig 5.2, with

$T = 40^{o}C$, the applied source term was able to move the slug. At fluid and wall temperature $T = 50^{o}C$ the slug moved faster from that at the previous temperature and at $T = 60^{o}C$, the same source term was sufficient for moving the slug from its original position towards the end of the domain associated with the fastest quicker than the previous two. This was due to the reduced interfacial tension as a function of temperature, which allowed less energy dissipation into deforming the droplet.

Furthermore, the reduced viscosity effects upon the rise in temperature, which resulted in higher average velocity of the flow, enhanced flow transport capabilities by imparting higher flow momentum on the slug. It is important to mention that the increased adhesion force with the temperature between the slug and the walls affects the average flow velocity; however, this effect is marginalized by the higher flow momentum due to the diminishing viscosity with temperature while exhibiting a small difference in the density of the fluid.

The flow average velocity profile shown in Fig 5.2 indicates the presence of fluctuations resembling a shortwave and the slug moves like a caterpillar. It is clear from the velocity profile that the slug movement is due to a periodic detachment of one end after another. The dip in the average velocity shown in Fig 5.2 is due to that a portion of the flow energy is absorbed in the slug interface, which eventually is released back, when an additional energy buildup from the flow subjected to constant source term, overcomes the adhesion force of the slug at one of its ends.

Referring to Fig 5.3, the same source term is used to push two slugs between two plates at different temperatures. At $T = 40^{o}C$ the applied source term

failed to move the slug due to the high interfacial tension, which allows the slugs to dissipate a larger portion of the flow energy and transforms it into minimal deformation. Moreover, the higher viscosity of both fluids at the prescribed temperature allows the formation of a thicker boundary layer,

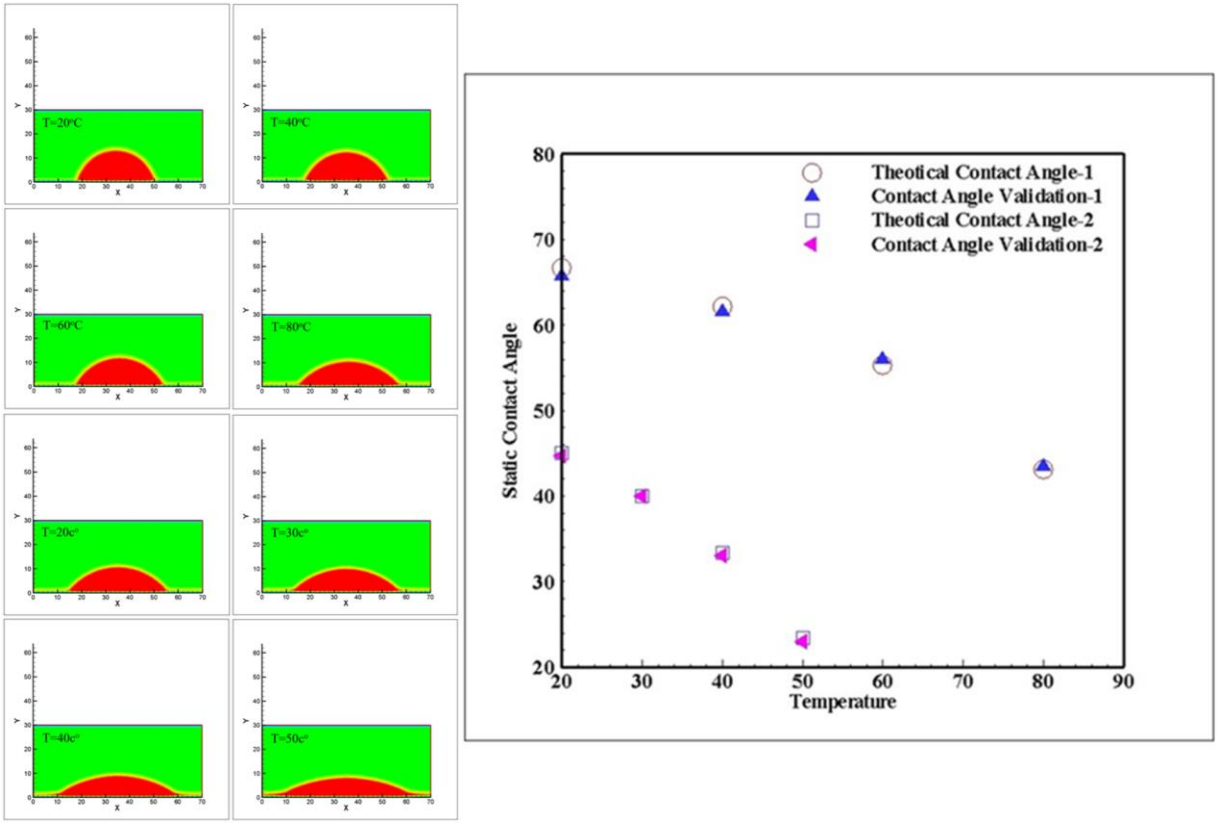

Figure 5.1 Static contact angles at different temperatures for the first and the second validation cases and static contact angle vs. temperature.

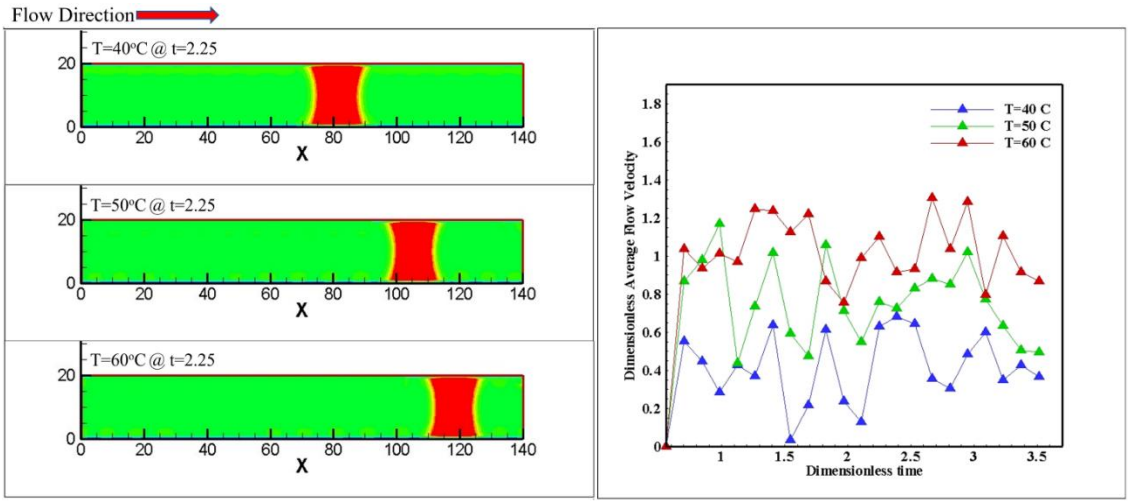

Figure 5.2 One slug displacement at different temperatures and same dimensionless time.

leading to a lower average velocity of the flow, thus depriving the slug of the required momentum to overcome its higher adhesion force on both walls. When temperature increased to $T = 50^{o}C$ the slugs were able to move due to the reduced interfacial tension as a function of temperature, at $T = 60^{o}C$ the slugs moved faster.

The flow average velocity profile shown in Fig 5.3 indicates the same fluctuation phenomena shown in the flow of one slug case. An interesting thing in the average flow velocity profile in this case that in some points the spontaneous average flow velocity is higher than the spontaneous average flow velocity at the same temperature for the one slug case. This is because the two slugs are moving at that moment and the movement of both slugs supports the average flow velocity.

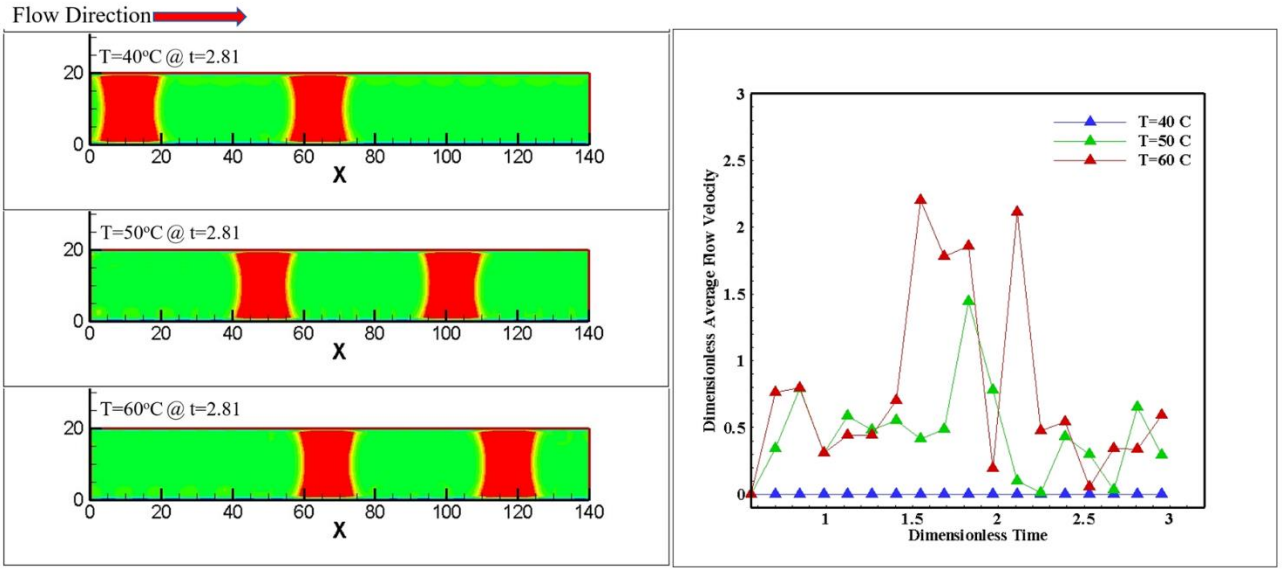

Figure 5.3 Two slugs' displacement at different temperatures and same dimensionless time.

5.2.3 Droplets Flow between Two Parallel Plates at Different Temperatures

The $311\times 49\left[lu^2\right]$ domain containing four droplets with initial radius $R_i=15$ placed on the upper and lower surfaces was used for the dynamic simulation of multi-drops the O/W system. The second configuration source term was used to induce the droplets movement between the two parallel plates at two different temperatures.

The droplets with domains and fluid's temperatures $T=20^oC$ and $T=40^oC$ showed the movement of the droplets because of the smaller adhesion force compared to the slug case. It is obvious from Fig 5.3 that the average flow velocity is almost doubled at higher temperature and that droplets transportation is more efficient for the same reasons mentioned in the previous section. The average flow

velocity for all cases showed much less fluctuation. This is because the droplets are sticking to one side of the domain.

The average contact angle hysteresis for temperatures $T = 20^{o}C$, $T = 40^{o}C$ and $T = 50^{o}C$ was measured as $\Delta\theta = 7.3$, $\Delta\theta = 8.5$ and $\Delta\theta = 10.8$, respectively. The higher contact hysteresis associated with the higher temperature is due to lower droplets' interfacial tension and higher adhesion force.

The streamlines in Fig 5.4 show that the droplets at lower temperature, hence higher viscosity and interfacial tension act like a physical obstacle toward the suspending flow movement.

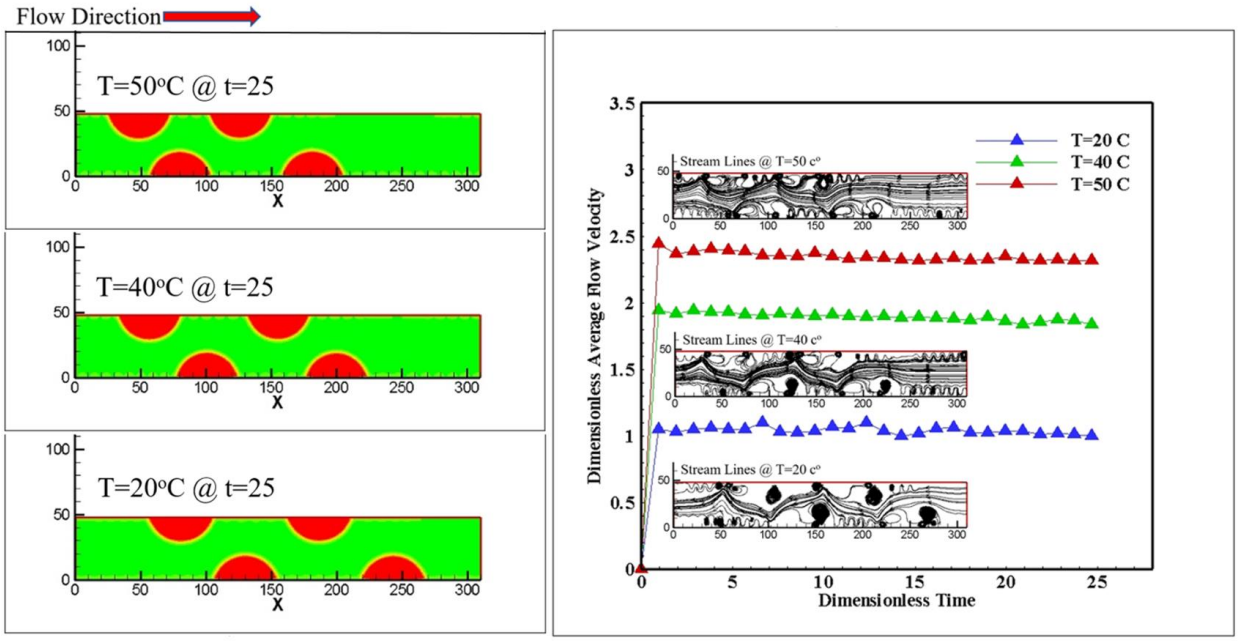

Figure 5.4 Droplets displacement at two different temperatures and same times with negative source term. Insets are for the streamlines of the various cases.

5.2.4 Flow Power Number Ratio

The power contained in the undisturbed flow through the channel is calculated by the following formula (Yagub 2015):

$$Q = \int_{-h}^{h} u dy = \frac{2h^3 \Delta p}{3\mu \ell} = 2u_{ave} h \tag{5.5}$$

where *Q* represents the volumetric flow rate through the channel, $F = \Delta p / \ell$ is the applied source term, u_{ave} is the average undistributed flow velocity and h is half channel height.

The power required for moving the undisturbed flow through the channel is calculated by:

$$\mathrm{P} = Q\ \Delta p = \frac{2h^3 F^2 \ell}{3\mu} = 2u_{ave} h F \ell \tag{5.6}$$

The combined droplets' mass center displacement was tracked in the simulations at equally spaced time steps. The suspended phase velocity was then calculated by numerically differentiating the mass center displacement using second order accuracy finite difference scheme. A droplet power number was derived as follows:

$$\mathrm{P}_d = \frac{\rho_d \cancel{V_d} V_{dmc}^3}{\ell} \tag{5.7}$$

where ρ_d is the droplet density, $\cancel{V_d}$ is the initial combined droplets' volume, V_{dmc} is the combined droplets' mass center terminal velocity and ℓ is the domain length.

The power number here represents the amount of power consumed by the slug/droplets from the flow for them to move; hence, a higher ratio $R_P = \frac{P_d}{P}$ indicates a system that is more efficient. In this case, the flow utilizes more energy into transporting the more important component in the system (oil as the target fluid).

According to Fig 5.5, The power number for one slug case at $T = 40^o C$ is 3.16×10^{-6}, which means that the slug could absorb some of the flow power and used it to move in the domain. At temperature $T = 50^o C$ the power, the number jumped to 1.85×10^{-5} and finally at $T = 60^o C$ the power number increased to 3.12×10^{-5}.

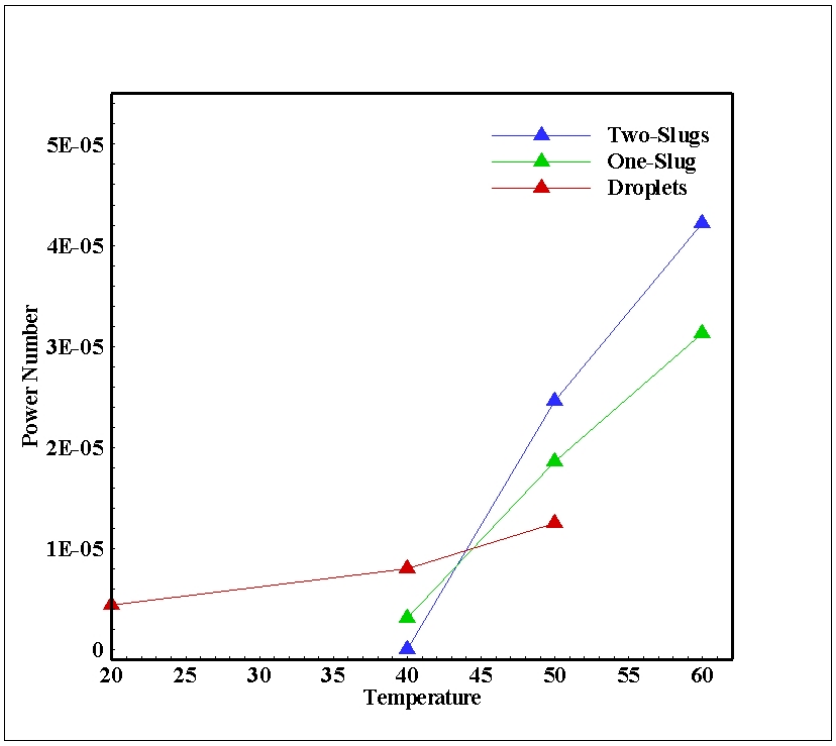

Figure 5.5 Slugs and droplets power number ratios at different temperatures.

For the two-slugs case, the power number at $T = 40^{o}C$ is equal to zero because the slug remained stationary. For $T = 50^{o}C$, the power number jumped to 2.46×10^{-5}, which means that the slug absorbed more energy for the flow and transferred it into useful work to move through the channel. As the temperature increased to $T = 60^{o}C$ the power number increased to 4.12×10^{-5}.

The power number for the droplets at $T = 20^{o}C$ is 4.42×10^{-6}, which means that the droplets could absorb some of the flow power and used it to move in the domain. At temperature $T = 40^{o}C$ the power, the number jumped to 8×10^{-6} due and finally at $T = 50^{o}C$ the power numbers increased to 1.25×10^{-5}.

From Fig 5.5, it is obvious that it is more efficient to transport multi slugs instead of single slug or droplets for this configuration. Another observation is worth mentioning, and it relates to the slopes of the power numbers curves for both cases. The average slope for the one slug, two slugs and droplets are $tan\left(\alpha_{one-slug}\right) = 45.56$, $tan\left(\alpha_{two-slug}\right) = 53.7$ and $tan\left(\alpha_{Droplet}s\right) = 11.88$, respectively. This again stresses the fact that it is more economical to transport multi slugs instead of single slug or multi droplets.

5.3 Confined Flow Simulation and Discussion Without Surfactants

5.3.1 Simulation and Discussion

A (3D) domain representing a flow in a rectangular shaped channel was used in the subsequent simulations. Three configurations were executed. The first consisted of $45\times45\times23\left[lu^{3}\right]$ the domain and a central droplet radius $R = 8\left[lu\right]$ m

deposited on the lower surface. The objective was to investigate the conformance of the temperature dependent static contact angle to the theoretical calculation results.

A second configuration consisting of $65\times34\times22\left[lu^3\right]$ was utilized to simulate the flow of an oil slug attached to the top and bottom surfaces at different static temperatures.

The last configuration consisted of $165\times44\times35\left[lu^3\right]$ and droplet radius $R=11\left[lu\right]$, and it was used to simulate the movement of three droplets placed on the upper and lower surfaces with three different static temperatures. The second configuration flow was subjected to a source term $\phi_i(x)=\frac{\Delta p}{\ell}=9\times10^{-7}$ and the third configuration to a source $\phi_i(x)=\frac{\Delta p}{\ell}=2.5\times10^{-6}$. This was to induce constant pressure gradient, which when associated with a second-order bounce back on the top and bottom surfaces resulted in a parabolic flow profile. Periodic boundary condition was imposed on the inlet and outlet boundaries. Dimensionless variables were used in the analysis of the simulation results with reference time calculated as follows: $\dot{\gamma}_{1/4(h)}\times t$ where $\dot{\gamma}$ is the shear strain rate calculated at $\frac{h}{4}$ and h is the channel height and *t* is the time step. The height of the channel was used as the reference distance, and the central velocity of the undisturbed parabolic flow was used as the reference velocity, which is calculated by: $u_{\max}=\frac{h^2}{2\mu}\times\frac{\Delta p}{\ell}$

The lattice surface tensions for the two fluids were set such that a mixture interfacial tension of $\sigma_0 = 0.0199 \left[lf \times lu^{-1} \right]$. The calculated physical Eötvös number calculated at $T_{av} = 40^o C$ is equal to 1.475×10^{-4}. Gravitational acceleration $g = 5.46 \times 10^{-9} \left[lu \times ts^{-2} \right]$ and mixture interfacial tension $\sigma_0 = 0.01028 \left[lf \times lu^{-1} \right]$ were used to ensure Eötvös number similarity.

5.3.2 Validating Temperature Dependent Static Contact Angle

The first 3D configuration $45 \times 45 \times 23 \left[lu^3 \right]$ subjected without any source term was used to check the values of the dependency of the contact angles on the domains temperature. The first case was done by assuming a reference contact angle of $\theta = 66.7^o$ at $T = 20^o C$. Several temperatures were assumed, and the corresponding values of the static contact angles were measured directly from the simulations.

The measurement results were then compared with the data from the mathematical calculations. Furthermore, the second set of simulations was done by assuming a reference contact angle of $\theta = 50^o$ at $T = 20^o C$ and the same procedure was adopted to check the model robustness.

A trend of diminishing static contact angle is associated with the increase in temperature of the fluid for both reference angles. The results for $\theta = 66.7^o$ and $\theta = 50^o$ were fitted and the following regression formulae were found to describe their behavior:

$$\theta = -0.1052Exp(0.06148T) + 68.1Exp(-0.002053T)$$

$$\theta = -0.00775T^2 - 0.0045T + 53.1$$

Tables 5.4 and 5.5 show the values of the calculated and the measured contact angles for both validation cases.The static contact angle dependency on temperature results are presented in Fig 5.6 The contact angles directly measured from the simulations match very well the calculated angles for the range of temperatures and the two-different reference static contact angles.

Table 5.4: Values of calculated, measured and relative errors for contact angle for validation-1

Temperature($C^{o)}$	Calculated Contact Angle	Measured Contact Angle	Relative Error (%)
20	66.7	66	1.05
40	62.2	62	0.32
60	55.3	56	0.54
80	43.1	44	2.08

Table 5.5: Values of calculated, measured and relative errors for contact angle for validation-2

Temperature($C^{o)}$	Calculated Contact Angle	Measured Contact Angle	Relative Error (%)
20	50.03	50	0.06
30	45.9	45.7	0.43
40	40.66	40.8	0.34
50	33.49	33.4	0.27

5.3.3 Simulating the Behavior of A slug in Parabolic Flow at Different Temperatures

The domain consisting of $65 \times 34 \times 22 \left[lu^3 \right]$ was used in this simulation with an attached slug to the top and bottom walls placed in the center of the channel. Three different temperatures were used in the presented simulations.

As shown in Fig 5.7, with $T = 20^{o}C$, the applied source term failed to move the slug due to the high interfacial tension, which allows the slug to dissipate a larger portion of the flow energy and transforms it into minimal deformation. On the other hand, the higher viscosity of both fluids at the prescribed temperature allows

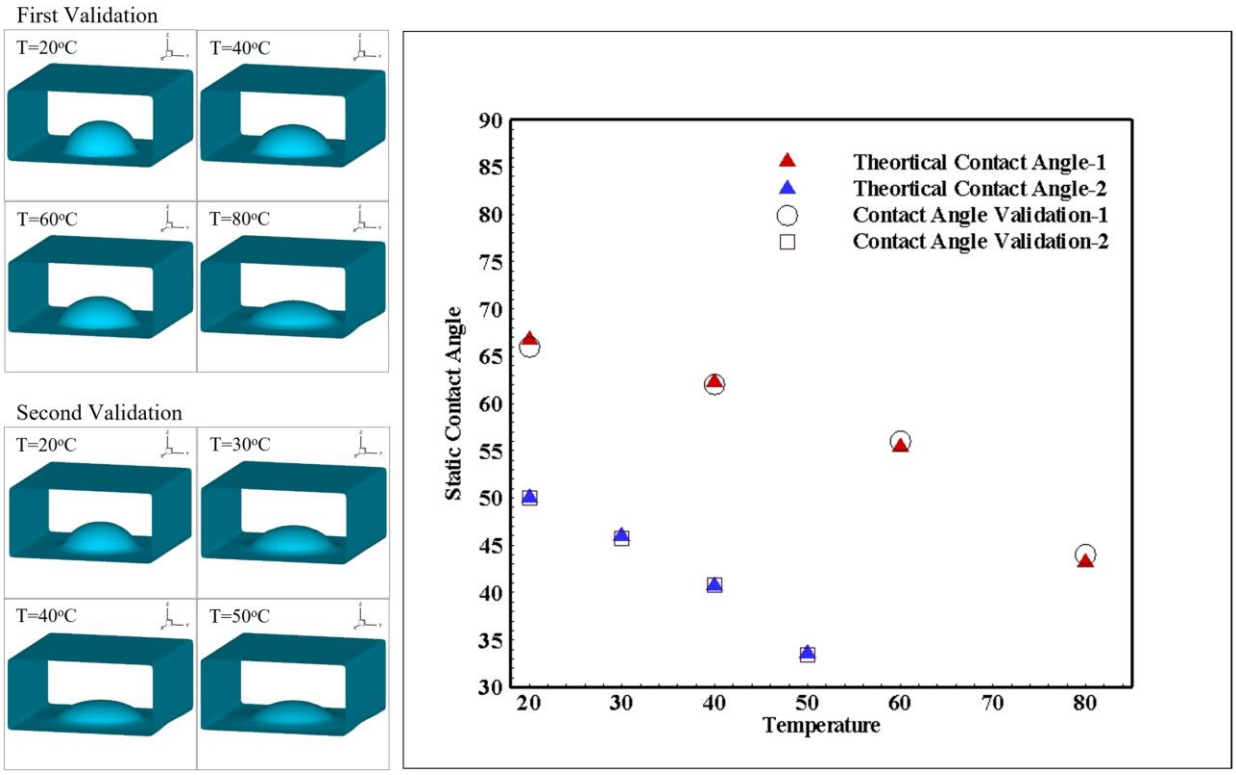

Figure 5.6 Static contact angles at different temperatures for the first and the second validation cases and static contact angle vs. temperature.

the formation of a thicker boundary layer, leading to a lower average velocity of the flow, thus depriving the slug of the necessary momentum to overcome its higher adhesion force on both walls. At fluid and wall temperature $T = 40^{o}C$, $T = 60^{o}C$ and $T = 80^{o}C$, the same source term was sufficient for moving the slug from its original position towards the end of the domain. This was due to the

reduced interfacial tension as a function of temperature, which allowed less energy dissipation into deforming the droplet.

Furthermore, the reduced viscosity effects upon the rise in temperature, which resulted in a higher average velocity of the flow, enhanced flow transport capabilities by imparting higher flow momentum on the slug. It is important to mention that the increased adhesion force with the temperature between the slug and the walls affects the average flow velocity; however, this effect is marginalized by the higher flow momentum due to the diminishing viscosity with temperature while exhibiting a small difference in the density of the fluids.

For temperatures, $T \geq 40^{o}C$ the slug moves forward in the domain. The flow average velocity profile shown in Fig 5.7 indicates the presence of fluctuations resembling a shortwave and the slug moves like a caterpillar.

It is evident from the velocity profile that the slug movement is due to a periodic detachment of one end after another. The dip in the average velocity shown in Fig 5.7 is due to that a portion of the flow energy is absorbed in the slug interface, which eventually is released back, when an additional energy buildup from the flow subjected to constant source term, overcomes the adhesion force of the slug at one of its ends.

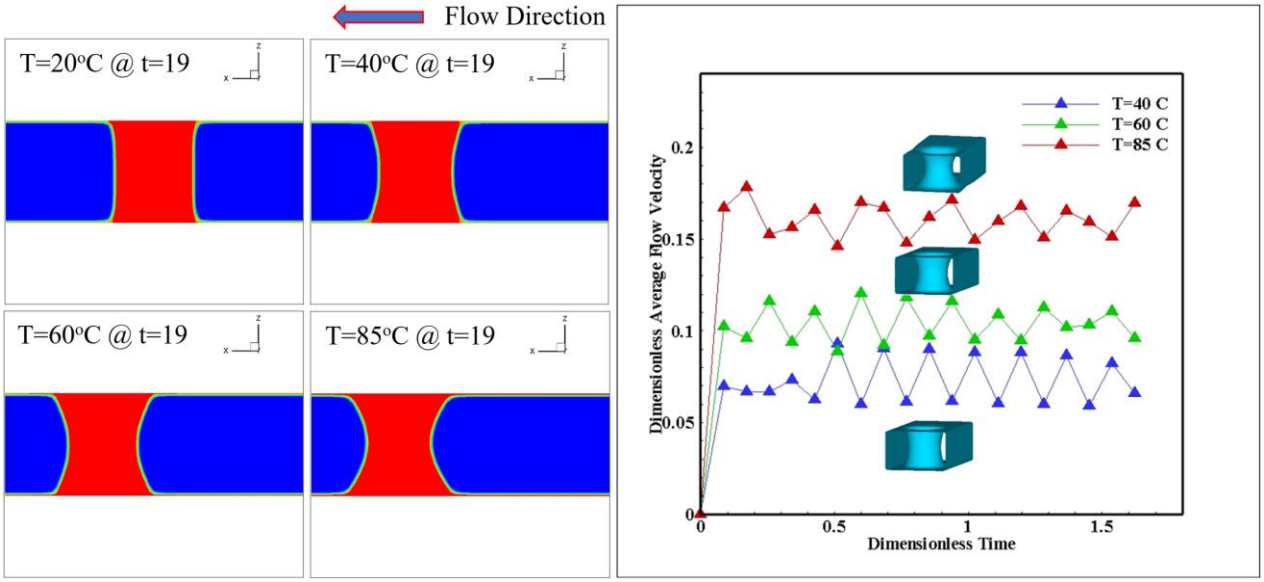

Figure 5.7 Slugs displacement at different temperatures and same dimensionless time.

5.3.4 Droplets in Flow in Parabolic Flow at Different Temperatures

The $165\times44\times35\left[lu^3\right]$ domain containing two droplets with an initial radius $R_i=11$ placed on the upper and lower surfaces was used for the dynamic simulation of multi-drops the O/W system. The second configuration source term which it $\phi_i(x)=\frac{\Delta p}{\ell}=2.5\times10^{-6}$ was used to induce the droplet movement in the channel at three different temperatures.

The droplets with domains and fluid's temperatures $T=20^oC$, $T=45^oC$ and $T=70^oC$, showed the movement of the droplets because of the smaller adhesion force compared to the slug case and the higher applied source term. It is obvious from Fig 5.8 that the average flow velocity is about 2.7 times as $T=70^oC$ compared to that at $T=20^oC$. The average flow velocity for all cases showed no fluctuation.

This is because the droplets are sticking to one side of the domain and the source term used for the droplets is higher.

The average contact angle hysteresis for temperatures $T = 20^{o}C$, $T = 45^{o}C$ and $T = 70^{o}C$ was measured as $\Delta\theta = 2.46$, $\Delta\theta = 4.91$ and $\Delta\theta = 6.3$, respectively. The higher contact hysteresis associated with, the higher temperature is due to lower droplets' interfacial tension and higher adhesion force. The x-velocity in Fig 5.8 show that the droplets at lower temperature, hence higher viscosity and interfacial tension act like a physical obstacle toward the suspending flow movement.

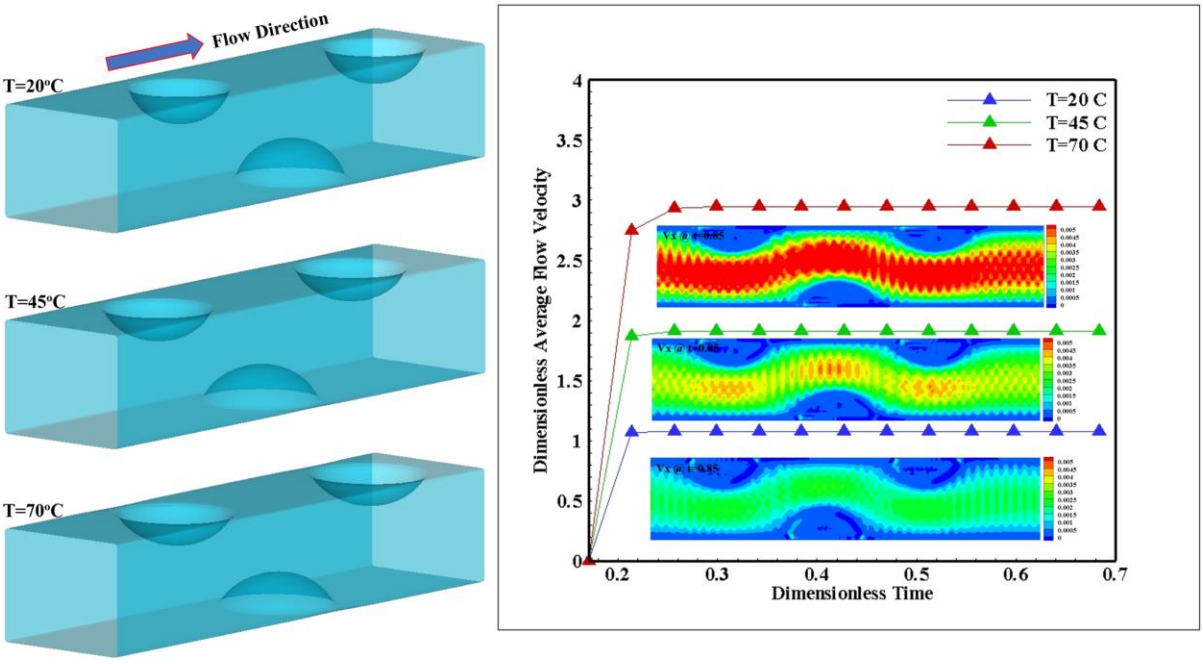

Figure 5.8 Droplets displacement at three different temperatures and same times with negative, positive term. Insets are for the x-velocity of the various cases.

5.3.5 Flow Power Number Ratio

In this case, the flow utilizes more energy. According to Fig 5.9, the slug, the power number at $T = 40^{o}C$ is equal to 4.96×10^{-9}. For $T = 60^{o}C$, the power number jumped to 6.1×10^{-9}, which means that the power absorbed by the slug is increased and transferred it into useful work to move through the channel. As the temperature increased to $T = 85^{o}C$ the power number increased to 9.37×10^{-9}.

For the case of the droplets, From Eq. (5.6). The flow power is inversely proportional to the dynamic viscosity, which is temperature dependent.

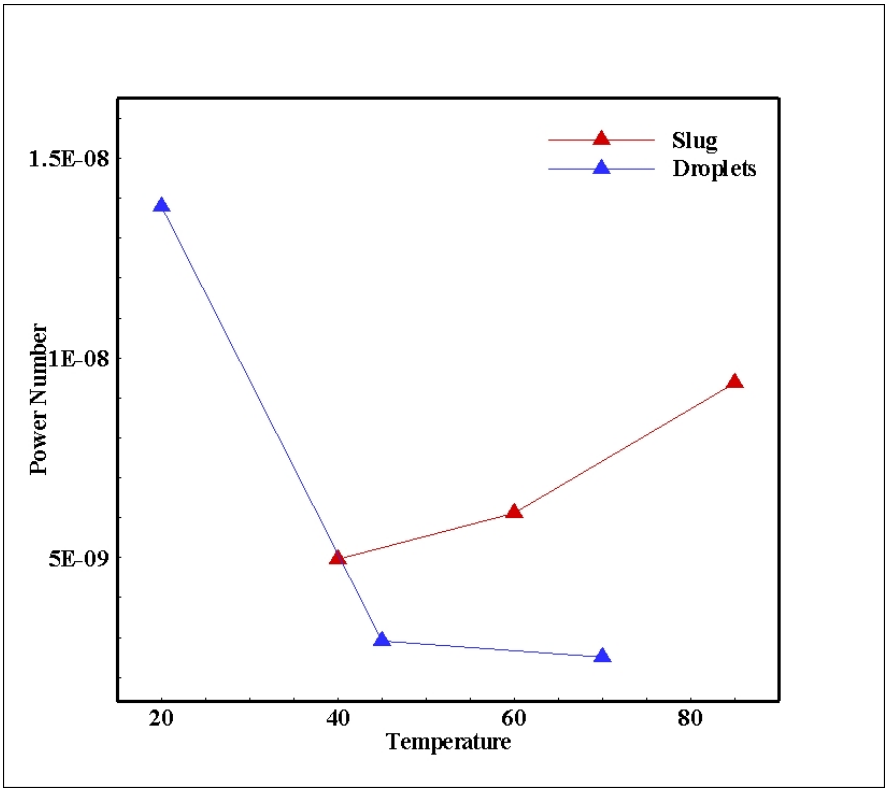

Figure 5.9 Slug and droplets power number ratio at using the average slug and droplets velocity at different temperatures.

Eq. (5.7) Shows that the power number is directly proportional to the suspended fluid density and the droplets velocity raised to power three. Logically any increase in the fluid temperature at constant pressure drop and droplet radius leads to an increase in the flow power due to the reduction of the dynamic viscosity of the suspending fluid. While the increase in temperature leads to higher suspended fluid velocity and lower density.

The value of the contact angle which affects the attached droplet height and contact surface area between the droplet and the wall is an additional temperature dependent parameter which affects droplet power number too. If temperature increases, contact angle reduces, droplet height shrinks and the contact surface between wall and droplet increases. As a result, the droplet will lose some of its momentum because its top will be farther from the channel centerline and has more area attached to the wall which increases adhering force and makes the droplet cling more and vice versa. All these competing factors determine the outcome of the power number ratio.

The power number ratio and the contact angle for the droplets at $T = 20^{o}C$ are 1.38×10^{-8} and 66.7^{o} respectively, which means that the droplets could absorb power from the flow and use it to move in the domain. At temperature $T = 45^{o}C$ the power number ratio and contact angle reduced to 2.89×10^{-9} and 60.7^{o} respectively. Firstly, the temperature increased and made the viscosity five times smaller than the viscosity $T = 20^{o}C$ and increased the required flow power is higher by five times. Secondly, the contact angle is smaller and made droplets height shrink

about 16.7 % compared to the droplet height at $T = 20^{o}C$ which reduced the momentum transfer to them.

On the other hand, the contact area between droplets and the wall increased about 1.23 times, and this augmented the adhering force between droplets and wall and supported the losses in droplets power and made the droplets move slower. For the density at the current temperature is almost the same compared to the previous case.

Good to mention that as the temperature increases, the droplets will be softer and easier to deform due to the reduction in the interfacial tension which leads to making the droplet softer and loss part of the absorbed power from the flow on this deformation. As a result, droplet power number is smaller, and the required flow power is higher this makes the power ratio at the current temperature is smaller compared to that at $T = 20^{o}C$.

For $T = 70^{o}C$ the power number ratio is, 2.49×10^{-9} and the contact angle is 50.2º. The viscosity here is about 15.9 times smaller than it at $T = 20^{o}C$, this made the required flow power is the highest compared to the previous two cases. Currently, the contact angle is the smallest which reflects higher contact area by about 1.37 times that at $T = 20^{o}C$ and shrank in droplet height about 21.8% compared to the droplet height at $T = 20^{o}C$, these supported the reduction in momentum received by the droplets due to the farthest distance between the droplets top and the centerline of the channel and the higher adhering force which came from, the higher contact area between droplets and the wall. The density at

the current temperature is about 4% smaller than the density at $T = 20^{o}C$, this means that the density role on the droplets power number is very minimal compared to the other parameters and can be neglected. As a result, the droplets the power number ratio for the current case is the smallest.

From Fig 5.9, it is obvious that it is more efficient to transport slugs instead of droplets for this configuration, another observation is worth mentioning, and it relates to the slopes of the power numbers curves for both cases. The slug curve's slope is steeper at, $T = 85^{o}C$ and it diminishes at a lower temperature, contrary to the droplets curve's slope, which behaves in an opposing manner. The average slope for the slug and droplets is $tan\left(\alpha_{slug}\right) = 22.96$ and $tan\left(\alpha_{droplets}\right) = -34.42$, respectively.

CHAPTER 6 INVESTING THE EFFECTS OF THERMAL, SURFACTANTS AND SURFACE ENERGY ON THE FLOW CHARACTERISTICS OF OTL IN WATER MIXTURE BETWEEN TWO PARALLEL PLATES

A hybrid quasi-steady thermal lattice Boltzmann model with a temperature and surfactants dependent contact angle is presented here. The model was used to study the combined effects of temperature, surfactants and contact angle on the movement of slugs and droplets of oil in water (O/W) system flowing between two parallel plates.

The model was used to simulate the dynamic behavior of droplet and slug deposited on the domain's upper and lower surfaces, while subjected to parabolic flow conditions.

The model accurately simulated the contact angle hysteresis for the dynamic droplets cases. It was also shown that by adding surfactants at elevated temperatures, the power to transport the mixture diminished remarkably. The goal is to improve our understanding of the underlying physics associated with the secondary and tertiary extraction process of trapped crude oil in wells by injecting hot water with the presence of the surfactants.

6.1 Simulation and Discussion

A two-dimensional (2D) domain consisted of $220 \times 38 \left[lu^2 \right]$ at $T = 60^o C$ representing a flow between two plates was used in the subsequent simulations. A central droplet with radius $R = 17 \left[lu \right]$ was deposited on the lower surface to study the effects of surfactants concentration on the movement of one droplet. Same configuration and temperature were used to simulate the flow of one trapped

slug between two plates attached to the upper and lower walls with an initial height $H_D = 38\left[lu \right]$ with and without surfactants. The flow was subjected to a source term $\phi_i(x) = \frac{\Delta p}{\ell} = 0.00000135$ to induce a constant pressure gradient, which when associated with a second-order bounce back on the top and bottom surfaces resulted in a parabolic flow profile. Periodic boundary condition was imposed on the inlet and outlet boundaries.

Dimensionless variables were used in the analysis of the simulation results with reference time calculated as follows: $\dot{\gamma}_{1/4(h)} \times t$ where $\dot{\gamma}$ is the shear strain rate calculated at $\frac{h}{4}$, where h is the channel height and *t* is the lattice time step. The height of the channel was used as the reference distance, and the central velocity of the undisturbed parabolic flow was used as the reference velocity, which is calculated by: $u_{\max} = \frac{h^2}{2\mu} \times \frac{\Delta p}{\ell}$ The calculated physical Eötvös number calculated at $T_{av} = 60^o C$ is equal to 3.6107×10^{-5}. Gravitational acceleration $g = 5.46 \times 10^{-9} \left[lu \times ts^{-2} \right]$ and mixture interfacial tension $\sigma_0 = 0.0163\left[lf \times lu^{-1} \right]$ were used to ensure Eötvös number similarity.

6.2 Simulating the Behavior of Droplet Flow in Parabolic Flow with and Without Surfactants

Temperature $T = 60^o C$ was used in the following simulation. As shown in Fig 6.1A for the applied source term the droplet, was able to move, and later the droplet

started to break up due to the presence of the surfactants on the droplet interface, which reduces the interfacial tension and makes the droplet more compliant. The deformation of the droplet forces it extend toward the center of the domain, which is subjected to higher flow momentum and eventually created a velocity gradient between the lower and upper parts, leading to its breakup. After droplet breakup, the daughter droplets are detached from the wall and can move with less restriction.

Fig 6.1B shows droplet without surfactants, which is subjected to the same source term and temperature. The droplet was able to move, but without any breakup due to the high interfacial tension, the traveled distance by the droplet is less compared to the previous case.

The flow average velocity profile shown in Fig 6.2 indicates the velocity associated with the surfactants contaminated droplet is higher and shows some reduction in magnitude beyond dimensionless time t = 2.5. This is because of the droplet breakup and reduction in the momentum of the daughter droplets due to the reduction in their mass.

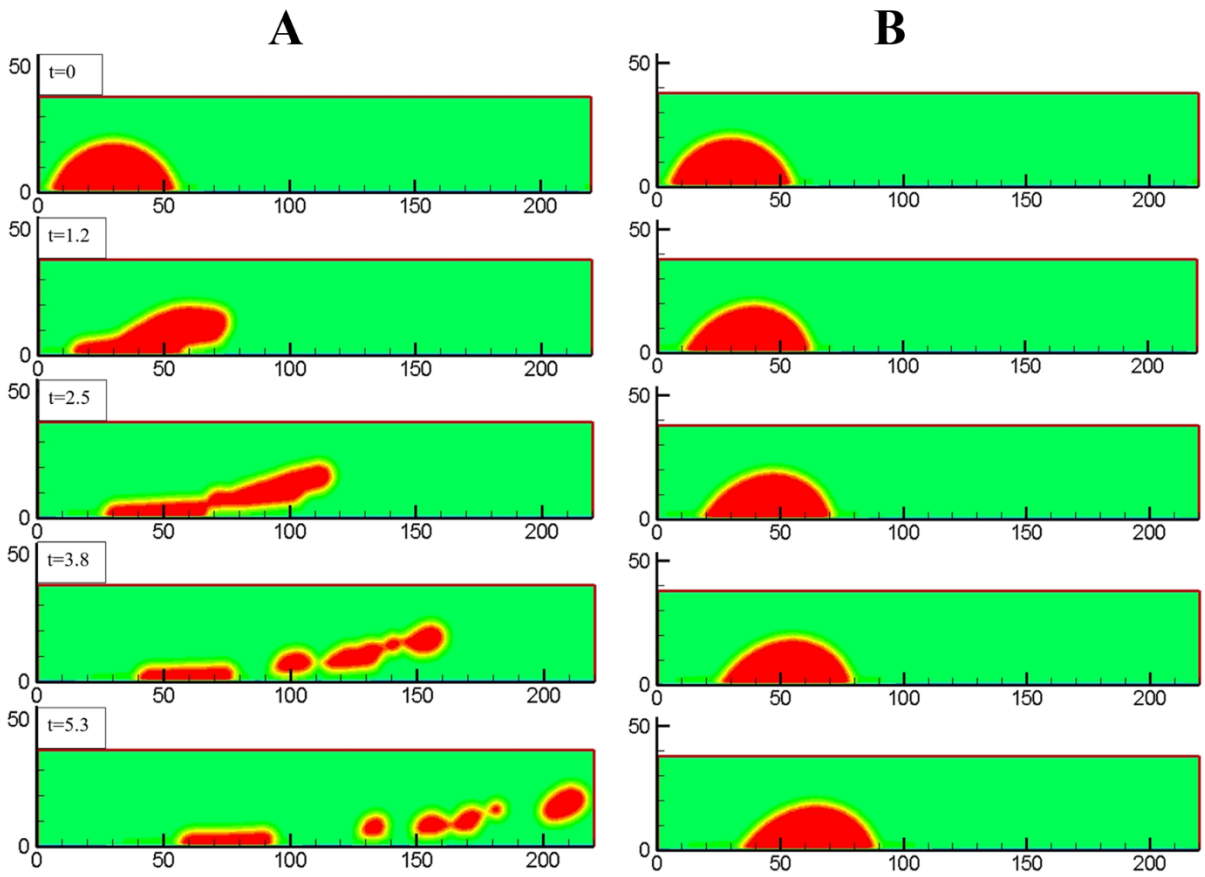

Figure 6.1 Droplet displacement at different dimensionless time steps (A) With surfactants (B) without surfactants.

On the other hand, the droplet without surfactants shows a steady increment in the average flow velocity. However, this velocity is lower than the surfactants covered droplet's case due to the high losses which came from the adhesion force between the droplet and the wall.

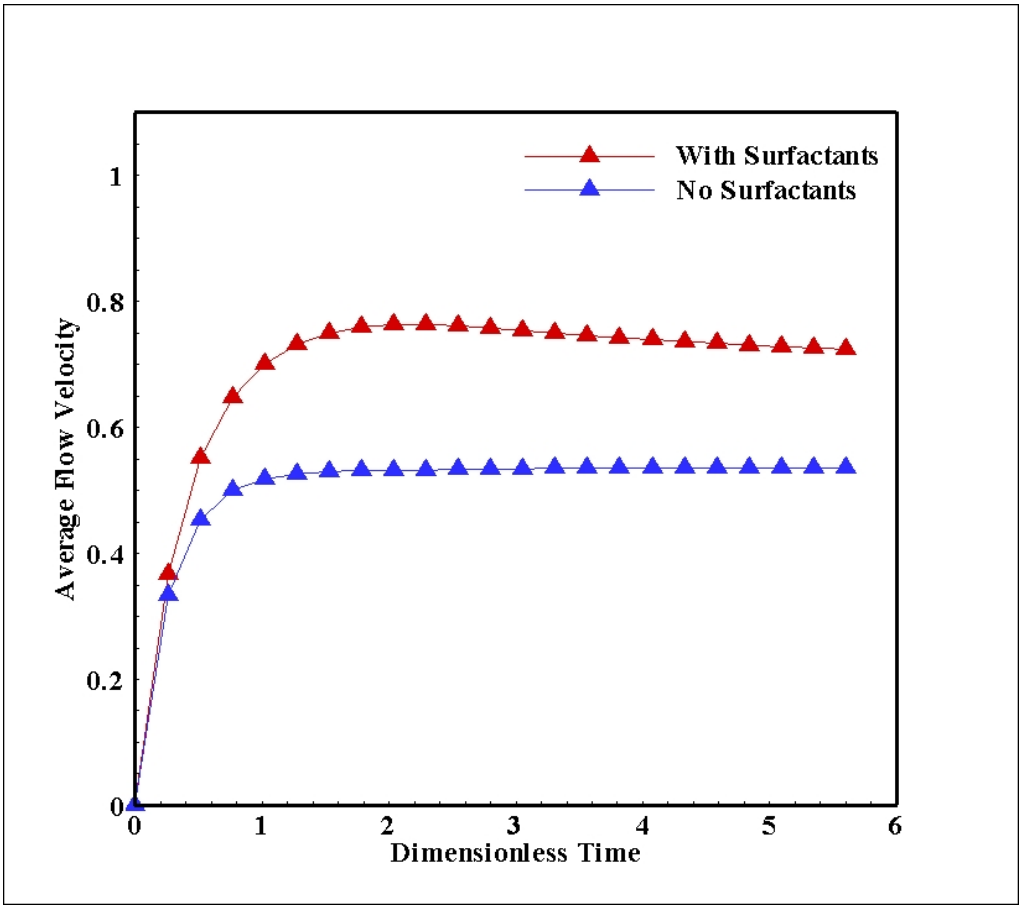

Figure 6.2 Dimensionless average flow velocity of the red dropletwith and without surfactants at different dimensionless time steps.

6.3 Simulating the Behavior of Slug Flow in Parabolic Flow with and Without Surfactants

In Fig 6.3, the same source term was used to move a slug between two plates at temperature $T = 60^{o}C$.

The slug with surfactants was able to move, then it experienced deformation due to the additional reduction in the interfacial tension by surfactants. The deformation

of the droplet leading to its breakup into multiple daughter droplets. These droplets are liberated from the wall, and they can be moving freely between the two walls.

On the other hand, the slug without surfactants, most of the flow momentum is dissipated into deformation. The rest of the flow momentum was.

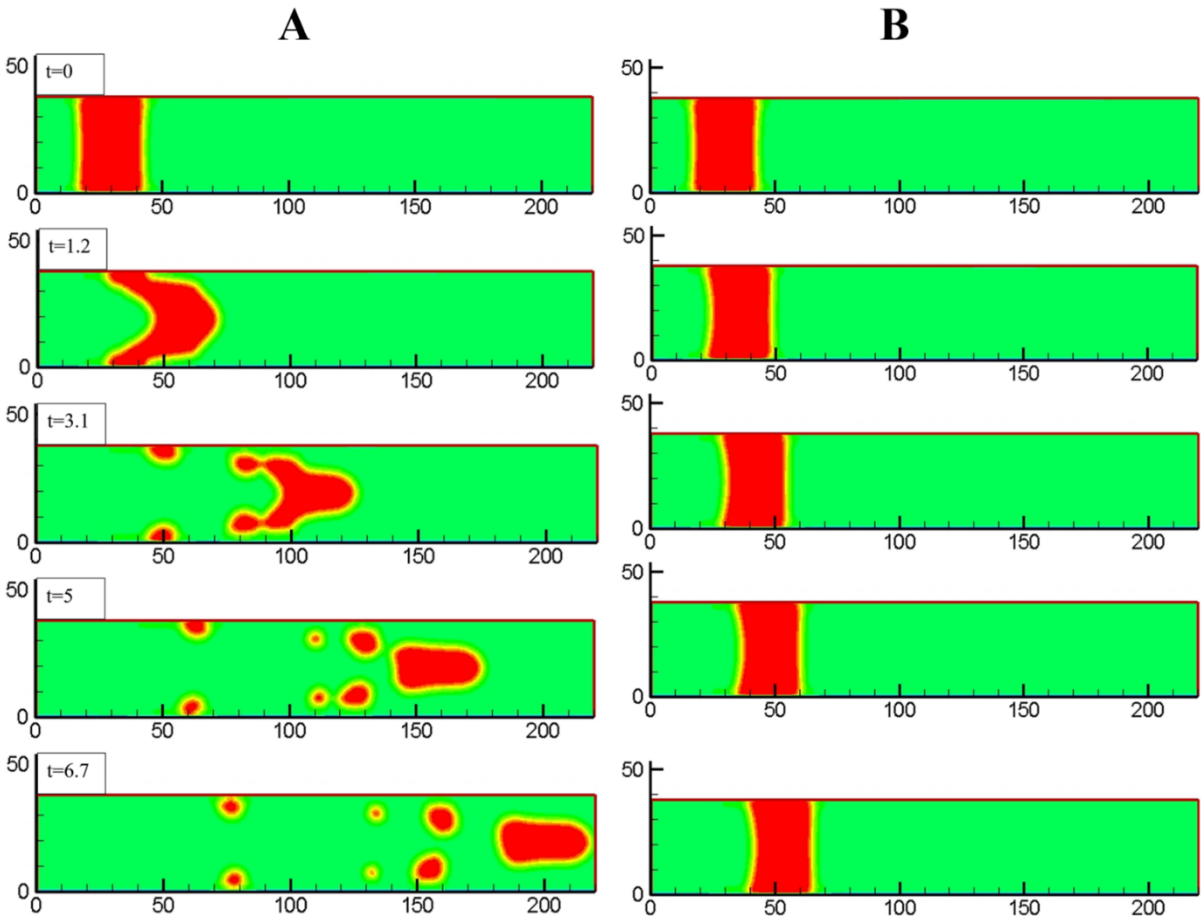

Figure 6.3 Slug displacement at different dimensionless timesteps (A) With surfactants (B) without surfactants.

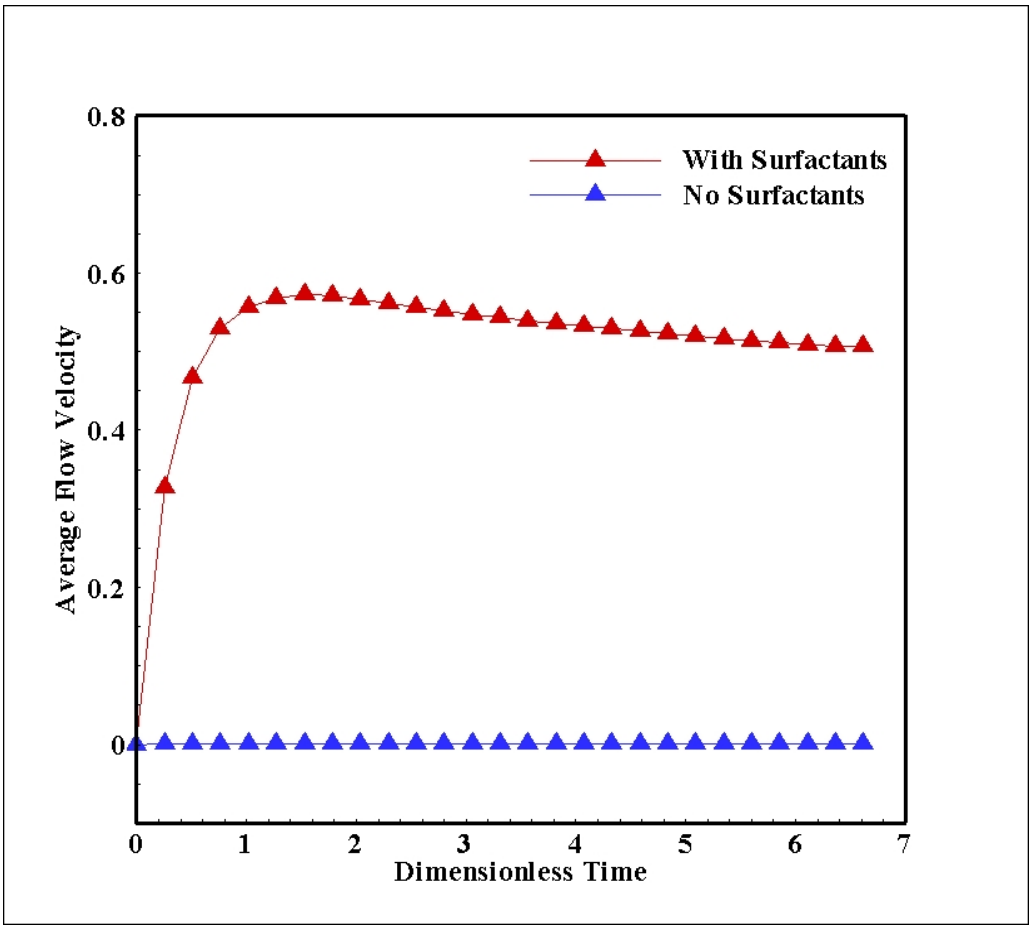

Figure 6.4 Dimensionless average flow velocity of slug with and without surfactants at different dimensionless time steps.

spent on moving the slug between the two walls but at a low velocity due to the adhesion force.

The flow average velocity profile shown in Fig 6.4 indicates the velocity associated with the surfactants contaminated slug is much higher than that of the case without surfactants. The figure also shows some reduction in the average flow velocity magnitude of the surfactants case beyond dimensionless time=2.5 because the slug breakup unleashes the stored energy from the flow into the

deformed interface back into the flow. Further breakups produce smaller daughter-droplets and eventually the flow gets to its steady state.

6.4 Surfactants Distribution for the Droplet and the Slug Flow

As shown in Fig 6.5**,** the distribution of surfactants for the droplet case at dimensionless time step = 1.2, reveals an accumulation of surfactants at the rear region without much accumulated surfactants at the frontal region of the droplet. This is due to the nature of the suspended fluid flow around the interface, with the droplets resisting the movement due to a large adhesion force.

At dimensionless time step = 3.1, the surfactants accumulation is present on the front stagnation region. This is due to the fact that the top interface of the droplet is subjected to lower shear stress due to a smaller shearing strain rate. As the droplet moves forward, deformation occurs and interfacial surface increases, which makes the surfactants diminish at the rear lower region because of expansion and due to the shear lift created by the proximity of the interface to the lower wall.

At dimensionless time step = 5, the droplets breaks up, most of the surfactants remain on the main part, and other daughter droplets will get less concentration, As these daughter droplets move between the two walls, they will subject to shear stress on their surface which makes the surfactants accumulate at the regions with less shear.

Finally, at dimensionless time step = 6.7, the separated droplets move towards the middle of the domain, where the shear lift is no more the driving force

and the hydrodynamic characteristics of the flow between two parallel plates is dominant. This moves the surfactants to the frontal section of the interface since the suspending fluid velocity near the droplets interfaces is higher than that of the droplet.

For the slug case, at dimensionless time step = 1.2, an accumulation of surfactants at the rear region and it is seen at the stagnation regions near the upper and lower walls.

At dimensionless time step = 3.1, the slug deforms, and the deformation at the frontal section of the slug's interface is associated with an increase in the interface surface. This drive the surfactants concentration to diminish at that region.

At dimensionless time step = 5, breakup occurs, a large droplets moves centrally with a shoe like shape. The continuous expansion of the droplet leads to decreased concentration at the frontal section. The rear section of the detached droplet still exhibit high concentration at the rear section of the droplet. This leads to further breakup of the slug into multi droplets moving between the two walls without any adhesion.

At dimensionless time step = 6.7, further breakup occurs and this lead to further decrease in their surfactants concentration.

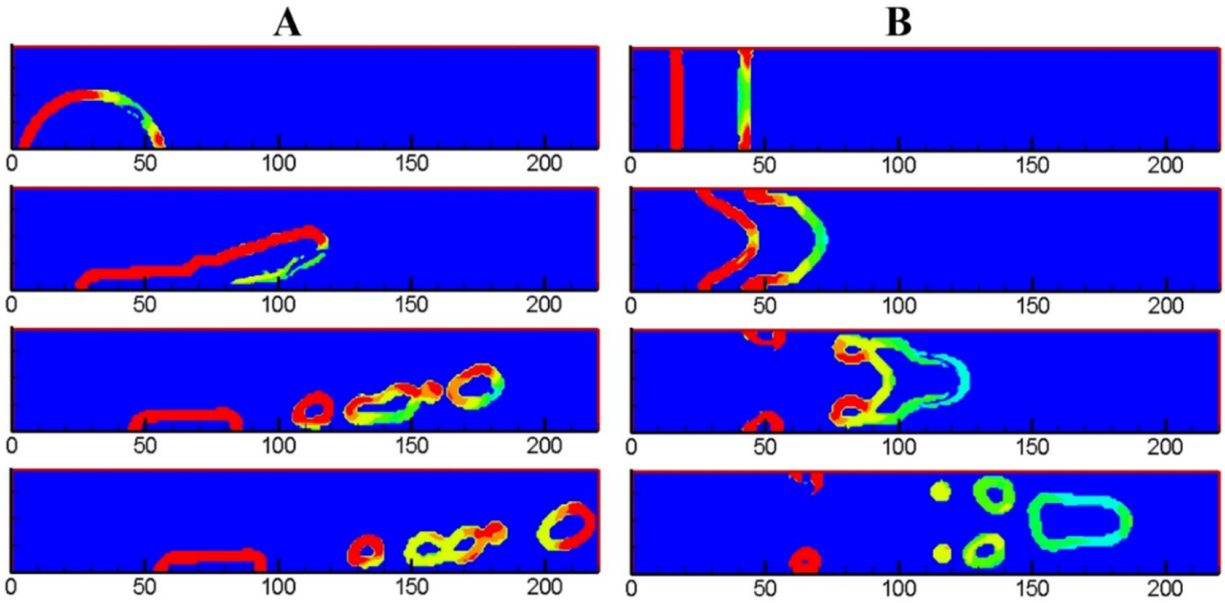

Figure 6.5 Surfactants distribution and verical tangetial velocity at different times (A) surfactant distributionfor the droplet (B) surfactant distribution for the slug.

6.5 Flow Power Number Ratio

The power required for moving the undisturbed flow through the channel is calculated by:

$$\mathrm{P} = Q\,\Delta p = \frac{2h^3F^2\ell}{3\mu} = 2u_{ave}hF\ell \tag{6.1}$$

The combined droplets' mass center displacement was tracked in the simulations at equally spaced time steps.

The suspended phase velocity was then calculated by numerically differentiating the mass center displacement using second order accuracy finite difference scheme. A droplet power number was derived as follows:

$$\mathrm{P}_d = \frac{\rho_d \forall_d V_{dmc}^3}{\ell} \tag{6.2}$$

where ρ_d is the droplet density, V_d is the initial combined droplets' volume, V_{dmc} is the combined droplets' mass center terminal velocity and ℓ is the domain length.

The power number here represents the amount of power consumed by the slug/droplets from the flow for them to move; hence, a higher ratio $R_P = \frac{P_d}{P}$ indicates a system that is more efficient. In this case, the flow utilizes more energy into transporting the more important component in the system (oil as the target fluid).

As shown in Fig 6.6, the average power number ratio for the droplet with surfactants is about 41 times the one without surfactants. This was due to the significant difference in droplet velocity for the two cases. For the one with surfactants, the droplet broke up into daughter droplets moving inside the channel without facing any curb which comes from adhesion between the droplets and the wall. This made the average droplets velocity about 3.4 times the droplet velocity without surfactants, and this number is raised to the power 3 as per Eq. (6.2). Furthermore, the droplet without surfactants was moving on the lower wall and facing a continuous resistance which dropped the power number for this case.

A distinct issue should be mentioned about the power number ratio for the droplet with surfactants. The ratio undergoes a fluctuation due to the breaking up of the main droplet to different sizes of daughters-droplets.

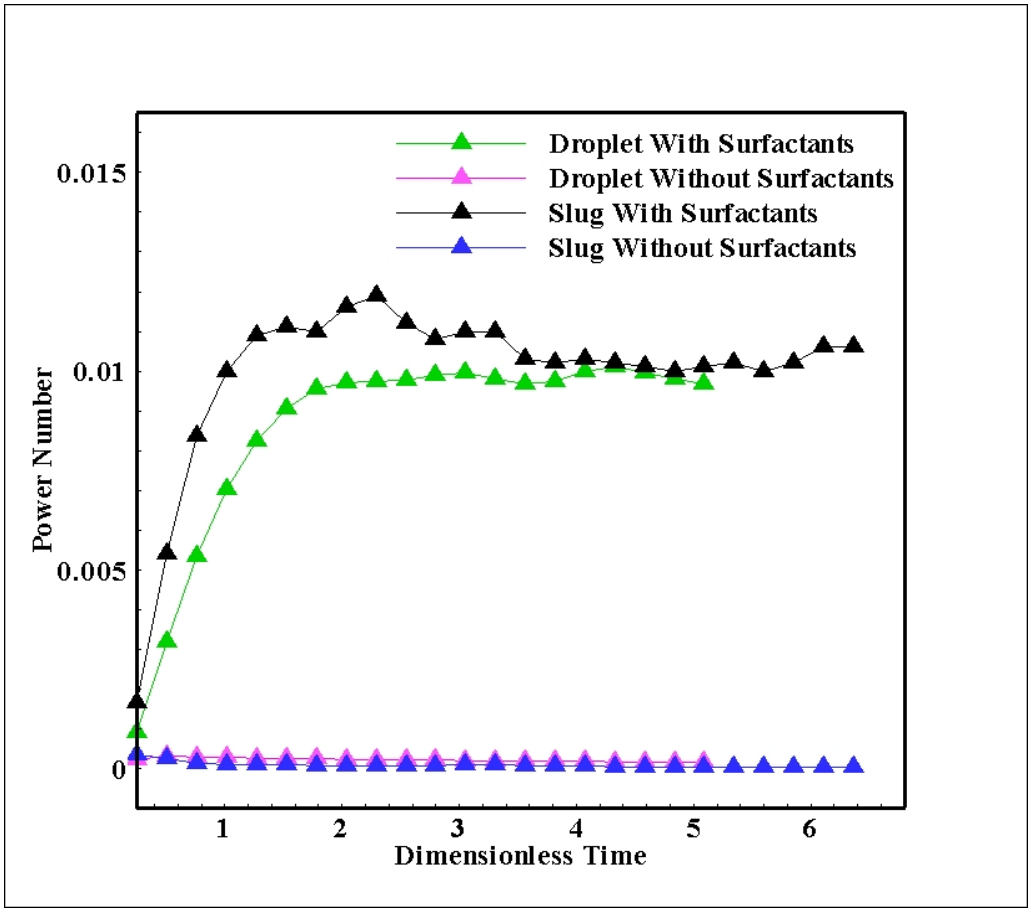

Figure 6.6 Slug and droplet power number ratios at different dimensionless times.

For the slug with surfactants case, the average power number ratio is about 130.5 times than that without surfactants. The power number for the slug with surfactants is even bigger than that for the droplet with surfactants by 1.16 times. This fact comes from the orientation of the slug which blocks all the distance between the two plates and absorbs all the momentum from the flow.

The slug without surfactants is suffering from stiff resistance in the form of adhesion force applied on it from both plates. This leads to an average slug velocity

of about 5.3 times less than the the other slug with surfactants. It is good to mention that the power number ratio for the slug with surfactants undergoes a fluctuation over the time due to the same reason which were stated for the droplet case.

CHAPTER 7 HYBRID THERMAL LATTICE BOLTZMANN MODEL FOR ANALYZING THE TRANSPORTATION OF SURFACTANTS CONTAMINATED EMULSIONS IN PARABOLIC FLOWS

A special LBM model, which couples the effects of hydrodynamics, interfacial physics, surfactants effects, and the temperature is used for the investigation of the flow behavior of O/W emulsions with the goal of delineating the best practices for transporting these emulsions in circular ducts. The effects of temperature, volume fraction, flow pressure gradient, and surfactants concentration are investigated in a Poiseuille flow setup. A dimensionless power number ratio was introduced and successfully used for guiding the selection of the most cost-efficient means for transporting O/W emulsion.

7.1 Simulation Results and Discussion

In this work ts indicates lattice time step, mu lattice mass unit and lu the lattice spatial unit. 3D domain representing cylindrical channel with radius $R_{ch} = 60\ lu$ and length $\ell_{ch} = 350\ lu$ was used for the simulations of droplets transportation in cylindrical micro-channels. An average density ratio of $\frac{\rho_R}{\rho_B} = 0.87$ was set to simulate suspension of transformer oil in the water matrix. *R* and *B* indicate the suspending and suspended fluids, respectively. A relaxation time $\tau = 0.945$ was imposed, which led to a kinematic viscosity $\nu = 0.063 lu^2/ts$ of the suspending fluid.

The surface tension constants for all constituent fluids was set such that the resulting interfacial tension was $\gamma = 0.035$, and the undisturbed droplet radius was

set to $R_i = 25\ lu$ .The gravitational constant was selected as $g = 1.96\times10^{-9}$, which resulted in a Bond number $B = 4\Delta\rho g R^2/\gamma_{LV} = 0.758$. An initial dimensionless surfactants concentration of $\Gamma^* = 0.4$, surfactants elasticity $E_0 = 0.5$ and surfactants diffusion coefficient $D_s = 0.0039$ were used in the following simulations unless other values were specified. The second order accuracy bounce-back condition was used on the walls. Periodic boundary condition was used on the inlet and outlet of the domain to simulate infinitely long channel. The simulations were stopped after the droplet reached its terminal velocity or at the end of the periodic domain. Multiple source terms F were utilized, from which their respective average undisturbed velocities were derived as follows:

$$\bar{U}_u = \frac{R_{ch}{}^2 \Delta p}{8\mu\ell} \tag{7.1}$$

Where μ is the matrix dynamic viscosity. The channel radius R_{ch} was selected as a characteristic length, $U_0 = 2\bar{U}_u$ the undisturbed centerline flow velocity as characteristic velocity and the inverse shearing strain rate $\dot{\gamma}^{-1} = \frac{R_{ch}}{2\left(U_0 - U_{R_{ch}/2}\right)}$ as characteristic time.

The channel average Reynolds number was calculated by:

$$\mathrm{Re} = \frac{2\bar{U}R_{ch}}{\nu} \tag{7.2}$$

Several Weber numbers We for droplet radius R_d resulted from the various simulations, and they have been computed by the following equation:

$$We = \frac{2\rho \bar{U}^2 R_d}{\sigma} \tag{7.3}$$

The constituent fluids properties are shown in the table 7.1.

7.2 Effects of Temperature Changes on the Multiphase Flow Behavior

Two steady-state temperature conditions were used in the following simulations with temperatures10^{o}C and 60^{o}C, respectively. The transient behavior of the O/W emulsion was explored during fluid cooling and heating while using the wall temperature as the temperature gradient driving source. The volume fraction was calculated as the volume of the suspended phase ratio to the total volume of the cylindrical domain, and this led to $\phi_i = 19.8\%$ for the case of three droplets.

Constant pressure gradient per unit length $F = \frac{\Delta p}{\ell} = 2.5 \times 10^{-7}$ leading to an average Reynolds number $\mathrm{Re} = 0.0019$ was used to move the flow from the inlet periodic boundary to the outlet periodic boundary. The temperature dependent Reynolds number range was $0.0016 \le \mathrm{Re} \le 0.033$, which was derived from the utilization of the measured average velocities from all the cases. A shear strain rate $\dot{\gamma} = 8.57 \times 10^{-5}\ ts^{-1}$ was used as the reference for the dimensionless time. The maximum flow velocity of the undisturbed parabolic flow $U_{\max} = 2.96 \times 10^{-5}\ lu/ts$ calculated at 35^{o}C was utilized for the dimensionless analysis of the average flow velocity and for the calculation of the dimensionless time.

The average Weber number was computed as $We = 1.23 \times 10^{-5}$. The temperature dependent Weber number range was $8.2 \times 10^{-6} \le We \le 1.7 \times 10^{-3}$.

Table 7.1: Fluid properties of the mixture constituent fluid in both physical and lattice units

Transformer Oil and Water Physical and Lattice Properties								
Water Properties	**Temperature C°**	**Density Kg/m³**	**Dynamic Viscosity Kg/m.s**	**Kinematic Viscosity m²/s**	**Specific Heat J/kg.K°**	**Thermal Conductivity W/m.K°**	**Prandtl number**	**Thermal Diffusivity m²/s**
	10	999.570	0.001266400	0.000001267	4089.70	0.58839	8.8027	0.000000144
	20	997.780	0.000977200	0.000000979	4076.40	0.60475	6.5870	0.000000149
	30	995.180	0.000777330	0.000000781	4070.20	0.61941	5.1078	0.000000153
	40	991.800	0.000635440	0.000000641	4067.30	0.63247	4.0864	0.000000157
	50	987.680	0.000531850	0.000000538	4066.00	0.64399	3.3580	0.000000160
LBM Properties								
	10	2.316	0.212057306	0.091559755	24.41713	0.58839	8.8000	0.010404520
	20	2.312	0.163623246	0.070774173	24.39973	0.60475	6.6017	0.010720637
	30	2.306	0.13015658	0.056445469	24.39193	0.61941	5.1255	0.011012728
	40	2.298	0.106398489	0.046299463	24.39073	0.63247	4.1032	0.011283804
	50	2.289	0.089053143	0.038913257	24.39673	0.64399	3.3737	0.011534421
Transformer Oil Properties	**Temperature C°**	**Density Kg/m³**	**Dynamic Viscosity Kg/m.s**	**Kinematic Viscosity m²/s**	**Specific Heat J/kg.K°**	**Thermal Conductivity W/m.K°**	**Prandtl number**	**Thermal Diffusivity m²/s**
	10.00	885	0.03345	0.0000378	1650	0.111	0.49722	7.60144×10^{-5}
	20.00	879	0.0211	0.000024	1710	0.111	0.32505	7.38479×10^{-5}
	30.00	873	0.01344	0.0000154	1780	0.11	0.21748	7.07878×10^{-5}
	40.00	867	0.009364	0.0000108	1830	0.109	0.15721	6.86999×10^{-5}
	50.00	860.797	0.006282502	7.29847×10^{-6}	1901.6875	0.10819575	0.11042	6.60952×10^{-5}
LBM Properties								
	10	2.05000	5.536985517	2.700957398	9.94368264	0.111	0.49601	0.005445278
	20	2.03609	3.521098776	1.729341556	10.2589474	0.111	0.32543	0.005314015
	30	2.02220	2.242675988	1.109026052	10.6233465	0.11	0.21658	0.005120431
	40	2.00834	1.517491782	0.755594229	11.0140488	0.109	0.15333	0.004927672
	50	1.99451	1.09036324	0.546682257	11.4082233	0.10819575	0.11496	0.00475506

The surface Péclet number indicating the relation between the flow shear strain rate and the surfactants diffusion was calculated for the individual cases by $Pe_s = \dot{\gamma} R_0^2 / D_s$. This yielded an average Péclet number $Pe_s = 0.316$ when calculated using the undisturbed velocity. The temperature dependent Péclet number range was $0.81 \le Pe \le 2.32$. This was derived from the use of the measured average velocity from each of the individual cases. The dimensionless time was computed as $T_d = \dot{\gamma} \times ts$.

The effects of constant wall temperature changes on the flow behavior were analyzed with respect to the following aspects:

7.2.1 Flow Average Velocity

The main parameters, which influence the flow velocity, are generally dependent on the various terms of the Naiver-Stokes equation, which can be recovered by the LBM through Chapman-Enskog expansion:

$$\frac{\partial u}{\partial t} + u.\nabla u = -\frac{\nabla p}{\rho} + \nu.\nabla^2 u \qquad (7.4)$$

Where ∇p represents pressure gradient, ρ is the density, u is the velocity and ν is kinematic.

For a constant pressure gradient flow such as the one described in the current simulations, the viscosity of the immiscible liquids mixture is expected to drop with the rise of the temperature of the fluids. This tends to diminish the diffusive term in the Navier-Stokes equation and to increased velocity of the fluid

since less energy is transformed into heat. The average velocity is also affected by the suspended phase degree of deformation.

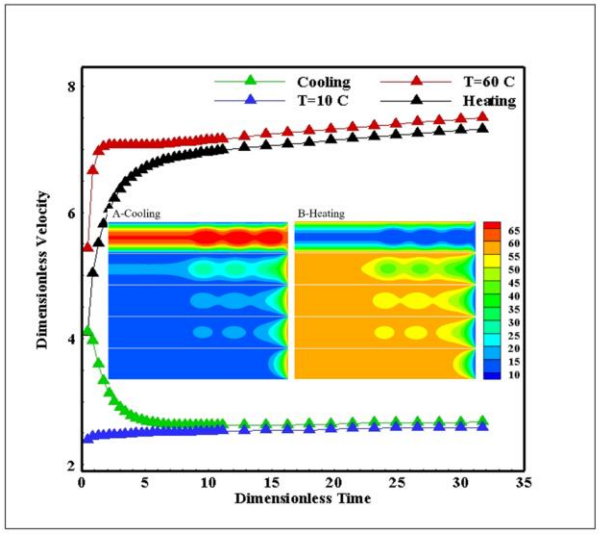

Dimensionless Average Flow Velocity at Different Temperatures

Dimensionless Time	T=10°C	T=60°C	Cooling	Heating
0.43	0.49	1.11	0.84	0.84
4.71	0.51	1.45	0.55	1.37
24.85	0.53	1.52	0.55	1.48
26.56	0.53	1.52	0.55	1.49
28.28	0.53	1.53	0.55	1.49
29.99	0.53	1.53	0.55	1.50
31.70	0.53	1.54	0.55	1.50

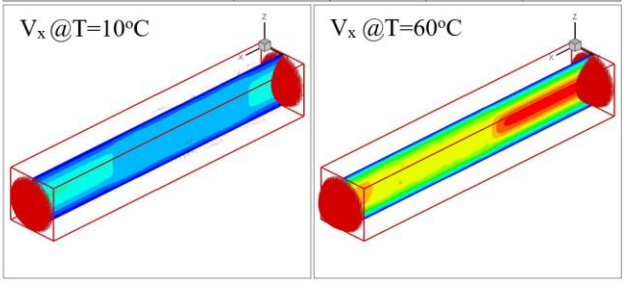

Figure 7.1 Dimensionless average velocity versus dimensionless time for the flow of three droplets simulated at different temperature conditions.

It is clear that the flow temperature influences the surfactants elasticity. A higher flow temperature leads to higher droplet surfactants' elasticity and thus higher droplets' deformation. This allows the droplets to align with the flow, which reduces the flow restriction and leads to higher average flow velocity as shown in Fig 6.1 The average flow velocity, as well as the dimensionless time at different temperature, are normalized by the maximum flow velocity of the undisturbed flow at 35°C.

The insets in the graph depict the temperature contours of the transient heating and cooling cases at different time steps. The table displays the numerical values for the average dimensionless velocities. The contours in the figure

represent central sections for the horizontal velocity of the steady state cases with velocity vectors depicting the parabolic nature of the flow.

7.2.2 Surfactants distribution

The primary effect of surfactants is to reduce the interfacial tension, which causes deformation of the droplets by the addition of Marangoni stresses arising from the gradients in interfacial tension. The overall transport of the surfactants is from the front to the rear of the drop. Due to the convection term $\nabla_s \cdot (\boldsymbol{u}_s \Gamma)$ in the surfactants governing equation the local accumulation of surfactants occurs at the front stagnation point and the rear stagnation ring (converging flow), while a depletion of surfactants is expected at the rear stagnation point (diverging flow).

In addition, because the surface can deform and undergo local changes in surface area, there is a coupling between the drop deformation and the surfactants distribution expressed by $K\Gamma u_n$. There are two consequences of the non-uniform surfactants concentration gradients.

First, high curvature regions develop along the interface where the surface tension is low in order to balance the normal stress jump in these regions. The high curvature regions, in turn, increase surface dilation effects and reduce the surfactants concentration locally.

Second, the interfacial tension gradients induce Marangoni stresses, which oppose the tangential flow along the drop surface due to the non-uniform surfactants distribution. The Marangoni stresses reduce the drop mobility and cause an increase in the extra pressure loss (Johnson and Borhan 1999).

The surfactants distribution corresponding to the lower temperature cases the surfactants distribution remains almost uniform on the droplets over the entire simulation time because the flow conditions lead to a relatively low Péclet numbers compared to the previous hot flows.

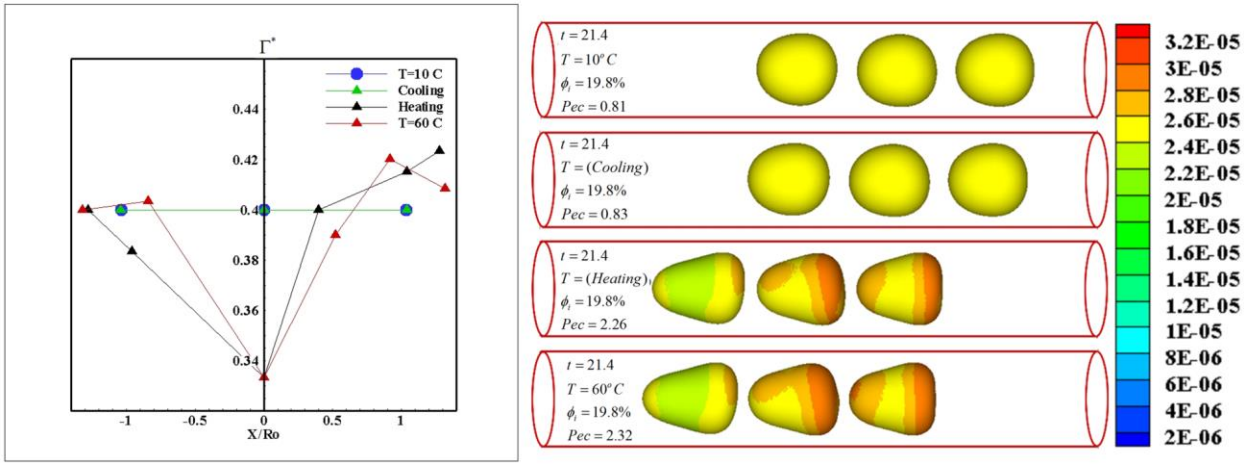

Figure 7.2 Droplets shape and dimensionless surfactants concentration for leading droplet at different temperatures (X) represents the leading droplet major axis half-length and (Ro) is the initial droplet radius.

The surfactants diffusion effects $D_s \nabla_s^2 \Gamma$ are overwhelming when compared to the effects of the convective term $\nabla_s \cdot (\boldsymbol{u}_s \Gamma)$ in Eq. (4.18) and therefore no noticeable surfactants distribution changes are observed. The other factor, which contributes to a stable surfactants concentration, is the lower flow shear stress. Low levels of flow shear stress lead to very humble droplet deformation and thus to small droplet interface surface changes. This means that the shape term $K\Gamma u_n$ in the surfactants governing equation is too small, and a considerable change in the surfactants distribution is not warranted.

The distribution of surfactants for the hot cases (T=60^{o}C and Heating) reveals an accumulation of surfactants at the rear region without much accumulated at the frontal region for the leading droplet. The surfactants accumulation is present on the front and rear stagnation region for the other two droplets. As the leading droplet moves forward, a wake region is formed behind it. The wake helps the following droplets to move forward with reduced tangential velocity and hence fewer effects on surfactants distribution.

The Péclet number for the higher temperature cases is approximately greater by 2.8 times from the Péclet number for the low-temperature cases. The surfactants convection on the surface is, therefore, higher and this helps reduce the surfactants' resistance and let them move and accumulate on the droplets rear surface. On the other hand, higher Péclet number leads to non-uniform surfactants distribution on the surface of the droplet, which makes the droplets deform more than the others from the lower temperature cases. The higher temperature helps in the reduction of the interfacial tension, which causes the droplets to deform and align with the flow. It is important to mention that the increasing in pressure losses to the flow due to the non-uniform surfactants distribution on the droplets, is much smaller than the effect of the higher temperature.

For the cold cases (T=20^{o}C and Cooling) the surfactants' distribution is uniform over the droplets surfaces because of the small Péclet number of these particular cases. The low temperature, associated with high viscosity leads to higher interfacial tension which supports droplets resistance to deformation.

The graph in Fig 7.2 shows the surfactants concentration distribution at different temperatures and the dimensionless surfactants concentration values Γ* for the leading droplets in all cases. The measurement was executed in a central xz plane along the top circumference of the droplet in the direction of the major axis. The coordinate (X) was normalized by the initial droplet radius (R_o).

7.2.3 Leading Droplet Deformation Index

The leading droplet deformation index is calculated by $DI = \frac{a-b}{a+b}$ where *a*, is the drop major axis and *b* is the minor droplet axis. The *DI* is used for quantitative comparison of the droplets deformation from the four simulated cases. The leading droplets in the higher temperature cases have almost three times higher *DI* than the cases with, the lower temperature after reaching steady state. The *DI* of the leading droplets depends mainly on the flow shear strain rate $\dot{\gamma}$ and the surfactants elasticity and distribution; however, the role of shear strain rate outweigh by far the effects of the surfactant elasticity $E_0^{(T)}$.

It is useful to mention from observing Fig 7.3-A that the DI in the transient heating case lags behind the steady-state case, while the transient cooling DI is leading the steady-state case. This is an indication of the lasting effects of the droplets' initial state during heating or cooling.

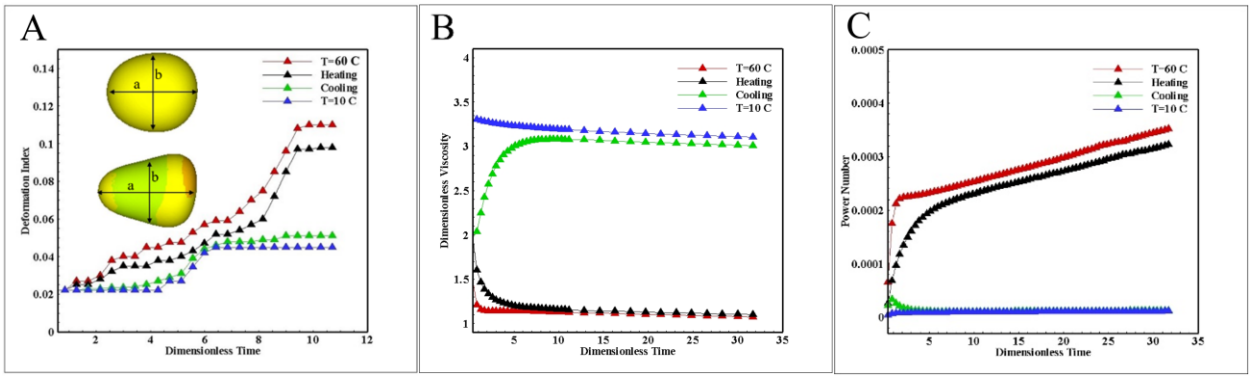

Figure 7.3 (A) Deformation index of the leading droplets (B) Relative viscosities as a function of dimensionless time with different thermal conditions, (C) Power number ratio as a function of dimensionless time at various temperatures.

7.2.4 Rheological Behavior of the Mixture

The dynamic viscosity of the simulated O/W emulsion was assessed by applying the following Poiseuille-Hagen equation for volumetric flow rate:

$$Q = 2\pi\int_0^R u_z r dr = \frac{\pi R_{ch}^4 \Delta p}{8\mu\ell} = \bar{U}_s \times \pi R^2{}_{ch} \Rightarrow \mu = \frac{R_{ch}^2 \Delta p}{8\bar{U}_s \ell} \tag{7.5}$$

Where the average flow velocity $\bar{U}_s$ is measured directly from the simulation data.

The viscosity dependence on temperature is apparent from the fluid properties presented in Table 7.1. The normalized dynamic viscosity of the suspending fluids with respect to the matrix at the simulated conditions are calculated as $\mu_N^w = \mu_{10}^w / \mu_{35}^w = 1.79$ and $\mu_N^w = \mu_{60}^w / \mu_{35}^w = 0.644$. The normalized viscosity of the suspended fluids with respect to the matrix viscosity is computed as $\mu_N^o = \mu_{10}^o / \mu_{35}^w = 47.45$ and $\mu_N^o = \mu_{60}^o / \mu_{35}^w = 6.61$, while the relative viscosities of the

emulsions at steady states for the steady temperatures T= 10ºC and T = 60ºC are reported as $\mu_R^e = \mu_{10}^e / \mu_{35}^w = 3.18$ and $\mu_R^e = \mu_{60}^e / \mu_{35}^w = 1.101$, respectively.

A careful look at the graphs of Fig 7.3-A and Fig 7.3-B shows that the DI is in direct correlation with the rheological behavior of the emulsions in all cases, where a lower DI is associated with higher relative viscosity, while higher DI is associated with lower relative viscosity. Finally, it is interesting to mention that for the transient cases, it takes less time for the emulsion to thin than to thicken before reaching steady state. This is due to the effects of the temperature dependent average flow velocity shown in Fig 6.1, which exhibit gentler absolute slope ($\theta = 71.8^o$)for the cooling case as opposed to the heating case ($\theta = 81.7^o$) during the first five dimensionless time steps.

7.2.5 Flow Power Number

By recalling the power number equations, the hydraulic power due to the movement of the undisturbed flow through the channel is calculated by:

$$\mathrm{P} = Q\,\Delta p = \frac{\pi R^4 F}{8\mu}\Delta p \qquad (7.6)$$

The combined droplets' mass center is evaluated at different time steps, and the suspended phase velocity is calculated by differentiating the mass center displacement using second order accuracy finite difference scheme. A droplet power number is introduced, and it is given by:

$$\mathrm{P}_d = \frac{\rho_d \forall_d V_{dmc}^3}{\ell} \qquad (7.7)$$

The power number here represents the amount of power consumed by the droplets from the flow during their motion; hence a higher ratio $R_P = \frac{\mathrm{P}_d}{P}$ indicates a more efficient system. In this case, the flow utilizes more energy into transporting the necessary component in the system, i.e., the oil as the target fluid.

From Eq. (7.6) the flow hydraulic power is inversely proportional to the dynamic viscosity, which is temperature dependent. Equation (7.7) shows that the power number is directly proportional to the velocity raised to power three. For the power number ratio analysis, a reference suspending fluid temperature of 35^0C is used in the calculation of the hydraulic flow power. The velocity profiles of Fig 7.1 suggest that an increase in temperature leads to larger flow average velocity due to diminishing viscosity and larger droplets compliance as shown in Fig 7.3. The ratio of the two equation determines the outcome of the power number ratio.

It is evident from Fig 7.3-C that the power number ratio for the hot fluids is about 4.5 times higher than the cold cases. Thus, it can be inferred that heating the suspending fluid would lead to an improvement of the suspended fluid transportation by reducing the required pumping power during O/W transportation. The necessary pumping power is equal to the hydraulic power multiplied by the total efficiency of the driving system.

Fig 7.3-C shows a slightly higher power number ratio for the hot transient (heating) case as compared to the hot steady state case. The figure also shows that the cold transient (cooling) case power number ratio is slightly smaller than its corresponding steady-state case. This disposal can be explained by the fact that

the power number is directly proportional to the density of the suspended phase, which is subject to change during cooling and heating.

7.2.6 Notes on the Transient Flow Temperature Distribution

As per our previous discussion, the transient cases were characterized by constant temperature boundaries. The transient heating case inset in Fig 7.1 shows the heat being transferred from the wall to the water and then from water to the oil droplets. It is clear that the oil droplets are the coldest in the thermal system. This is because the oil droplets are located at the centerline of the tube, and they are considered to be the farthest from the heat source, i.e., the wall. Based on the principles of heat transfer, the amount of heat transfer is inversely proportioned to the distance from the heat source.

Furthermore, when the heat reaches the droplets surface it will face higher thermal resistance because the droplets have lower thermal conductivity and heat transfer coefficients. Finally, continuous flow of fresh cold charge of water enters the tube. The suspending phase central flow velocity is usually higher than the droplets velocities. When the suspending phase meets the oil droplets, water with high momentum at the center of the tube pushes the droplets forward and then flow around them, which acts as a cold envelop of water covering the oil droplets and reducing the amount of heat transfer to them and vice versa for the cooling case. The same can be said about the transient cooling case with inversed effects as shown in the transient cooling case of Fig 7.1.

7.3 Effects of the Pressure Gradient on the Multiphase Parabolic Flow Behavior

To study the influence of the pressure gradient on the flow characteristics of the O/W emulsions, two source terms were used $F = \frac{\Delta p}{\ell} = 1.0 \times 10^{-6}$ and $F = \frac{\Delta p}{\ell} = 1.5 \times 10^{-8}$. The steady-state fluid temperature of 60ºC and the volume fraction $\phi_i = 19.8\%$ were employed in the subsequent simulations. For reporting dimensionless results of the simulations, the average flow velocities were normalized by the central undisturbed flow velocity for the three pressure gradients at 60ºC.

Increasing the source term by 4 folds as shown in Fig 7.4, led to an increase in the average velocity of 1.47 times after reaching steady-state velocity. A decrease in the source term by 16.6 folds led to a decrease in the average velocity by 4.25 times at the same time step.

The surfactants distribution for the case with source term $\frac{\Delta p}{\ell} = 1.5 \times 10^{-8}$ shown in Fig 7.5, is characterized by a very low Péclet number and it exhibits no change in the surfactants concentration distribution since the convection due to flow velocity is not sufficient to overcome the diffusion of surfactants on the droplets' interfaces. The surfactants concentration distribution for the follower droplets with $F = \frac{\Delta p}{\ell} = 1.0 \times 10^{-6}$ is influenced by the same conditions explained in

the previous section; however, and due to higher tangential velocities associated with higher shear stress there is a less concentration of surfactants at the frontal tip of the droplet as compared to the baseline.

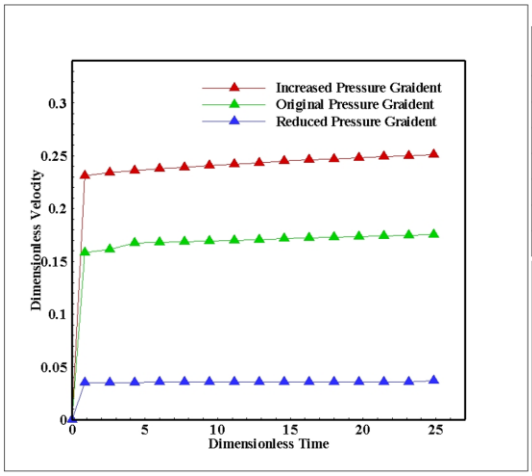

Dimensionless Average Flow Velocity at Different Pressure Gradients

Dimensionless Time	Original Pressure Gradient	Reduced Pressure Gradient	Increased Pressure Gradient
0.86	0.16	0.04	0.23
6.00	0.17	0.04	0.24
11.14	0.17	0.04	0.24
16.28	0.17	0.04	0.25
19.71	0.17	0.04	0.25
21.42	0.17	0.04	0.25
23.13	0.17	0.04	0.25

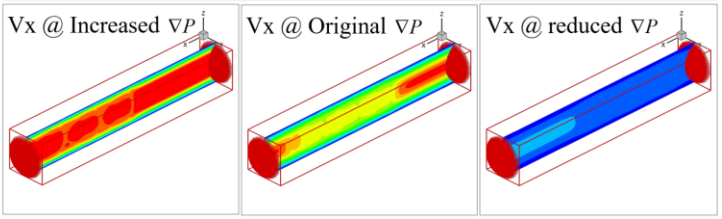

Figure 7.4 Average flow velocities at different pressure gradients as function of the dimensionless time.

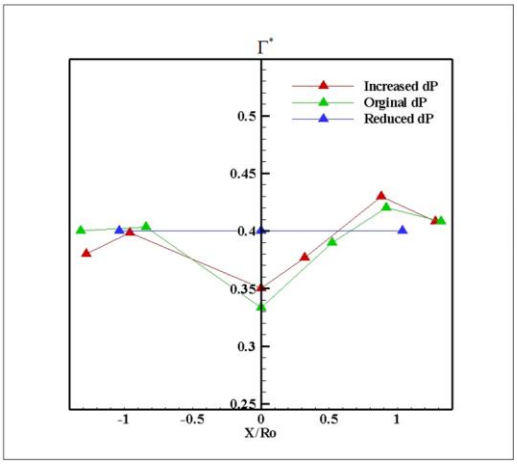

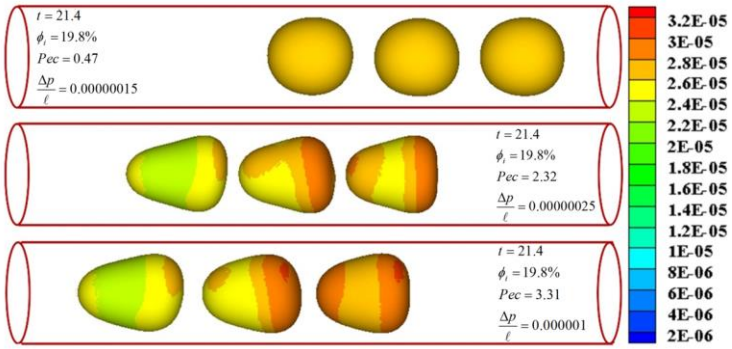

Figure7.5 Droplets shape and dimensionless surfactants concentration for leading droplet at different pressure gradients. (X) represents the leading droplet major axis half-length and (Ro) is the initial droplet radius.

This, in turn, increases the concentration slightly from the middle to the end of the leading droplet despite the fact that the droplet deforms more under this condition.

Fig 7.6-A accounts for the DI of the three simulated conditions. The leading droplet in the higher-pressure gradient case has 3.78 times the value of the DI of the lowest pressure gradient case and the original baseline gradient DI is 3.33 times greater than the reduced pressure gradient after the droplets reached their steady states.

From Fig 7.6-B it is evident that the relative viscosity, which is directly proportional to the increase in the source term and inversely proportional to the average flow velocity as per Eq. (7.5), is increasing with the source term.

This is an indication that the increase in pressure gradient is much higher than the increase in the resulting average flow velocity. For the case, with a lower pressure gradient, the viscosity is mainly affected by the diminished source term. The relative viscosity i.e. the normalized emulsion dynamic viscosity by the water viscosity at 60°C after stabilization is reported as $\mu^e_{R,h} = \mu^e_{high} / \mu^w_{60} = 5.15$ and $\mu^e_{R,l} = \mu^e_{low} / \mu^w_{60} = 0.527$, respectively.

A reference suspending fluid temperature of 60°C in the calculation of the flow hydraulic power. As shown in Fig 7.6-C the power number ratio at dimensionless time step 19.7 and the reduced pressure gradient is equal to 6.06×10^{-6}, while the power number for the baseline pressure gradient is equal to 1.5×10^{-4}. The lower

power number ratio for this case is due to a reduced power number from Eq. (7.7), as a result of smaller droplets velocity.

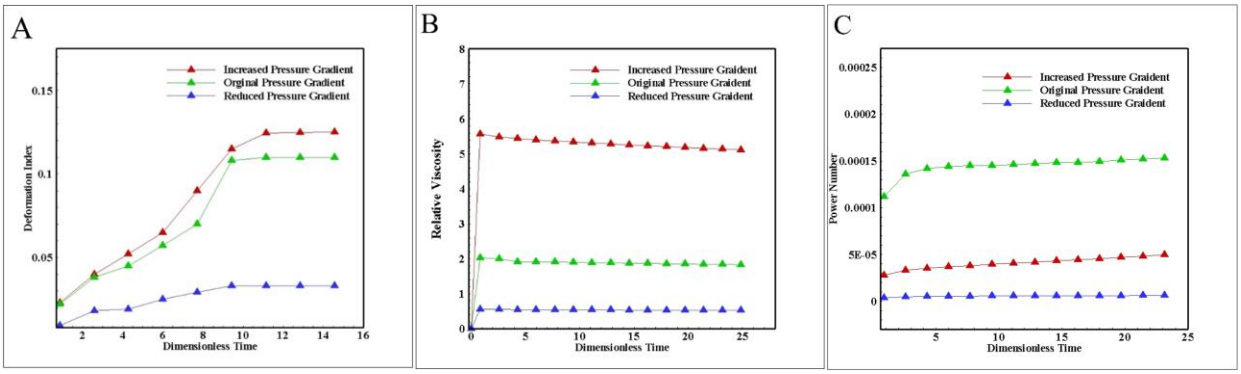

Figure 7.6 (A) Deformation index at different pressure gradients (B) Relative viscosity at various pressure gradients (C) Power number ratio at various pressure gradients.

Finally, for the increased pressure gradient case, the power number is 4.9×10^{-5} which is lower than the power number of the baseline case, since there is higher pressure drop in Eq. (7.6) associated with a higher source term for the same flow and domain.

7.4 Effects of the Volume Fraction on the Multiphase Parabolic Flow Behavior

In the consequent simulations, the volume fraction was changed to $\phi_i = 26.3\%$ by adding one more droplet to the fluid domain while maintaining the same droplets' diameter, temperature, and the simulations' source term. The surfactants conditions were also maintained as from the baseline simulations. The velocity is normalized by the maximum undisturbed flow velocity at 60^{o}C.

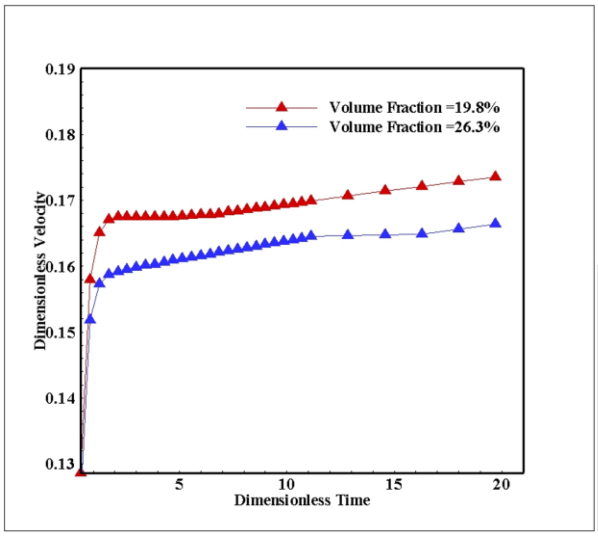

Dimensionless Average Flow Velocity at Different Volume Fractions

Dimensionless Time	V/F=19.8%	V/F=26.3%
0.86	0.15800	0.15180
4.28	0.16750	0.16060
7.28	0.16820	0.16230
10.71	0.16970	0.16420
16.28	0.17210	0.16480
17.99	0.17280	0.16560
19.71	0.17350	0.16640

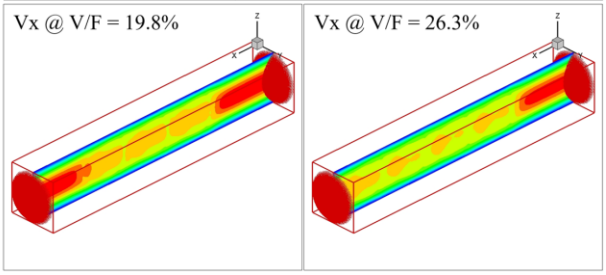

Figure 7.7 Average velocity at different volume fractions.

The average velocity of the flow with the highest volume fraction is less than the flow with lower fraction's velocity because the same source term was used for more number of droplets seeded in the same domain. Fig 7.7 shows the dimensionless velocity for both volume fractions at a different dimensionless time. As reported in the table of Fig 7.7 an increase of 1.328 folds in volume fraction led to a decrease of 1.043 times in the average velocity.

The deformation indices for both volume fractions are shown in Fig 7.9-A. The leading droplet in the domain with $\phi_i = 18.9\%$ has about 1.09 times higher DI than that with $\phi_i = 26.3\%$ due to the difference in average flow velocities between both cases.

From Fig 7.9-B it is clear that increasing the volume fraction increases the viscosity ratio. The relative viscosities of the emulsions with low and high-volume

fractions normalized by the lattice water viscosity at 60°C are reported at the end of the simulations as $\mu_R^e = \mu_{19.8}^e / \mu_{60}^w = 1.864$ and $\mu_R^e = \mu_{26.3}^e / \mu_{60}^w = 1.947$, respectively.

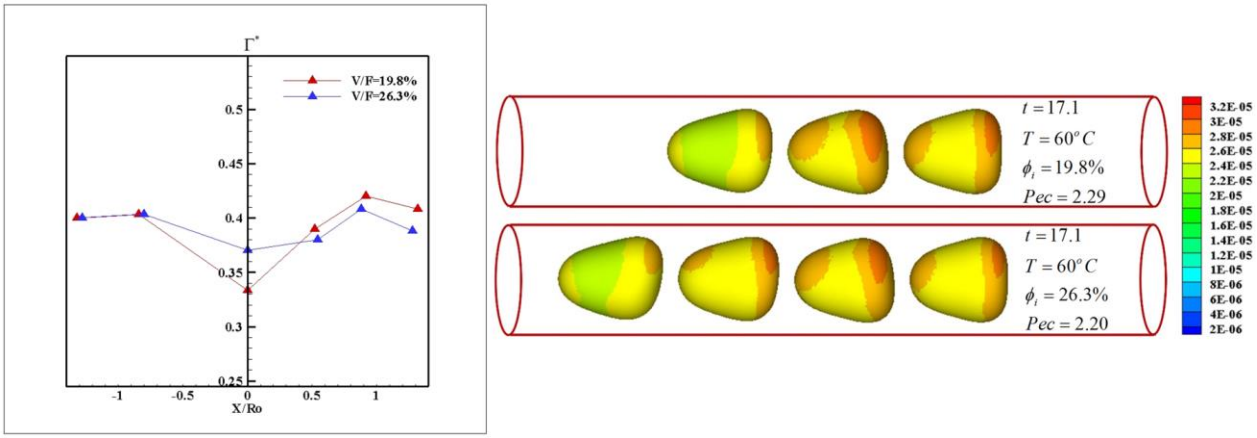

Figure 7.8 Droplets shape and dimensionless surfactants concentration for the leading droplet at different volume fractions. (X) represents the leading droplet major axis half-length and (Ro) is the initial droplet radius.

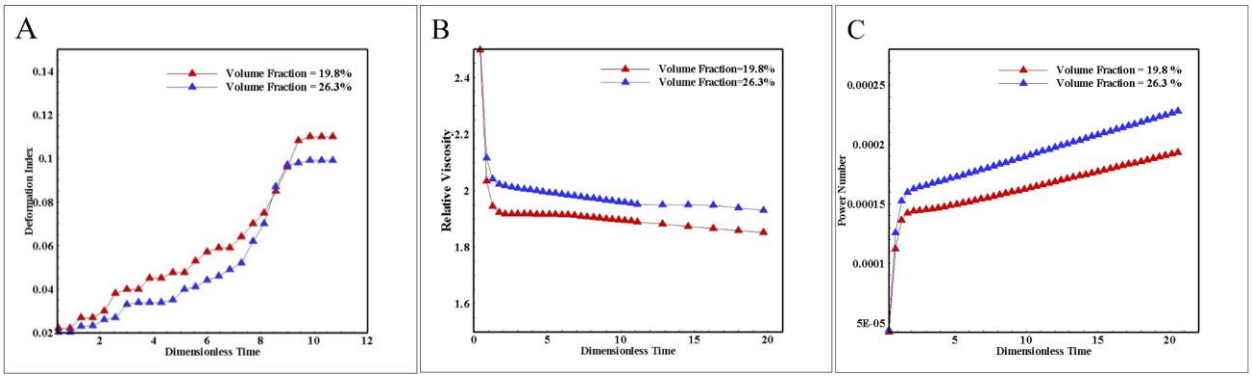

Figure 7.9 (A) Droplets deformation index at different volume fractions (B) Viscosity at different volume fractions (C) Power number at different volume fractions.

The calculated power numbers at dimensionless time step=20 for $\phi_i = 18.9\%$ and $\phi_i = 26.3\%$ are 1.97×10^{-3} and 2.33×10^{-3}, respectively. The higher

volume fraction case indicates a more efficient system. Although the average flow velocity is lower for the higher volume fraction case, its droplets' velocity is about 0.9534 times of the low volume fraction droplets' velocity; however, because the combined droplets' volume is about 1.33 times bigger, the higher volume fraction system possesses higher power number ratio.

7.5 Effects of Surfactants Concentration the Multiphase Parabolic Flow Behavior

In the following simulation, the dimensionless surfactant concentration is increased from $\Gamma^* = 0.4$ to $\Gamma^* = 0.5$, other simulation conditions were maintained as in the baseline simulations. Two source terms are used here, the initial one $\frac{\Delta p}{\ell} = 2.5\times10^{-7}$ and a reduced source term $\frac{\Delta p}{\ell} = 1.5\times10^{-7}$. The temperature of the fluid and the wall were fixed at 60ºC. The velocity and viscosity were normalized by the maximum undisturbed flow velocity and water viscosity at 60ºC.

A flow characterized by $\frac{\Delta p}{\ell} = 2.5\times10^{-7}$ does not show any impact of surfactants concentration on the average flow velocity, nor on the shape, rheology and other flow characteristics.

With the lower source term $\frac{\Delta p}{\ell} = 1.5\times10^{-7}$, the high surfactants concentration had a remarkable influence on the average flow velocity as shown Fig 7.10. The droplets deformation, in this case, is mainly due to the surfactants concentration influence on their interfacial tension rather than the shear stress caused by the flow in

confinement. The more deformable droplets are less restrictive to the flow, hence the increase in the average flow velocity.

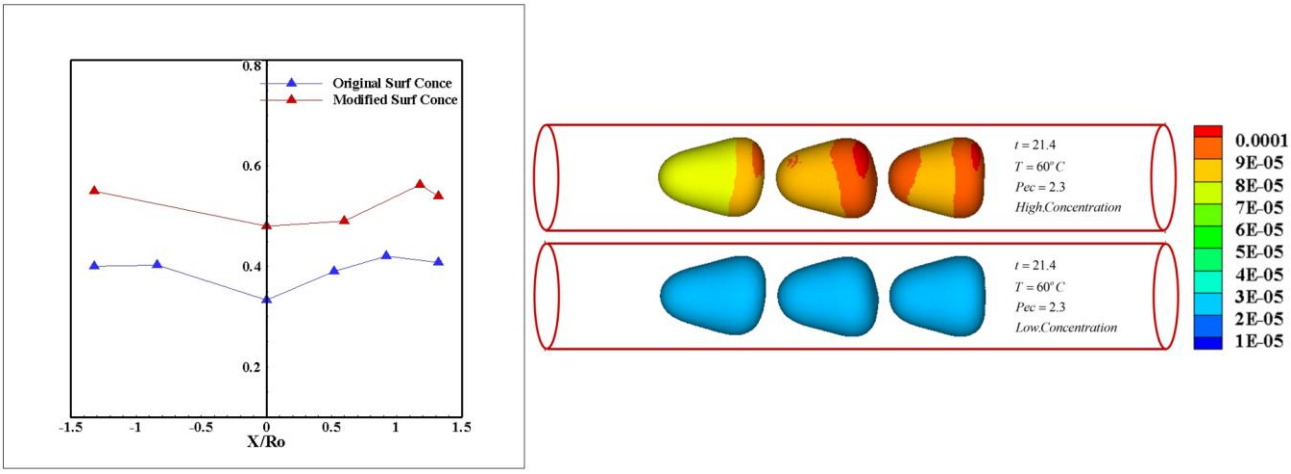

Figure 7.10 Droplets dimensionless surfactants concentration for the leading droplet with the original source term and different surfactants concentrations. (X) Represents the leading droplet major axis half-length and (Ro) is the initial droplet radius. In the low concentration simulation figure, the distribution is not obvious because of scaling.

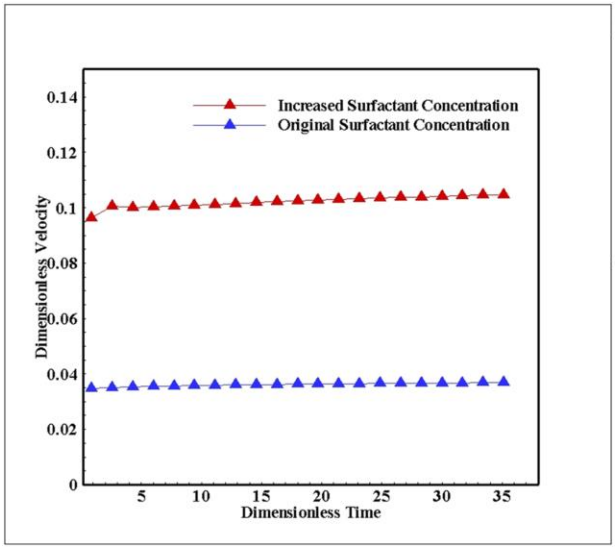

Dimensionless Average Flow Velocity at Different Surfactant Concentrations

Dimensionless Time	Original Surfactant Concentration	Increased Surfactant Concentration
2.57	0.0350	0.1004
7.71	0.0356	0.1005
16.28	0.0361	0.1021
24.84	0.0365	0.1035
31.70	0.0367	0.1043
33.41	0.0367	0.1044
35.13	0.0368	0.1046

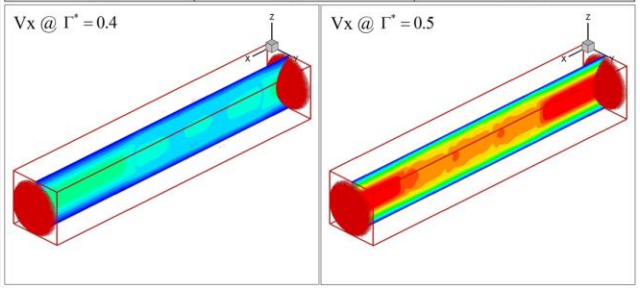

Figure 7.11 Average velocity at different surfactant concentrations.

The surfactants distribution shown in Fig 7.11, is an expression of the effects of the convective and the shape change terms in the surfactants governing equation Eq. (4.18). The leading droplet exhibits more depletion at its frontal zone since it is moving at higher speed due to the nature of the parabolic flow. The follower droplets move in the wake of the leading one and have smaller depletion at their frontal zones. Droplets with lower surfactants concentration are less deformable, and their surfactants distribution is almost constant and is stabilized mainly by diffusion.

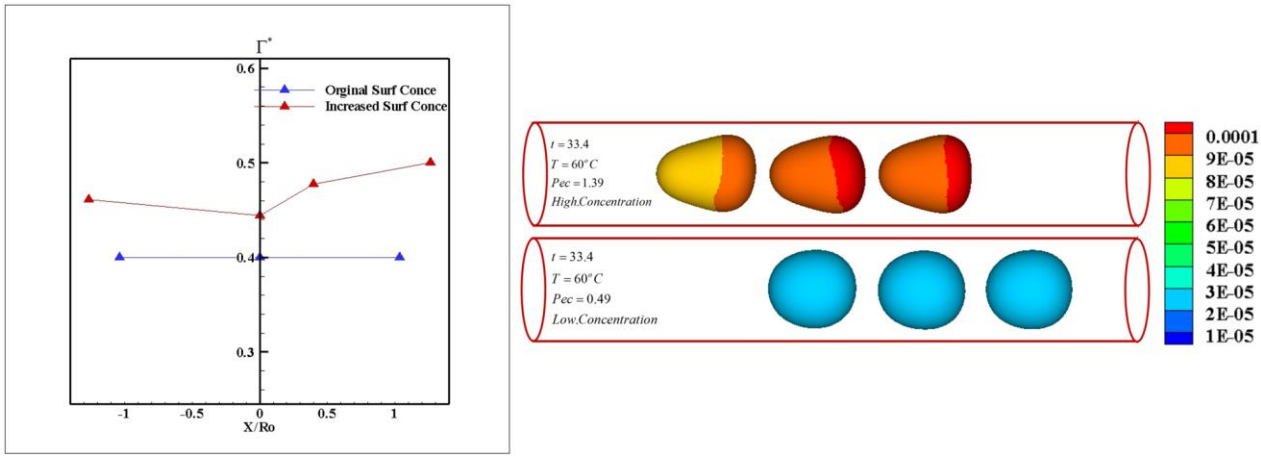

Figure 7.12 Droplets dimensionless surfactants concentration for the leading droplets at the reduced source term and different surfactants concentrations. (X) represents the leading droplet major axis half-length and (Ro) is the initial droplet radius.

The relative viscosity of the flow with the higher surfactants concentration is well below, the lower surfactants case since the flow is less restrictive in the first

case. The relative viscosities for the simulated high and low concentrations cases are $\mu_R^e = \mu_{h.c}^e / \mu_{60}^w = 3.07$ and $\mu_R^e = \mu_{l.c}^e / \mu_{60}^w = 8.73$, respectively.

The power number ratio is much higher in the high concentration case than the low concentration, and this is mainly due to the increased droplets velocities which are raised to cubic power in Eq. (7.7).

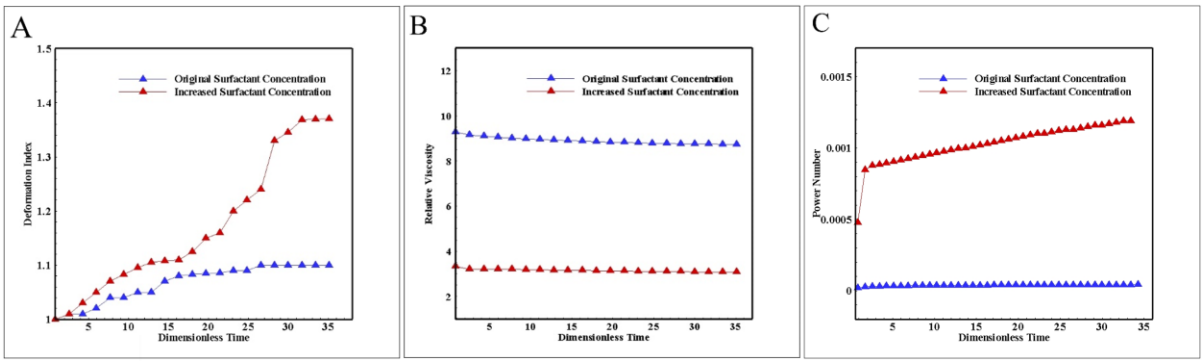

Figure 7.13 (A) Droplets Deformation Index at different surfactants concentrations (B) Viscosity at various surfactants concentrations (C) Power Number at different surfactants concentrations.

CHAPTER 8 CONCLUSIONS AND RECOMMENDATIONS

8.1 Conclusion

In this research, three unique models have presented: Hybrid quasi-steady thermal LBM with surfactants for studying the rheology of surfactants contaminated emulsions at different temperatures. Hybrid quasi-steady thermal LBM with contact angles for studying the effects of temperature, surface energy and physics of interface on deposited emulsions on walls, Hybrid quasi-steady thermal LBM with contact angles and surfactants for studying the effects of temperature, surfactants, surface energy and physics of interface on oils.

8.1.1 Hybrid Quasi-Steady Thermal LBM with Surfactants

A quasi-steady thermal-surfactants hybrid Boltzmann model was presented. The model was validated by comparison with some experimental results. The simulations at different temperatures showed good agreement with the rheological finding of similar experimental conditions for surfactants contaminated O/W emulsions. Furthermore, the model was used for the solution of a transient thermal problem. The coupling of the energy equation with surfactants was tested, and the simulation showed reasonable results. The transient model capabilities motivate the future use of the model in more complex flow simulations.

8.1.2 Hybrid Quasi-Steady Thermal LBM with Contact Angles

The model presented in this was used to analyze the behavior of O/W systems under different thermal and surface conditions. The results for the static contact angle showed an excellent agreement between the model and theoretical results at a variety of conditions. The single slug, two slugs, and droplets flow simulations showed that the temperature plays a significant role in controlling the velocity, power and contact angles of the system. The simulation results helped in better understanding the intricate relationship between temperature and contact angle on the mechanism for transporting O/W mixtures in confined spaces due to temperature and surface energy changes.

8.1.3 Hybrid Quasi-Steady Thermal LBM with Contact Angle and Surfactants

The previous model is extended to include the effect of surfactants and using the model in studying the behavior of O/W systems under different thermal and surface conditions with and without adding surfactants. The slug and droplet flow simulations showed that the surfactants played a major role in controlling the velocity and required pumping power of the system. The simulation results helped in better understanding the intricate relationship between temperature, surfactants and contact angle on the mechanism for transporting O/W mixtures in confined spaces due to temperature and surface energy changes.

8.2 Recommendations for Future Work

The recommendation for future works with relation to the current work are:

- Extending the study on the hybrid quasi-steady thermal LBM with contact angles and surfactants to include the 3-dimensional simulation which gives a better understanding of the problem.
- Investigation the effects of surfactants initial and saturation concentrations on the behavior of trapped oil slugs and droplets.
- Tuning the temperature after optimizing the surfactants type to get minimum pumping power consumed.
- Introducing the multi relaxation time to get more accurate results.

REFERENCES

Abbassi-Sourki, F., Bousmina, M. and Huneault, M.A., 2012. Effect of interfacial modifier on single drop deformation and breakup in step increasing shear flow. Rheologica acta, 51(2), pp.111-126.

Al-Hadhrami, H.S. and Blunt, M.J., 2000, January. Thermally induced wettability alteration to improve oil recovery in fractured reservoirs. In SPE/DOE Improved Oil Recovery Symposium. Society of Petroleum Engineers.

Almatroushi, E. and Borhan, A., 2004. Surfactant Effect on the Buoyancy-Driven Motion of Bubbles and Drops in a Tube. Annals of the New York Academy of Sciences, 1027(1), pp.330-341.

Alvarado, V. and Manrique, E., 2010. Enhanced oil recovery: an update review. Energies, 3(9), pp.1529-1575.

Babadagli, T., 1996. Temperature effect on heavy-oil recovery by imbibition in fractured reservoirs. Journal of Petroleum Science and Engineering, 14(3-4), pp.197-208.

Baret, J.C., 2012. Surfactants in droplet-based microfluidics. Lab on a Chip, 12(3), pp.422-433.

Baroud, C.N., Gallaire, F. and Dangla, R., 2010. Dynamics of microfluidic droplets. Lab on a Chip, 10(16), pp.2032-2045.

Bayareh, M. and Mortazavi, S., 2011. Binary collision of drops in simple shear flow at finite Reynolds numbers: Geometry and viscosity ratio effects. Advances in Engineering Software, 42(8), pp.604-611.

Bedrikovetsky, P., 2013. Mathematical theory of oil and gas recovery: with applications to ex-USSR oil and gas fields (Vol. 4). Springer Science & Business Media.

Bentley, B.J. and Leal, L.G., 1986. An experimental investigation of drop deformation and breakup in steady, two-dimensional linear flows. Journal of Fluid Mechanics, 167, pp.241-283.

Bisanda, E.T.N., 2000. The effect of alkali treatment on the adhesion characteristics of sisal fibres. Applied Composite Materials, 7(5), pp.331-339.

Carslaw, H.S. and Jaeger, J.C., 1959. Heat in solids (Vol. 1). Clarendon Press, Oxford.

Chang-Zhi, L. and Lie-Jin, G., 2007. Numerical simulation of drop deformation and breakup in shear flow. Heat Transfer-Asian Research, 36(5), pp.286-294.

Chen, H., Chen, S. and Matthaeus, W.H., 1992. Recovery of the Navier-Stokes equations using a lattice-gas Boltzmann method. Physical Review A, 45(8), p.R5339.

Cheng, J., Xu, S., Wen, L. and Chen, J., 2005. Steric repulsion between internal aqueous droplets and the external aqueous phase in double emulsions. Langmuir, 21(25), pp.12047-12052.

Dalgleish, D.G., 2006. Food emulsions—their structures and structure-forming properties. Food hydrocolloids, 20(4), pp.415-422.

Dan, D. and Jing, G., 2006. Apparent viscosity prediction of non-Newtonian water-in-crude oil emulsions. Journal of Petroleum Science and Engineering, 53(1), pp.113-122.

De Gennes, P.G., Brochard-Wyart, F. and Quéré, D., 2013. Capillarity and wetting phenomena: drops, bubbles, pearls, waves. Springer Science & Business Media.

De Haan, H.J. and Van Lookeren, J., 1969. Early results of the first large-scale steam soak project in the Tia Juana Field, Western Venezuela. Journal of Petroleum Technology, 21(01), pp.101-110.

Debruijn, R.A., 1991. Deformation and breakup of drops in simple shear flows.

Dessoly, V., Melkote, S.N. and Lescalier, C., 2004. Modeling and verification of cutting tool temperatures in rotary tool turning of hardened steel. International Journal of Machine Tools and Manufacture, 44(14), pp.1463-1470.

Doddi, S.K. and Bagchi, P., 2009. Three-dimensional computational modeling of multiple deformable cells flowing in microvessels. Physical Review E, 79(4), p.046318.

d'Ortona, U., Salin, D., Cieplak, M., Rybka, R.B. and Banavar, J.R., 1995. Two-color nonlinear Boltzmann cellular automata: surface tension and wetting. Physical Review E, 51(4), p.3718.

Drumright-Clarke, M.A., 2002. Numerical simulations that characterize the effects of surfactant on droplets in shear flow (Doctoral dissertation).

Drumright-Clarke, M.A. and Renardy, Y., 2004. The effect of insoluble surfactant at dilute concentration on drop breakup under shear with inertia. Physics of fluids, 16(1), pp.14-21.

Dupin, M.M., Halliday, I. and Care, C.M., 2003. Multi-component lattice Boltzmann equation for mesoscale blood flow. Journal of Physics A: Mathematical and General, 36(31), p.8517.

Eggleton, C.D., Tsai, T.M. and Stebe, K.J., 2001. Tip streaming from a drop in the presence of surfactants. Physical Review Letters, 87(4), p.048302.

Eggleton, C.D. and Stebe, K.J., 1998. An adsorption–desorption-controlled surfactant on a deforming droplet. Journal of colloid and interface science, 208(1), pp.68-80.

Ernandez, J., 2009. EOR Projects in Venezuela: Past and Future. ACI Optimising EOR Strategy, pp.11-12.

Farhat, H., Choi, W. and Lee, J.S., 2010. Migrating multi-block lattice Boltzmann model for immiscible mixtures: 3D algorithm development and validation. Computers & Fluids, 39(8), pp.1284-1295.

Farhat, H., Celiker, F., Singh, T. and Lee, J.S., 2011. A hybrid lattice Boltzmann model for surfactant-covered droplets. Soft Matter, 7(5), pp.1968-1985.

Farhat, H. and Lee, J.S., 2011. Suppressing the coalescence in the multi-component lattice Boltzmann method. Microfluidics and nanofluidics, 11(2), pp.137-143.

Feigl, K., Megias-Alguacil, D., Fischer, P. and Windhab, E.J., 2007. Simulation and experiments of droplet deformation and orientation in simple shear flow with surfactants. Chemical engineering science, 62(12), pp.3242-3258.

Ganesan, S., Rajasekaran, S. and Tobiska, L., 2014. Numerical modeling of the non-isothermal liquid droplet impact on a hot solid substrate. International Journal of Heat and Mass Transfer, 78, pp.670-687.

Greco, F., 2002. Drop deformation for non-Newtonian fluids in slow flows. Journal of non-newtonian fluid mechanics, 107(1), pp.111-131.

Green, D.W. and Willhite, G.P., 1998. Enhanced oil Recovery, vol. 6. SPE Textbook Series, TX, USA.

Girifalco, L.A. and Good, R.J., 1957. A theory for the estimation of surface and interfacial energies. I. Derivation and application to interfacial tension. The Journal of Physical Chemistry, 61(7), pp.904-909.

Gomari, K.R., Denoyel, R. and Hamouda, A.A., 2006. Wettability of calcite and mica modified by different long-chain fatty acids (C 18 acids). Journal of colloid and interface science, 297(2), pp.470-479.

Gomari, K.R. and Hamouda, A.A., 2006. Effect of fatty acids, water composition and pH on the wettability alteration of calcite surface. Journal of petroleum science and engineering, 50(2), pp.140-150.

Guggenheim, E.A., 1945. The principle of corresponding states. The Journal of Chemical Physics, 13(7), pp.253-261.

Guido, S. and Preziosi, V., 2010. Droplet deformation under confined Poiseuille flow. Advances in colloid and interface science, 161(1), pp.89-101.

Gunstensen, A.K., Rothman, D.H., Zaleski, S. and Zanetti, G., 1991. Lattice Boltzmann model of immiscible fluids. Physical Review A, 43(8), p.4320.

Guo, Z., Zheng, C. and Shi, B., 2002. Discrete lattice effects on the forcing term in the lattice Boltzmann method. Physical Review E, 65(4), p.046308.

Guo, Z., Shi, B. and Wang, N., 2000. Lattice BGK model for incompressible Navier–Stokes equation. Journal of Computational Physics, 165(1), pp.288-306.

Halliday, I., Law, R., Care, C.M. and Hollis, A., 2006. Improved simulation of drop dynamics in a shear flow at low Reynolds and capillary number. Physical review E, 73(5), p.056708.

Halliday, I., Hollis, A.P. and Care, C.M., 2007. Lattice Boltzmann algorithm for continuum multicomponent flow. Physical Review E, 76(2), p.026708.

Hamouda, A.A. and Rezaei Gomari, K.A., 2006, January. Influence of temperature on wettability alteration of carbonate reservoirs. In SPE/DOE Symposium on Improved Oil Recovery. Society of Petroleum Engineers.

Hamouda, A.A., Karoussi, O. and Chukwudeme, E.A., 2008. Relative permeability as a function of temperature, initial water saturation and flooding fluid compositions for modified oil-wet chalk. Journal of Petroleum Science and Engineering, 63(1), pp.61-72.

Han, D.K., Yang, C.Z., Zhang, Z.Q., Lou, Z.H. and Chang, Y.I., 1999. Recent development of enhanced oil recovery in China. Journal of Petroleum Science and Engineering, 22(1), pp.181-188.

Haq, A.N. and Tamizharasan, T., 2006. Investigation of the effects of cooling in hard turning operations. The International Journal of Advanced Manufacturing Technology, 30(9-10), pp.808-816.

Hollis, A.P., Halliday, I. and Law, R., 2007. Kinematic condition for multicomponent lattice Boltzmann simulation. Physical Review E, 76(2), p.026709.

Hu, Y.T. and Lips, A., 2003. Estimating surfactant surface coverage and decomposing its effect on drop deformation. Physical review letters, 91(4), p.044501.

Inamuro, T., Tomita, R. and Ogino, F., 2003. Lattice Boltzmann simulations of drop deformation and breakup in shear flows. International Journal of Modern Physics B, 17(01n02), pp.21-26.

Jaeger, J.G., 1942. Moving sources of hear and the temperature at sliding contacts. In J. Proc. Roy. Soc. NSW (Vol. 76, pp. 203-224).

Jakiela, S., Korczyk, P.M., Makulska, S., Cybulski, O. and Garstecki, P., 2012. Discontinuous transition in a laminar fluid flow: A change of flow topology inside a droplet moving in a micron-size channel. Physical review letters, 108(13), p.134501.

Janssen, J.J.M., Boon, A. and Agterof, W.G.M., 1994. Influence of dynamic interfacial properties on droplet breakup in simple shear flow. AIChE journal, 40(12), pp.1929-1939.

Janssen, P.J.A. and Anderson, P.D., 2008. Surfactant-covered drops between parallel plates. Chemical Engineering Research and Design, 86(12), pp.1388-1396.

Jen, T.C., Gutierrez, G., Eapen, S., Barber, G., Zhao, H., Szuba, P.S., Labataille, J. and Manjunathaiah, J., 2002. Investigation of heat pipe cooling in drilling applications.: part I: preliminary numerical analysis and verification. International Journal of Machine Tools and Manufacture, 42(5), pp.643-652.

Jeon, H.K. and Macosko, C.W., 2003. Visualization of block copolymer distribution on a sheared drop. Polymer, 44(18), pp.5381-5386.

Karoussi, O. and Hamouda, A.A., 2007. Imbibition of sulfate and magnesium ions into carbonate rocks at elevated temperatures and their influence on wettability alteration and oil recovery. Energy & fuels, 21(4), pp.2138-2146.

Karoussi, O. and Hamouda, A.A., 2008. Macroscopic and nanoscale study of wettability alteration of oil-wet calcite surface in presence of magnesium and sulfate ions. Journal of colloid and interface science, 317(1), pp.26-34.

Katayama, M., 1916. Tokohu Imp. Univ. Sci. Repts, 4, p.373.

Kinoshita, H., Kaneda, S., Fujii, T. and Oshima, M., 2007. Three-dimensional measurement and visualization of internal flow of a moving droplet using confocal micro-PIV. Lab on a Chip, 7(3), pp.338-346.

Kleshchanok, D. and Lang, P.R., 2007. Steric repulsion by adsorbed polymer layers studied with total internal reflection microscopy. Langmuir, 23(8), pp.4332-4339.

Komanduri, R. and Hou, Z.B., 2001. Thermal modeling of the metal cutting process—Part II: temperature rise distribution due to frictional heat source at the tool–chip interface. International Journal of Mechanical Sciences, 43(1), pp.57-88.

Kokal, S. and Al-Kaabi, A., 2010. Enhanced oil recovery: challenges & opportunities. World Petroleum Council: Official Publication, 64.

Kondaraju, S., Farhat, H. and Lee, J.S., 2012. Study of aggregational characteristics of emulsions on their rheological properties using the lattice Boltzmann approach. Soft Matter, 8(5), pp.1374-1384.

Kowalewski, T.A., 1984. Concentration and velocity measurements in the flow of droplet suspensions through a tube. Experiments in fluids, 2(4), pp.213-219.

Kruijt-Stegeman, Y.W., van de Vosse, F.N. and Meijer, H.E.H., 2004. Droplet behavior in the presence of insoluble surfactants. Physics of Fluids, 16(8), pp.2785-2796.

Kundu, P., Kumar, V. and Mishra, I.M., 2015. Modeling the steady-shear rheological behavior of dilute to highly concentrated oil-in-water (o/w)

emulsions: Effect of temperature, oil volume fraction and anionic surfactant concentration. Journal of Petroleum Science and Engineering, 129, pp.189-204.

Kundu, P. and Mishra, I.M., 2013. Removal of emulsified oil from oily wastewater (oil-in-water emulsion) using packed bed of polymeric resin beads. Separation and Purification Technology, 118, pp.519-529.

Lai, M.C., Tseng, Y.H. and Huang, H., 2008. An immersed boundary method for interfacial flows with insoluble surfactant. Journal of Computational Physics, 227(15), pp.7279-7293.

Lake, L.W., 1989. Enhanced oil recovery.

Latt, J., 2007. Hydrodynamic limit of lattice Boltzmann equations (Doctoral dissertation, University of Geneva).

Li, G., Zhai, L., Xu, G., Shen, Q., Mao, H. and Pei, M., 2000. Current tertiary oil recovery in China. Journal of dispersion science and technology, 21(4), pp.367-408.

Lishchuk, S.V., Care, C.M. and Halliday, I., 2003. Lattice Boltzmann algorithm for surface tension with greatly reduced microcurrents. Physical review E, 67(3), p.036701.

Lishchuk, S.V., Halliday, I. and Care, C.M., 2008. Multicomponent lattice Boltzmann method for fluids with a density contrast. Physical Review E, 77(3), p.036702.

Li, X. and Pozrikidis, C., 1997. The effect of surfactants on drop deformation and on the rheology of dilute emulsions in Stokes flow. Journal of Fluid Mechanics, 341, pp.165-194.

Li, X. and Pozrikidis, C., 2000. Wall-bounded shear flow and channel flow of suspensions of liquid drops. International journal of multiphase flow, 26(8), pp.1247-1279.

Loewenberg, M. and Hinch, E.J., 1996. Numerical simulation of a concentrated emulsion in shear flow. Journal of Fluid Mechanics, 321, pp.395-419.

Lovick, J. and Angeli, P., 2004. Droplet size and velocity profiles in liquid–liquid horizontal flows. Chemical Engineering Science, 59(15), pp.3105-3115.

Lyu, S., Jones, T.D., Bates, F.S. and Macosko, C.W., 2002. Role of block copolymers on suppression of droplet coalescence. Macromolecules, 35(20), pp.7845-7855.

Manrique, E.J. and Pereira, C.A., 2007, January. Identifying viable EOR thermal processes in Canadian Tar sands. In Canadian International Petroleum Conference. Petroleum Society of Canada.

Milliken, W.J., Stone, H.A. and Leal, L.G., 1993. The effect of surfactant on the transient motion of Newtonian drops. Physics of Fluids A: Fluid Dynamics, 5(1), pp.69-79.

Moritis, G., 2008. SPECIAL REPORT: More US EOR projects start but EOR production continues decline. Oil and Gas Journal, 106(15), p.41.

Morrow, N.R., 1990. Interfacial phenomena in petroleum recovery. CRC Press.

Mortazavi, S., Afshar, Y. and Abbaspour, H., 2011. Numerical simulation of two-dimensional drops suspended in simple shear flow at nonzero Reynolds numbers. Journal of Fluids Engineering, 133(3), p.031303.

Mortazavi, S.A.E.E.D. and Tryggvason, G., 2000. A numerical study of the motion of drops in Poiseuille flow. Part 1. Lateral migration of one drop. Journal of Fluid Mechanics, 411, pp.325-350.

Mulligan, M.K. and Rothstein, J.P., 2011. The effect of confinement-induced shear on drop deformation and breakup in microfluidic extensional flows. Physics of Fluids, 23(2), p.022004.

Mulligan, M.K., 2012. Morphology and development of droplet deformation under flow within microfluidic devices. University of Massachusetts Amherst.

Nourbakhsh, A., Mortazavi, S. and Afshar, Y., 2011. Three-dimensional numerical simulation of drops suspended in Poiseuille flow at non-zero Reynolds numbers. Physics of Fluids, 23(12), p.123303.

Nosonovsky, M. and Bhushan, B., 2005. Roughness optimization for biomimetic superhydrophobic surfaces. Microsystem Technologies, 11(7), pp.535-549.

Nosonovsky, M., 2007. On the range of applicability of the Wenzel and Cassie equations. Langmuir, 23(19), pp.9919-9920.

Nott, P.R. and Brady, J.F., 1994. Pressure-driven flow of suspensions: simulation and theory. Journal of Fluid Mechanics, 275, pp.157-199.

Núñez, G.A., Briceño, M., Mata, C., Rivas, H. and Joseph, D.D., 1996. Flow characteristics of concentrated emulsions of very viscous oil in water. Journal of Rheology, 40(3), pp.405-423.

Oishi, M., Kinoshita, H., Fujii, T. and Oshima, M., 2009. Confocal micro-PIV measurement of droplet formation in a T-shaped micro-junction. In Journal of Physics: Conference Series (Vol. 147, No. 1, p. 012061). IOP Publishing.

Okiishi, M.Y., Munson, B. and Young, D., 2006. Fundamentals of fluid mechanics. John Wiley & Sons, Inc.

Partal, P., Guerrero, A., Berjano, M. and Gallegos, C., 1997. Influence of concentration and temperature on the flow behavior of oil-in-water emulsions stabilized by sucrose palmitate. Journal of the American Oil Chemists' Society, 74(10), pp.1203-1212.

Pawar, Y. and Stebe, K.J., 1996. Marangoni effects on drop deformation in an extensional flow: The role of surfactant physical chemistry. I. Insoluble surfactants. Physics of Fluids, 8(7), pp.1738-1751.

Reis, T. and Phillips, T.N., 2007. Lattice Boltzmann model for simulating immiscible two-phase flows. Journal of Physics A: Mathematical and Theoretical, 40(14), p.4033.

Rezaei Gomari, K.A., Karoussi, O. and Hamouda, A.A., 2006, January. Mechanistic study of interaction between water and carbonate rocks for enhancing oil recovery. In SPE Europec/EAGE Annual Conference and Exhibition. Society of Petroleum Engineers.

Saiki, Y., Prestidge, C.A. and Horn, R.G., 2007. Effects of droplet deformability on emulsion rheology. Colloids and Surfaces A: Physicochemical and Engineering Aspects, 299(1), pp.65-72.

Sharma, V.S., Dogra, M. and Suri, N.M., 2009. Cooling techniques for improved productivity in turning. International Journal of Machine Tools and Manufacture, 49(6), pp.435-453.

Shui, L., Eijkel, J.C. and van den Berg, A., 2007. Multiphase flow in microfluidic systems–Control and applications of droplets and interfaces. Advances in Colloid and Interface Science, 133(1), pp.35-49.

Staben, M.E., Zinchenko, A.Z. and Davis, R.H., 2003. Motion of a particle between two parallel plane walls in low-Reynolds-number Poiseuille flow. physics of fluids, 15(6), pp.1711-1733.

Stone, H.A. and Leal, L.G., 1990. The effects of surfactants on drop deformation and breakup. Journal of Fluid Mechanics, 220, pp.161-186.

Sundararaj, U. and Macosko, C.W., 1995. Drop breakup and coalescence in polymer blends: the effects of concentration and compatibilization. Macromolecules, 28(8), pp.2647-2657.

Taghilou, M. and Rahimian, M.H., 2014. Lattice Boltzmann model for thermal behavior of a droplet on the solid surface. International Journal of Thermal Sciences, 86, pp.1-11.

Tang, G.Q. and Kovscek, A.R., 2004. An experimental investigation of the effect of temperature on recovery of heavy oil from diatomite. SPE Journal, 9(02), pp.163-179.

Thomas, S., 2008. Enhanced oil recovery-an overview. Oil & Gas Science and Technology-Revue de l'IFP, 63(1), pp.9-19.

Van der Graaf, S., 2006. Membrane emulsification: droplet formation and effects of interfacial tension.

Van der Sman, R.G.M. and Van der Graaf, S., 2006. Diffuse interface model of surfactant adsorption onto flat and droplet interfaces. Rheologica acta, 46(1), pp.3-11.

Venkatesan, J., Rajasekaran, S., Das, A. and Ganesan, S., 2016. Effects of temperature-dependent contact angle on the flow dynamics of an impinging droplet on a hot solid substrate. International Journal of Heat and Fluid Flow, 62, pp.282-298.

Ward, T., Faivre, M. and Stone, H.A., 2010. Drop production and tip-streaming phenomenon in a microfluidic flow-focusing device via an interfacial chemical reaction. Langmuir, 26(12), pp.9233-9239.

Wever, D.A.Z., Picchioni, F. and Broekhuis, A.A., 2011. Polymers for enhanced oil recovery: a paradigm for structure–property relationship in aqueous solution. Progress in Polymer Science, 36(11), pp.1558-1628.

Wu, Y., Fu, T., Zhu, C., Wang, X., Ma, Y. and Li, H.Z., 2015. Shear-induced tail breakup of droplets (bubbles) flowing in a straight microfluidic channel. Chemical Engineering Science, 135, pp.61-66.

Yagub, A.S., 2016. Specialized Inter-Particle Interaction Lbm For Patterned Superhydrophobic Surfaces.

Yildiz, Y. and Nalbant, M., 2008. A review of cryogenic cooling in machining processes. International Journal of Machine Tools and Manufacture, 48(9), pp.947-964.

Yu, D., Mei, R. and Shyy, W., 2002. A multi-block lattice Boltzmann method for viscous fluid flows. International journal for numerical methods in fluids, 39(2), pp.99-120.

Zhang, L. and Guo, F., 2008. Micro-mechanisms of residual oil mobilization by viscoelastic fluids. Petroleum Science, 5(1), pp.56-61.

Zhang, L.J. and Yue, X.A., 2008. Displacement of polymer solution on residual oil trapped in dead ends. Journal of Central South University of Technology, 15, pp.84-87.

Zhou, H. and Pozrikidis, C., 1994. Pressure-driven flow of suspensions of liquid drops. Physics of Fluids, 6(1), pp.80-94.

ABSTRACT

SURFACTANTS, THERMAL AND SURFACE ENERGY EFFECTS ON EMULSIONS' TRANSPORT PROPERTIES: A STUDY USING LATTICE BOLTZMANN METHOD

by

WESSAM FALIH HASAN

August 2018

Advisors: Drs. Naeim Henein and Hassan Farhat

Major: Mechanical Engineering

Degree: Doctor of Philosophy

This work aims to provide an efficient Gunstensen LBM based CFD model, capable of solving complex problems related to droplets behavior in shear and parabolic flows.

Thermal conditions determine the outcome of the physical and transport properties of emulsions during their various processing phases. A better understanding of the intricate relationship between thermal, surfactants and hydrodynamics can help in the optimization of these processes during the production of emulsions. To investigate the outcome of coupling thermal, surfactants and hydrodynamics on emulsions behavior, a robust quasi-steady thermal-surfactants numerical scheme is presented and used here. To validate the model, the rheological behavior of oil-in-water system was investigated. The numerical results matched well the experimental results of the similar oil-in-water

system under steady-state thermal conditions. Furthermore, it is shown that the proposed numerical model can handle cases with transient thermal conditions while maintaining good accuracy.

The model has been improved to study the combined effects of temperature, and contact angle on the movement of slugs and droplets of oil in water (O/W) system flowing between two parallel plates and in 3D confined flow study. This is found in the enhanced oil recovery technique which includes thermal, contact angle and surfactant effects for breaking up trapped crude oil.

The model static contact angle due to the deposition of the O/W droplet on a flat surface with simulated hydrophilic characteristic at different fluid temperatures, matched very well the proposed theoretical calculation.

Furthermore, the model was used to simulate the dynamic behavior of droplets and slugs deposited on the domain's upper and lower surfaces, while subjected to parabolic flow conditions. The model accurately simulated the contact angle hysteresis for the dynamic droplets cases. It was also shown that at elevated temperatures the required power to transport the mixture diminished remarkably. The aim is to improve our understanding of the underlying physics associated with the secondary and tertiary extraction process of trapped crude oil in wells by injecting hot water.

Finally, the model was utilized for the investigation of the flow behavior of O/W emulsions with the goal of delineating the best practices for transporting these emulsions in circular ducts. The effects of temperature, volume fraction, flow

pressure gradient, and surfactants concentration are investigated in a Poiseuille flow setup. A dimensionless power number ratio was introduced and successfully used for guiding the selection of the most cost-efficient means for transporting O/W emulsion.

AUTOBIOGRAPHICAL STATEMENT

WESSAM FALIH HASAN

EDUCATION

2016~Present
PhD in Mechanical Engineering, Wayne State University, MI, USA
2013~2016
MSc in Mechanical Engineering, Wayne State University, MI, USA
2006~2009
MSc in Mechanical Engineering, University of Technology, Baghdad, Iraq
1998~2002
BSc in Refrigeration and Air Conditioning Engineering, Technical College, Kirkuk, Iraq

EXPERIENCE

2005~Present
Mechanical engineer at North Oil Company, Kirkuk, Iraq
2010~2012
Lecturer at The Technical College, Kirkuk, Iraq

PUBLICATIONS

Journal papers

- Hasan, Wessam F., H. Farhat, S. Kondaraju, and T. Singh. "Hybrid quasi-steady thermal lattice Boltzmann model for studying the rheology of surfactants contaminated emulsions." Comp& Fluids 165 (2018): 188-198.

- Hasan, Wessam F., and Hassan Farhat. "Hybrid thermal lattice Boltzmann model to study the transportation of surfactants contaminated emulsions in parabolic flows." J.of Petroleum Sci and Engineering 166 (2018): 85-93.

Conferences

- Hasan, W., Hassan Farhat, Ameer Alhilo, and Luma Tamimi. "Hybrid Quasi-Steady Thermal Lattice Boltzmann Model for Studying the Behavior of Oil in Water Emulsions Used in Machining Tool Cooling and Lubrication." World Academy of Science, Engineering and Technology,
- Hasan, W., and H. Farhat. "Investigating the Effects of Thermal and Surface Energy on the Two-Dimensional Flow Characteristics of Oil in Water Mixture between Two Parallel Plates: A Lattice Boltzmann Method Study." World Academy of Science, Engineering and Technology